MOLECULAR DYNAMICS SIMULATIONS TO STUDY THE EFFECT OF FRACTURING ON THE EFFICIENCY OF CH_4 - CO_2 REPLACEMENT IN HYDRATES

By

Aditaya O. Akheramka, B. Tech.

A Thesis Submitted in Partial Fulfillment of the Requirements

for the Degree of

Master of Science

in

Petroleum Engineering

University of Alaska Fairbanks

May 2018

APPROVED:

Abhijit Dandekar, Committee Chair
Shirish Patil, Committee Co-Chair
Mohabbat Ahmadi, Committee Member
Ahmed E. Ismail, Committee Member
Abhijit Dandekar, Chair
Department of Petroleum Engineering
Douglas Goering, Dean
College of Engineering and Mines
Michael Castellini, *Dean of the Graduate School*

Abstract

Feasible techniques for long-term methane production from naturally occurring gas hydrates are being explored in both marine and permafrost geological formations around the world. Most of the deposits are found in low-permeability reservoirs and the economic and efficient exploitation of these is an important issue. One of the techniques gaining momentum in recent years is the replacement of CH_4-hydrates with CO_2-hydrates. Studies have been performed, at both laboratory and field based experimental and simulation scale, to evaluate the feasibility of the *in situ* mass transfer by injecting CO_2 in gaseous, liquid, supercritical and emulsion form. Although thermodynamically feasible, these processes are limited by reaction kinetics and diffusive transport mechanisms. Increasing the permeability and the available surface area can lead to increased heat, mass and pressure transfer across the reservoir. Fracturing technology has been perfected over the years to provide a solution in such low-permeability reservoirs for surface-dependent processes. This work attempts to understand the effects of fracturing technology on the efficiency of this CH_4-CO_2 replacement process. Simulations are performed at the molecular scale to understand the effect of temperature, initial CO_2 concentration and initial surface area on the amount of CH_4 hydrates dissociated.

A fully saturated methane hydrate lattice is subjected to a uniaxial tensile loading to validate the elastic mechanical properties and create a fracture opening for CO_2 injection. The Isothermal Young's modulus was found to be very close to literature values and equal to 8.25 GPa at 270 K. Liquid CO_2 molecules were then injected into an artificial fracture cavity, of known surface area, and the system was equilibrated to reach conditions suitable for CH_4 hydrate dissociation and CO_2 hydrate formation. The author finds that as the simulation progresses, CH_4 molecules are released into the cavity and the presence of CO_2 molecules aids in the rapid formation of CH_4 nanobubbles. These nanobubbles formed in the vicinity of the hydrate/liquid interface and not near the mouth of the cavity. The CO_2 molecules were observed to diffuse into the liquid region and were not a part of the

nanobubble. Dissolved gas and water molecules are found to accumulate near the mouth of the cavity in all cases, potentially leading to secondary hydrate formation at longer time scales.

Temperatures studied in this work did not have a significant effect on the replacement process. Simulations with varying initial CO_2 concentration, keeping the fracture surface area constant, show that the number of methane molecules released is directly proportional to the initial CO_2 concentration. It was also seen that the number of methane molecules released increases with the increase in the initial surface area available for mass transfer. On comparing the positive effect of the two parameters, the initial CO_2 concentration proved to have greater positive impact on the number of methane molecules released as compared to the surface area. These results provide some insight into the mechanism of combining the two recovery techniques. They lay the groundwork for further work exploring the use of fracturing as a primary kick-off technique prior to CO_2 injection for methane production from hydrates.

Table of Contents **Page**

List of Figures **Page**

List of Tables **Page**

List of Appendices **Page**

List of Abbreviations

CG : conjugate gradient

DCV-GCMD : dual control volume - grand canonical molecular dynamics

EEZ : Exclusive Economic Zone

EPM2 : modified extended primitive model

etol : energy tolerance

ftol : force tolerance

GCMC : Grand Canonical Monte Carlo

GHSZ : Gas Hydrate Stability Zone

HBS : Hydrate Bearing Sediments

Ice Ih : hexagonal crystal form of ordinary ice

JOGMEC : Japan Oil, Gas and Metals National Corporation

LAMMPS : Large-scale Atomic/Molecular Massively Parallel Simulator

LJ : Lennard-Jones

MD : Molecular Dynamics

MRI : Magnetic Resonance Imaging

MSD : Mean Square Displacement

N : number of particles

NEMD : Non equilibrium molecular dynamics

NPT : Isothermal-isobaric ensemble

NVT : canonical ensemble

OPLS-AA : Optimized Potentials for Liquid Simulations - All Atom

OVITO : Open Visualization Tool

P : pressure

PBC : Periodic Boundary Conditions

PDF : Pair Distribution Function

POM : Polyoxymethylene

RDF : Radial Distribution Function

SA : surface area

SASA : solvent accessible surface area

sI : cubic structure I of hydrate

sII : cubic structure II of hydrate

sH : hexagonal structure of hydrate

SPC/E : extended simple point charge

STP : Standard Pressure and Temperature

T : temperature

TIP4P/Ice : Transferable Interatomic Potential 4-point / Ice

TraPPE : Transferable Potentials for Phase Equilibria

V : volume

VLE : Vapor Liquid Equilibrium

μ: chemical potential

μVT : Grand Canonical ensemble

Acknowledgements

I would like to express my sincere gratitude to the following people that helped me throughout the duration of this work:

Dr. Abhijit Dandekar for being my thesis advisor and an inspiring mentor. His encouragement, skillful guidance, and enthusiasm towards the subject have contributed immensely towards the completion of this thesis. I will be forever grateful to him for giving me the opportunity to work on such a challenging and multi-disciplinary research topic.

Dr. Shirish Patil for the time he spent with me as a co-advisor for this thesis committee. Dr. Patil provided valuable assistance when needed from King Fahd University of Petroleum and Minerals (KFUPM) in Saudi Arabia, where he is now Saudi Aramco Chair Professor of Petroleum Engineering. His assistance and contributions, even though there was a 12 hour difference in time zones, are highly appreciated. Also, I would like to thank KFUPM for allowing Dr. Patil to dedicate his time towards this effort.

Dr. Ahmed E. Ismail, from West Virginia University, for the insightful discussions on molecular dynamics simulations. His expertise in the simulation technique and patience to answer all my questions has made a huge positive impact on this work. I learnt a lot about the possibilities and limitations of MD simulations from him and thank him for his constant motivation.

Dr. Mohabbat Ahmadi for serving on my thesis committee and the wonderful ideas he provided.

I would also like to thank Dr. Martin Truffer, Dr. John Keller and Dr. Cheng-Fu Chen, from across the University of Alaska Fairbanks, for sharing their expertise and making complex topics simpler; Dr. Srinath Velaga for sharing his experiences while working on similar systems; and Dr. Angelo Rossi, from

University of Connecticut, for the wonderful workshop in my first summer at UAF introducing me to MD simulations and HPC clusters.

I thank the Research Computing Systems Group at the Geophysical Institute, UAF for providing the high-performance computing and data storage resources; the Dept. of Petroleum Engineering and Dept. of Mining and Geological Engineering for providing the financial support during the last two years.

I also thank all my friends and colleagues at UAF, in Fairbanks, and across the world, for all their help in this journey and making Alaskan winters enjoyable.

Lastly, but most importantly, I would like to thank my family for their continued love and support. This endeavor would not have been possible without their encouragement, understanding and sacrifices. I thank them for everything.

Thank you!

Aditaya Akheramka

CHAPTER 1 INTRODUCTION

Gas hydrates are non-stoichiometric crystalline inclusion compounds composed of light hydrocarbons, CO_2, and H_2S, trapped in an ice-like lattice of water molecules formed under specific conditions of temperature and pressure. Among the naturally occurring hydrates, methane hydrate is the most widely distributed in nature (Sloan & Koh 2008). It is found in two major geological settings, in permafrost and under the seafloor, where thermodynamic conditions are suitable for its spontaneous formation. Large amounts of methane are stored in these formations with estimates ranging between 1,000 and 10,000 Gt of carbon (Kvenvolden 1993).

1.1 Current Methods of Production

Production from these naturally occurring methane hydrate reservoirs has a low environmental risk and very clean natural gas can be produced from concentrated formations. The exact details of the production processes are still being optimized but all methods require destabilizing the hydrate structure equilibrium outside the Gas Hydrate Stability Zone (GHSZ) by either temperature increase, pressure reduction, or changing the equilibrium condition itself.

Depressurization makes the hydrate-bearing sediments unstable by reducing the pressure in the drilled production well. This technique is ideal for Class 1 (gas hydrate with a subjacent free gas zone) settings. The low reservoir permeability (around 0.1 md or less) in the presence of hydrates makes this concept uneconomical in the more commonly found Class 2 (hydrate layer underlain by a water zone) and Class 3 (isolated hydrate layer) type of settings (Konno et al. 2017).

Thermal injection disturbs the hydrate equilibrium by supplying heat to the reservoir. Steam or hot water is injected into the reservoir or circulated around in the wellbore. This technique is slow and inefficient. Also, due to the endothermic nature of gas hydrate dissociation, the reservoir will cool down eventually and re-

establish the hydrate equilibrium conditions blocking any further fluid flow (Konno et al. 2010; Moridis et al. 2011).

Changing the equilibrium condition itself requires the introduction of an inhibitor into the system. Methanol or brine is injected into the hydrate-bearing sediments to shift the equilibrium conditions. The hydrate dissociation continues using the sensible heat released due to shifted equilibrium and the convection heat of the injected inhibitor.

In the past decade, CO_2 injection has been proposed as a method to stimulate the methane hydrate reservoir. This process is similar to the inhibitor injection method, but since CO_2 hydrates are thermodynamically more stable than methane hydrates, they replace the methane in the hydrate cages in an exothermic reaction, helping to continue the dissociation. This process, however, also faces significant challenges due to a reduction in permeability near the wellbore region due to the formation of CO_2 hydrates.

1.2 Field Applications and Their Limitations

All of these methods have been validated extensively at the laboratory scale as well as in numerical simulations at different dimensional scales. First field-scale production tests were conducted at the Mallik test site in northern Canada in 2002 (Dallimore et al. 2005). The trial injected hot water into the formation to destabilize the equilibrium and produced only 468 m^3 methane during the 5 days of production (Hancock et al. 2005a). The total (system) active circulation fluid volume was ~48.5 m^3, with no significant gain or loss, indicating that the wellbore and reservoir remained a closed system. The low energy efficiency of the process and the occurrence of relatively high permeability zones in the reservoir led to the second field trial using depressurization as the primary production technique (Hancock et al. 2005b; Kurihara et al. 2005). The abrupt sand production interrupted this test but the 13,000 m^3 produced in the 6 days of production (Yamamoto et al. 2008) proved the promising nature of depressurization techniques.

Success of the depressurization-triggered methane production in permafrost laid the groundwork for a marine production program in the Eastern Nankai Trough off the shore of Japan, beginning in 2013. Data from Phase 3 tests, conducted recently in 2017, with a redesigned sand control technology, and the associated problems encountered will be released soon and will play a significant role in the future development of marine methane hydrates (Konno et al. 2017) across the world.

These tests confirmed the potential of using depressurization as a methane production technique but will very likely need to be supplemented by a primary stimulation technique using thermal, mechanical, or chemical stimulation as warranted by the local permeability and geological conditions.

Of critical importance for this thesis is the Ignik Sikumi #1 test on the Alaska North Slope evaluating the potential of using CO_2 injection and replacement technique for long-term methane production (Boswell et al. 2016). The test injected a mixture of CO_2 and N_2 in a 2-stage "Huff and Puff" procedure. This test confirmed that the gas hydrate destabilization is controlled and self-limiting. However, the changes in permeability as a result of the gas exchange could prove to be a limiting factor. It has been proven in laboratory experiments and was also observed in the field trials (Schoderbek et al. 2013), that injecting pure CO_2 would result in drastic loss of permeability due to the formation of CO_2 hydrates near the wellbore. The binary mixture of CO_2 and N_2 was introduced to overcome this limitation. N_2 did not help in the formation of CO_2 hydrates but helped in maintaining continuous flow while CO_2 interacted with methane hydrates. The high initial water saturation would also play an important role in this. In experiments replicating the field conditions, a significant reduction in effective permeability was observed when additional water was present (Birkedal et al. 2015).

1.3 Motivation for the current work

The initial low permeability is an issue not only in permafrost hydrates but also in marine hydrates as reported in the sandy and silty marine turbidite formations discovered in the South China Sea (Moridis et al. 2011). The low porosity and poor permeability found in that region has proven a hindrance for effective heat and pressure transfer across the reservoir, reducing long-term productivity (Chen et al. 2017). Therefore, marine sediment reservoirs also need to overcome this challenge for efficient and economic methane production.

Another concern in the long-term use of CH_4 production by guest molecule injection is the final rate and distance of penetration of the guest molecules into the hydrate-rich reservoirs. Experimental work by McGrail et al. (2007) estimated these penetration rates at different temperatures. Similar work at the University of Alaska Fairbanks (White 2003) concluded that the injected CO_2 would penetrate past the initial interface contact with solid methane hydrates, but the rate of penetration would be very slow, on the magnitude of 10^{-8} meters per second.

Such low permeability of the hydrate-bearing zones, spontaneous formation of CO_2 hydrates, and low rates of penetration hinder the mass transfer between incoming guest molecules and existing methane hydrates. It has been confirmed through experiments that increasing the permeability of the hydrate layer can lead to increased heat, pressure and mass transfer through the reservoir; accelerate the rate of methane production and CO_2 sequestration; and effectively increase the cumulative production of the well (Jin et al. 2015; Qorbani et al. 2017; Ruan et al. 2017).

From the simulation point of view, simplistic kinetic models built by Ota et al. (2005) based on their experimental data for the CH_4-CO_2 replacement found that surface area plays a very important role in the initial stages of the process. Based on activation energy comparisons, they concluded that the CH_4 hydrate system underwent surface replacement during the initial contact with CO_2. This surface

reaction later transformed into a diffusion limited process. Therefore, if the replacement process is limited by diffusive transport, increasing the surface area available initially would result in faster and greater CH_4 hydrate dissociation and, possible, CO_2 hydrate formation.

Fracturing technology has been perfected over the years and has addressed this same productivity issue from low-permeability reservoirs in unconventional oil and gas. Fracturing technology could also provide a solution to overcome this issue in the case of methane hydrate-bearing formations and effectively increase reservoir permeability and enhance productivity. The combination of fracturing as the primary stimulation followed by an existing gas hydrate recovery method would lead to increased conductivity of gas hydrate formations. Depressurization and fracturing have been combined in simulations (Song et al. 2016; Qorbani et al. 2016), resulting in increased rate of pressure drop within the reservoir leading to enhanced dissociation and methane release. Similar studies have also been done to combine fracturing with thermal stimulation (Song et al. 2016) and observed greater depths of reservoir penetration and reduced heat losses as the hot fluid entered the crack network. However, there have been no prior studies to the best of this author's knowledge of fracturing as a primary technique followed by the CH_4–CO_2 replacement method for methane production from hydrates. This work attempts to understand the effects of fracturing technology on the efficiency of this *in situ* mass transfer process.

The process is simulated at the molecular scale to understand the driving mechanisms behind the interactions. Since there is very negligible field scale data available to develop reservoir scale models, and since there are also no prior simulations providing guidance about the interaction of the two techniques, it was decided to simulate the processes using molecular dynamics simulations. This will provide insight into the fundamentals of the mass transfer process and lay the groundwork for continuum scale models in the future.

1.4 Thesis Goals

The overall goal of this thesis is to better understand the process of CH_4-CO_2 replacement and the effect of fracturing technology on the efficiency of the exchange at the molecular scale. After an extensive literature review involving both academic and industrial progress on the topic, the following are the ideas the author wants to test during this research.

1. Study the evolution of a fracture in a saturated CH_4 hydrate simulation box. Compare the elastic mechanical properties like Young's modulus from literature and validate the stress-strain behavior. Estimate the surface area as the fracture propagates.
2. Estimate the number of CH_4 molecules released as the fracture propagates. This question is important from the point of view of employing fracturing as a primary means of hydrate reservoir stimulation.
3. Observe the evolution of fracture with time. Provide insight into the fracture mechanism and phase changes along the immediate vicinity of the fracture, and analyze if secondary hydrates form near the mouth of the fracture after releasing the stresses. This is important to ascertain the potential of hydrate growth blocking the flow of released fluid towards the wellbore.

Next, after the basic properties of a fracture are studied, gaseous CO_2 into an artificially created fracture will be introduced and the effects of combining the two recovery techniques will be observed.

1. Find an optimum path for combining the two recovery methods.
2. Insert fixed number of CO_2 molecules into an artificial fracture and let them equilibrate. Monitor the evolution of the replacement process with time.
3. Estimate the number of CH_4 released using coordination number analysis techniques. Monitor the phase changes in the system along the way using mean-square displacements.

4. Analyze the formation of nanobubbles and quantify the bubble size using cluster analysis.
5. Study the effect of temperature on this mass transfer and compare the system properties and number of molecules released at each temperature.
6. Observe the secondary hydrate formation near the mouth of the fracture at each temperature condition.
7. Study the effect of initial CO_2 concentration and initially available surface area on the efficiency of the mass transfer.

And finally, after both sets of analyses are complete, study the effectiveness of combining the two techniques. Verify if using fracturing as a primary stimulation technique, followed by CO_2 injection, holds any promise for further research.

These questions are broad and due to lack of clarity in the actual processes in nature, and the need to understand the mechanisms better for future field deployment at the reservoir scale, the author will model the processes at the molecular scale.

CHAPTER 2 LITERATURE REVIEW

2.1 Methane Hydrates: Fundamentals

Gas hydrates are non-stoichiometric crystalline inclusion compounds with an ice-like lattice of water molecules enclosing low molecular weight gases like methane, ethane, carbon dioxide, etc. (Sloan & Koh 2008). The crystalline lattice contains regularly spaced cages of different sizes and usually contains at most one guest molecule. Unlike with inorganic hydrates, all the cages in naturally occurring gas hydrates are not filled. Therefore, the ratio of gas molecules to water molecules is not fixed.

Methane has been the predominantly found type of guest molecule in naturally occurring hydrates. Methane hydrates are primarily found in two types of geological settings: under the permafrost and below the ocean floor. In these locations, about 99% of hydrates form in marine sediments on continental slopes (Kvenvolden 1999).

In addition to the favorable pressure and temperature conditions, adequate supplies of water and methane gas molecules are required to form stable methane hydrates. The vertical extent over which these conditions are satisfied in the subsurface is commonly referred to as the gas hydrate stability zone (GHSZ). Within the GHSZ, two basic parameters define the amount of gas hydrate volumes present: the porosity of the rock matrix available for hydrate formation and the percentage of that pore space occupied by gas hydrates, called the gas hydrate saturation (Dallimore & Collett 1995). This interval within the GHSZ where gas hydrates actually occur is known as the gas hydrates occurrence zone (GHOZ).

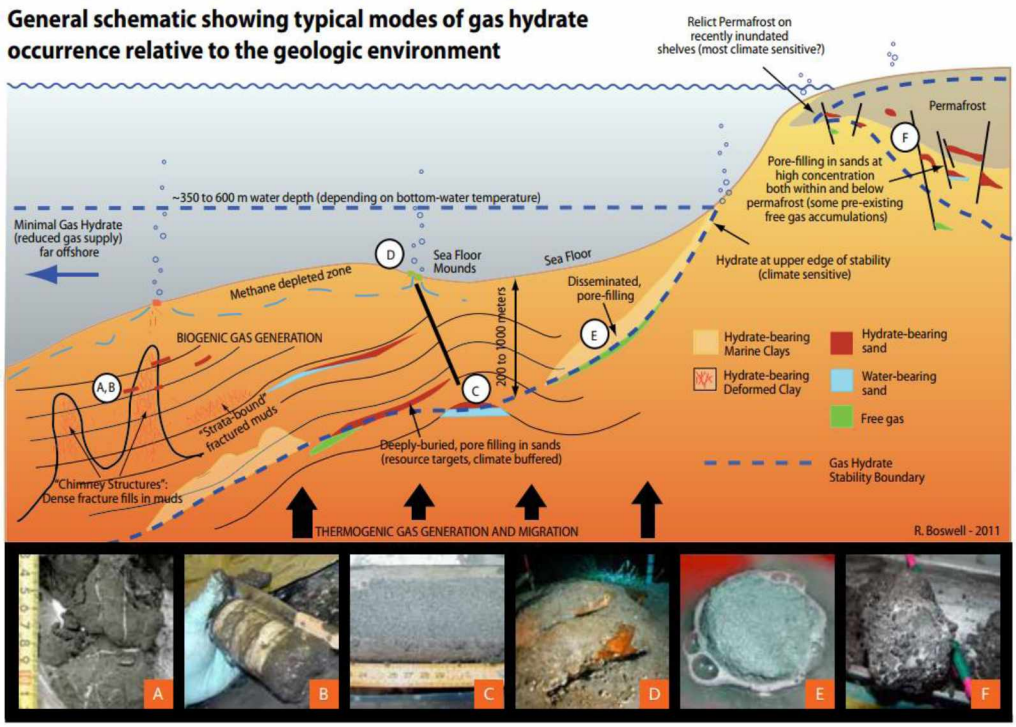

Figure 2.1: General schematic showing typical modes of gas hydrate occurrence relative to the geological environment. This figure is adopted from Boswell 2011.

As shown in Figure 2.1, methane hydrates are found in many forms in nature. The most visible forms are massive mounds of solid hydrate, found exposed on the seafloor bed (D). However, most of the extractable hydrate deposits lie buried in sediment. The relatively high permeability of sands facilitates the formation of hydrates in both the high porosity, high saturation Arctic sands (F) (Collett 2009) and the deeply buried ocean sediments (C) (Boswell 2012). Also, disseminated, pore-filling (E), and thickly veined or sediment-displacing (A, B) accumulations in clay and mud formations are quite commonly found below the ocean floor.

Estimates of methane trapped in these naturally occurring hydrate formations have reduced over the years owing to more accurate mapping, direct sampling and coring efforts across the world. Even so, the current available lowest estimates are so large that they are on the order of 3×10^{15} m^3 (Boswell 2011) of methane gas in place at STP (equivalent to ~1,500 Gt of carbon). They are estimated to satisfy the world's

energy demand for another 300 years according to current consumption rate projections. However, it is important to note here that only a small portion of this enormous resource is available as a recoverable reserve.

2.2 Current Production Methodologies

International projects have been evaluating potential methods for sustainable production of methane from hydrates in both the marine and permafrost settings for decades. The fundamental difference from conventional oil and gas production is the occurrence of hydrates in solid form. Oil and gas flow naturally (or under external push) from the reservoir to the low-pressure wellbore. Hydrates, on the other hand, need to be dissociated before methane gas is free to flow to the wellbore. Figure 2.2 (right side phase diagram) shows the stable pressure-temperature region (shaded blue) of the methane hydrate system. The basic idea is to destabilize the hydrate structure, and keep it out of the stability 'Gas Hydrate + Liquid' zone to avoid reformation.

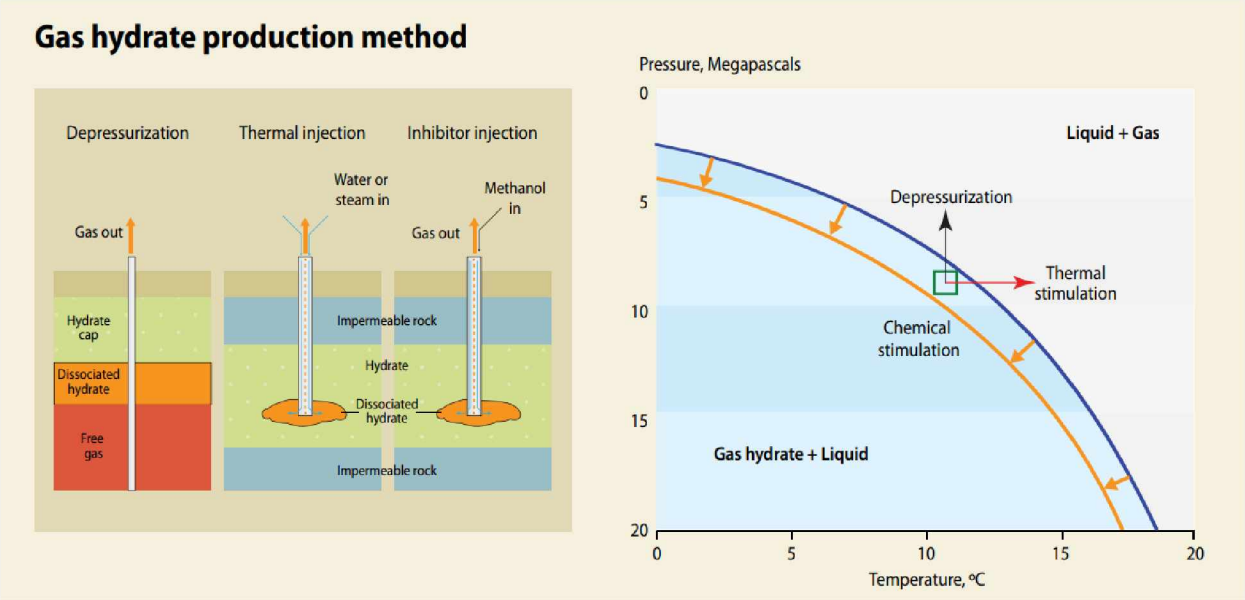

Figure 2.2: Methane Hydrate Production Methodologies. This figure is adopted from Beaudoin et al. 2014

Three different procedures have gained considerable interest over the past few years: depressurization, thermal injection, and chemical injection. Depressurization techniques dissociate gas hydrates by reducing local formation pressures below the equilibrium limits. Thermal injection, on the other hand, achieves the same objective by raising the formation temperatures. Finally, chemical injection, or now CO_2 injection, achieves destabilization by changing the equilibrium conditions altogether.

Of the three techniques mentioned above, depressurization has been proven to be the most promising as far as economic and technical feasibility is concerned. Although there has yet been no long-term commercial production of methane from hydrates, significant short-term pilot studies have been performed by several different groups around the world. The earliest tests were performed to test the thermal injection method by a five-country consortium at the Mallik gas hydrate field in Mackenzie Delta in 2002 (Dallimore & Collett 2005). Depressurization was tested at the same site in 2007 as a joint project by a team from Canada and Japan (Dallimore et al. 2008).

There have been several other smaller drilling and coring projects undertaken over the years, but of particular significance have been the results of two of the latest pilot production tests: Ignik Sikumi #1 on the Alaska North Slope in 2012-13, and the Nankai Trough offshore Japan undertaken by JOGMEC in 2013, and again recently in 2017.

2.2.1 Offshore Japan: Nankai Trough

The Research Consortium for Methane Hydrate Resources in Japan (MH 21 Research Consortium) has been extremely proactive and pioneering in research and efforts toward the development of methane hydrate resources offshore in Japan's Exclusive Economic Zone (EEZ) for the past 15 years (Oyama & Masutani 2017). In 2013, JOGMEC succeeded in producing methane gas from hydrate-bearing sediments (HBS) in the eastern Nankai Trough. Depressurization was utilized to

produce approximately 120,000 m^3 of gas (Konno et al. 2017). The bottom hole pressure was lowered from 13.5 MPa to 4.5 MPa, and the production lasted six continuous days until an increase in sand production occurred. Extensive downhole data and pressure core samples were acquired from the one production well and two monitoring wells in this project.

Along with the actual field trial, numerical models were developed to predict the evolution of the permeability due to hydrate dissociation and to estimate the total production and depths of reservoir penetration in subsequent long-term production. The simulations estimated that the hydrate dissociation zone would expand up to 200 m from the well after 180 days of production (Konno et al. 2017). It expanded 25 m during the 6-day field trial. This estimated decrease in the reservoir penetration rate supports the slow diffusion-driven mechanism assumed to occur in this *in situ* exchange. One of the key learning from the project was the effect of the water-rich layer resulting in high water production, reducing gas-water production ratios, and triggering abrupt sand production. These observations indicated a clear need for zone isolation of the water-rich layer and robust sand management for high long-term gas productivity.

Overall, the trial was the first successful proof of continuous marine hydrate production. It shed light on several interesting observations about sand production in the production well, and seawater and groundwater flow in the reservoir.

More recently in summer of 2017, a second offshore test was conducted near the Atsumi/Shima Peninsula. Newer sand control techniques were deployed and preliminary reports have reported approximately 35,000 m^3 of production from the first production well over 12 days and 200,000 m^3 from the second production well over 24 days (Konno et al. 2017). Data from these tests on extended gas production behavior and the associated problems encountered will be released soon and will play a significant role in the future development of marine methane hydrates across the world.

2.2.2 Alaska North Slope: Ignik Sikumi #1

Another technique being considered for long-term methane production is the injection of CO_2 into the hydrate reservoir. It has been extensively proven that CO_2 hydrates are thermodynamically more stable than the CH_4 hydrates (Ohkagi 1996). Research into practical applications of exploiting this thermodynamically feasible *in situ* exchange has been conducted both in the laboratories and through numerical simulations at all dimensional scales. The Ignik Sikumi field program, conducted in 2012 by a consortium of stakeholders on the Alaska North Slope, was designed to study the commercial viability of using CO_2–CH_4 exchange for long-term production.

The overall design was to inject CO_2 gas as a short-term "Huff and Puff" operation with a single injection/production cycle from a single vertical well. To overcome the problem of possible free water and secondary hydrate formation, it was decided to inject a mixture of CO_2 and N_2 in a fixed stoichiometric ratio. This modified approach ensured no formation of unwanted CO_2 hydrates near the injection point and thereby kept the injection rate high and continuous, long enough for sufficient *in situ* mass transfer. Based on factors like CO_2 phase changes along the length of the well, uncontrolled CH_4 hydrate dissociation due to partial pressure effects, and loss of injectivity due to ice formation in the wellbore region, an optimum ratio of 23% CO_2 was determined.

The formation and breakdown pressures were calculated to be 1,450 psi using the XPT and MDT tools (Boswell et al. 2016). Approximately 6,113 m^3 gas, consisting of 4,737 m^3 N_2 and 1,376 m^3 CO_2, was injected into the reservoir. As seen in Figure 2.3, through the entire production period, 70% of the injected N_2, and 40% of the injected CO_2 were recovered. A total of 24,410 m^3 of CH_4 was produced over a total assisted and unassisted production period of 31 days. In addition, 1,136 bbl of formation water and an estimated 67 bbl of sand were also produced.

Since only 40% of the injected CO_2 was recovered, this trial was a good field scale confirmation of the bulk exchange of CO_2 for CH_4. However, even though the laboratory studies show a direct 1:1 mass transfer of the two gases, in the case of an actual injection well, it was difficult to ascertain the amount of CH_4 liberated due to the direct chemical replacement and as a response to other partial pressure dissociation reasons. Since not much is known about the kinetics of the exchange, and of the mixed gas hydrate formation and dissociation, the ability of the models to reliably infer what happened was also greatly limited.

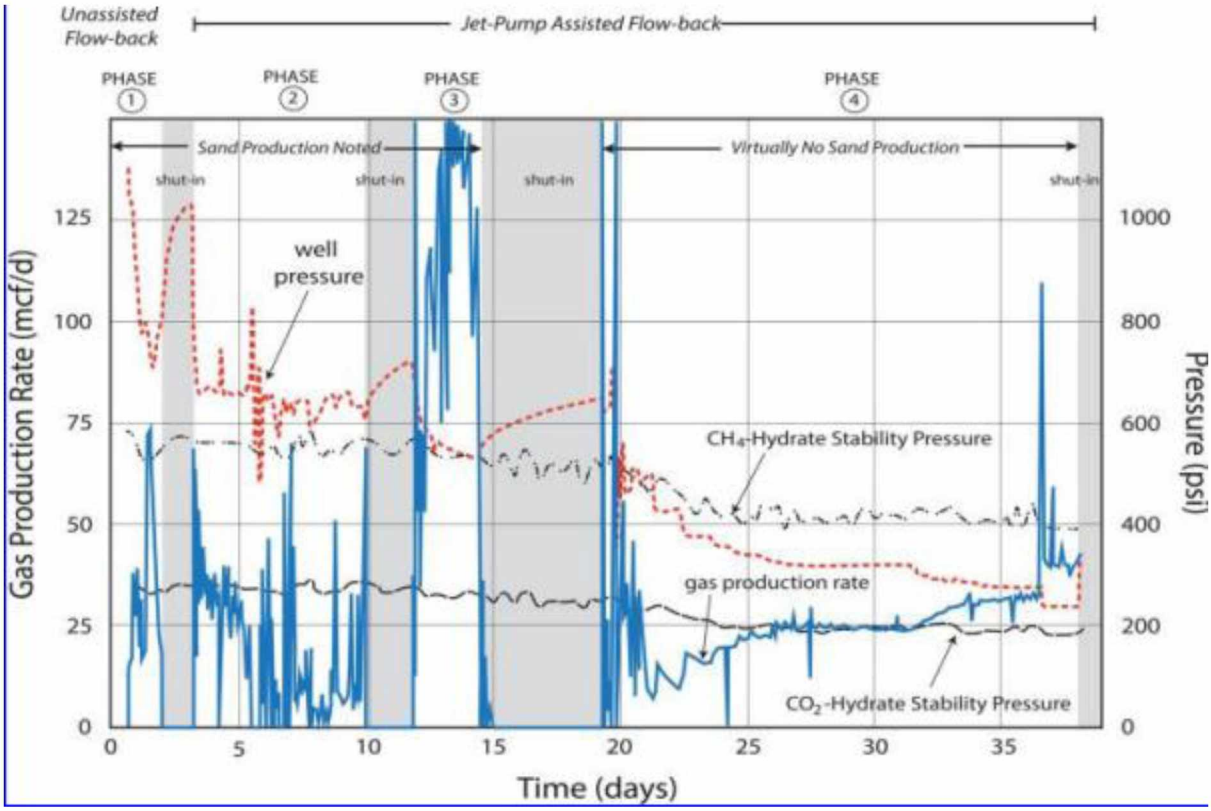

Figure 2.3: Results of Ignik Sikumi field trial. Red dotted line indicates wellbore pressure at the reservoir level. Solid blue line indicates the total gas production rate. Figure adopted from Boswell 2016.

The issue of the geomechanical instability of the reservoir raised more questions because of the produced water and sand, and further complicated the analysis of the source of the produced CH_4 gas. While sand screens and other completion installations were utilized to manage sand production, wide fluctuations in the bottom hole pressures and flow rates during the initial phases of the injection hindered the formation of a stable sand pack behind the sand screens (Boswell et al. 2016). This issue of reservoir fluid expansion associated with hydrate dissociation could be a cause for reservoir subsidence, well completion equipment failure, and channeling leading to unwanted CH_4 migration. However, once the test progressed onto the depressurization stages, the pressures and flow rates stabilized and no further sand production was observed in the last 19 days of production.

Looking at the several methods of methane production from hydrates from both technical and economic viability, and noting the hurdles still left to overcome, the complexity involved in the *in situ* CH_4–CO_2 mass transfer and the promising outcome of not only recovering CH_4 but possibly sequestering CO_2 permanently motivated the author to delve deeper into this topic for this thesis. To increase the low reservoir permeability and to enhance the gas hydrate production, a primary stimulation technique to increase the stimulated surface area is required. The application of fracturing technology can be an effective tool to achieve these objectives. The rest of the chapter looks at literature around two major ideas:

- Mechanical properties of hydrates - experimental and MD simulations
- CH_4–CO_2 exchange - experimental and MD simulations

2.3 Mechanical Properties of Hydrates from Experiments

A clear understanding of the mechanical properties of all forms of hydrates – pure CH_4, pure CO_2, as well as mixed gas hydrates – is essential for a thorough evaluation of the potential of long-term methane production from subsurface reservoirs and concurrent permanent CO_2 sequestration. This knowledge will also help us to understand the mechanical responses of the sediments to hydrate dissociation and formation. Many researchers around the world have investigated these properties experimentally in the past couple of decades.

In the past decade, noteworthy work by the Santamarina group at the Georgia Institute of Technology used triaxial measurements to evaluate various mechanical properties like bulk modulus, the stress-strain curve, Poisson's ratio, shear strength of laboratory-synthesized and marine hydrate-bearing cores (Yun et al. 2007). They also proved that the CH_4-CO_2 replacement occurs without any loss of mechanical stiffness by monitoring the P-wave velocity in CH_4 hydrate-bearing sand before, during and after CO_2 injection (Espinoza & Santamarina 2011). Another significant work by Hyodo et al. (2013) studied deformation behaviors of the Toyoura Sand samples containing CH_4 hydrates. They concluded that while thermal stimulation did cause the failure of samples under certain conditions, depressurization did not lead to collapse. There have been several more such tests under varying external conditions, using both laboratory-synthesized and actual field core samples. However, to keep the focus on permafrost-associated methane hydrates, a recent work by Li et al. (2015) will be explained here in detail.

In the study by Li et al. (2015), and in the follow-up publication by Lui et al. (2016), a series of triaxial tests were conducted to investigate the mechanical stability of permafrost-associated CH_4 hydrate-bearing sediments, dissociating them by both depressurization and thermal injection replicating both constant pore pressure (exhaust) and increasing pore pressure (non-exhaust) conditions.

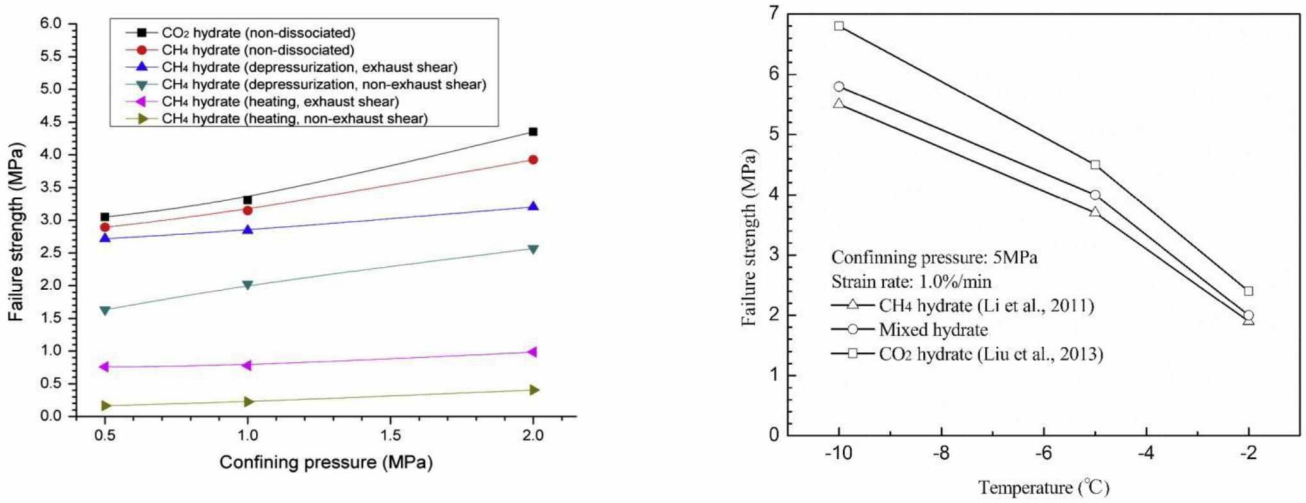

Figure 2.4: Effect of temperature and pressure on failure strength. Pressure curve adopted from Li et al. (2015) and temperature curve from Lui et al. (2016), respectively.

As seen from the above Figure 2.4, both depressurization and thermal injection resulted in a decrease in failure strength and similarly in elastic modulus, E. Also, the failure strengths of mixed hydrate-bearing sediments increased with a decrease in temperature and CO_2 concentration.

Table 2.1: Mechanical properties of sI structure from Waite et al. (2000)

Property	Value
Poisson's Ratio	0.317
Shear Modulus	3.1 GPa
Isothermal Young's Modulus	7.8 GPa

The above Table 2.1, published by Waite et al. (2000), used measurements of compressional and shear wave speeds, assuming the hydrate sample to be isotropic and homogeneous. However, these values closely match other published results in the literature and will be used for comparison in our simulations.

2.3.1 Fracture Propagation from Experiments

Another recent publication by Konno et al. (2016) utilized the use of similar triaxial pressure cells to evaluate hydraulic fracturing of these methane hydrate sediments. The authors again used wet Toyoura sand to synthesize the core samples. The porosity of the core sample was 38% by mass balance. The schematic of the experimental apparatus is shown in Figure 2.5.

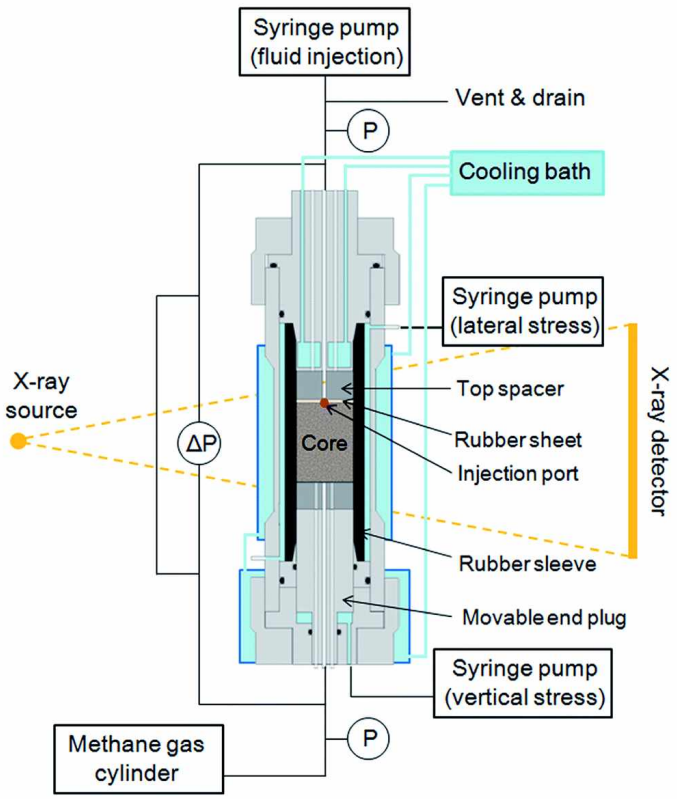

Figure 2.5: Triaxial pressure cell to evaluate hydraulic fracturing of hydrates.
Experimental setup reported in Konno et al. (2016).

The cylindrical core used was 50 mm in diameter and 69.9 mm long. A spacer with an injection port of 3 mm diameter was located at the top of the core. The fracturing fluid was injected using a syringe pump. The pore pressure, axial confining pressure, and lateral confining pressure were 4.1 MPa, 6.1 MPa, and 5.1 MPa,

respectively. The temperature of 276 K was maintained throughout the experiment using an external coolant bath.

The injection rate was kept constant at 5 mL/min. The axial and lateral confining pressures were kept constant as well during injection. After injecting the fluid in two stages, a few connected fractures were observed perpendicular to the minimum principal stress, i.e., lateral stress in their case. The fractures were straight, laminar, and formed radially. The initial effective permeability was of sub-millidarcy order and the fracturing behavior was affected by this low initial permeability yielding a consolidated rock-like fracturing mode. One of the critical observations was that the permeability increased after fracturing and was maintained even after confinement and closure of the fractures. The lack of chemicals and proppants required to keep the fracture open makes fracturing a promising primary stimulation technique for hydrate-bearing sediments.

2.4 Mechanical Properties from MD Simulations

Many experimental investigations have indicated the similarities and differences between the bulk thermal and mechanical properties of gas hydrates and ice I_h (Stern et al. 1998; Helgerud et al. 2009). However, due to limitations in the currently available direct experimental visualization techniques at the nanoscale level, behavior at the molecular scale still remains poorly understood. To overcome this limitation, since the first molecular dynamics simulations by Tse et al. (1983, 1984), there have been hundreds of publications on understanding hydrate dynamics at the molecular scale.

Ning et al. (2012, 2015) in recent years have studied mechanical instabilities in pure monocrystalline, as well as polycrystalline, CH_4 and CO_2 hydrate crystals. In one of the papers (Wu et al. 2015), the group studied the compression and thermal expansion of CH_4, CO_2, and mixed hydrates with different guest molecule ratios. They calculated bulk modulus for pure CH_4 hydrates to be 9.5 GPa at 271.15 K and 10 MPa. This is pretty close to the 9.03 GPa calculated by experimental value at

these conditions. Moreover, they observed that the ratio of CO_2 in the mixed hydrate was inversely proportional to the bulk modulus of the mixed hydrate. In another follow-up paper performing similar MD simulations but on larger systems, they concluded that the methane hydrates initially exhibited elastic properties and showed an abrupt drop in tensile stress meaning a brittle failure pattern. This expected behavior was pretty similar to that of ice I_h. However, methane hydrate possessed larger ultimate tensile stress and critical strain than that of ice I_h.

2.4.1 Fracture Propagation Using MD Simulations

In addition to mentioning the work on mechanical properties using MD simulation of hydrates, it is necessary to lay the groundwork for methods to study fracture propagation at the molecular scale in general. The exhaustive work of Buehler (2006) illustrates in detail the method of estimating crack dynamics, crack tip instabilities, and limiting speeds of cracks at the atomistic levels.

Typically, as shown in Figure 2.6, an initial crack of length a, in a 2-dimensional slab of size $l_x \times l_y$, is created. The dimensions of the slab need to be large enough to avoid the interference of the waves reflected from the boundary with the propagating crack at the initial stages of the simulation. The slab is then loaded with a constant strain rate (uniaxial in the case of 3-dimensional simulations) corresponding to tensile or shear loading. This continuous loading leads to increasing stress and slowly increasing crack velocity upon initiation. Properties to be calculated are averaged over small time intervals to eliminate very high-frequency fluctuations.

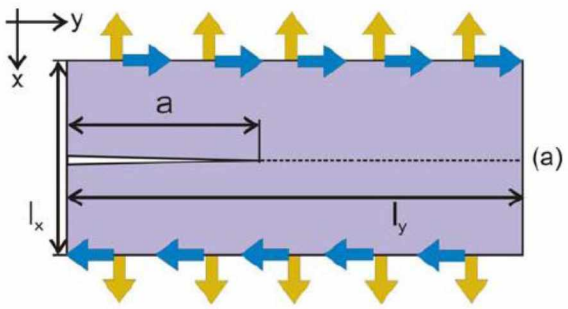

Figure 2.6: Illustration of geometry used in atomistic studies of fracture. Figure adopted from Buehler (2006).

2.5 CH_4–CO_2 Exchange from Experiments

A series of experiments to demonstrate the viability of CH_4–CO_2 exchange in naturally occurring hydrate structures were conducted between 2003 and 2009 in laboratory-synthesized samples. Researchers have studied exchange with gaseous CO_2 (Ohkagi et al. 1996), liquid CO_2 (Hirohama et al. 1996), supercritical CO_2 (Deusner et al. 2012) and even CO_2 emulsions (McGrail et al. 2007). Earlier studies were simplistic in design and emphasized the study of the driving forces that favored this replacement reaction. The hydrate samples were usually created in gas-rich, low water saturation environments in consolidated rocks. These conditions formed hydrates faster with nearly 100% conversion of all water to hydrates but differed from the higher water-saturated reservoirs present in nature.

Ohkagi et al. (1996) and Hirohama et al. (1996) performed a few of the first experiments in this field. Although their experiments proved the thermodynamic feasibility of the exchange, they were severely limited in their reaction kinetics. Also, the available surface area for the mass transfer was limited since these studies dealt with bulk methane hydrate samples placed in direct contact with liquid or gaseous CO_2.

Stevens et al. (2008) used Magnetic Resonance Imaging (MRI) technology to track the progress of CH_4–CO_2 replacement (Figure 2.7). The hydrate samples were

created using 23% porosity and 1,100 mD permeability sandstone acquired from Germany. Two core plug designs were used. First was a standard cylindrical plug. The second arrangement had a 4 mm thick acetal polyoxymethylene (POM) spacer between the two halves of the same cylindrical plug to simulate a fracture opening in the sample where fluids had enhanced access to the porous media. The spacer also acted as an effective region for the dissociated gas to collect. These experiments also measured the effect of changing water salinity on the reaction rates and completion. Another major difference between these tests and earlier experiments was that CO_2 partial pressures here were significantly greater than CO_2 saturation levels.

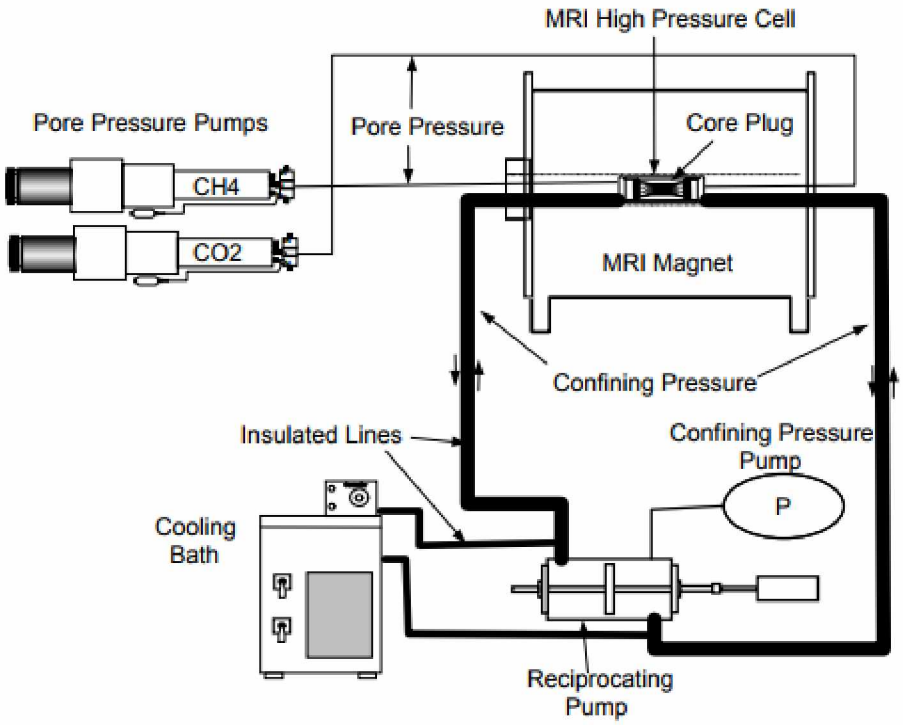

Figure 2.7: Setup to evaluate CH_4-CO_2 hydrate replacement using MRI. Experimental setup reported in Stevens et al. (2008)

The results show that the exchange process was rapid with complete conversion of free water into hydrates. Also, higher salinity resulted in slower hydrate formation rates and less efficiency of water conversion. However, since most of the experiments were run connected to an infinite methane reservoir, it was possible for all free water to convert to hydrates eventually.

2.6 CH_4–CO_2 Exchange from MD Simulations

Owing to the complexity of this process there have been few significant experimental studies and no continuum scale modeling at all. However, there have been a significant amount of publications simulating this at the molecular scale (Kvamme et al. 2010, 2014, 2016; Bai et al. 2012, 2015; Lui et al. 2017). This is also true because much about the mechanisms and dynamics behind this *in situ* transfer needs to be known before it can be convincingly applied to long-term field trials or commercial pilot studies.

Geng et al. (2009) carried out MD simulations to understand the stability of sI CH_4 and CO_2 hydrates and the potential of CH_4 molecules to reoccupy the small cavities. They performed simulations at 50 bar and 260 K, 270 K, and 280 K. Comparing the stabilization energies for the small and big cavities with both guest molecules, they inferred that CO_2 molecules were less suitable for the smaller cavities but more stable in large cavities. Also, they showed that stability of mixed CH_4–CO_2 hydrates were greater than either of the pure hydrates.

Uddin et al. (2014) studied the kinetics of CH_4 and CO_2 hydrate dissociation and were among first to observe nano bubble formation as the CH_4 hydrate dissociated. In addition to the regular quantitative methods of calculating radial distribution functions (RDF), mean square displacements (MSD), and 2D density maps, they introduced an innovative hydrogen bond breakage behavior to analyze the dissociation kinetics. Their simulations established the similarities between the two guest molecule hydrates and also illustrated the effects of gas bubble formation on

overall dissociation stages and changes in system density and volumes for both guest molecules.

Kvamme (2016) followed up the Ignik Sikumi field trial and explored the mechanisms of this multicomponent, multiphase mass transfer and thermodynamic limitations of adding N_2 to the system containing CH_4 hydrate and CO_2 gas. His models include the effects of concentrations and chemical potentials, in addition to the pressure and temperature, on the thermodynamics of mixed gas hydrate stability. He expands on the two discussed conversion mechanisms for this process:

- The solid-state exchange mechanism where the incoming CO_2 gas is met with an impermeable barrier of solid mixed gas hydrates. The kinetic limitation in this mechanism is defined by the rate of mass transport across this hydrate layer.
- Formation of new CO_2 hydrates from incoming CO_2 gas and free water, followed by dissociation of the CH_4 hydrates due to heat liberated from this exothermic formation.

Through multiple molecular dynamics simulations, he makes a convincing case claiming that formation of new CO_2 hydrates is probably the fastest mechanism for exchange between existing CH_4 hydrates and the injected CO_2/N_2 mixtures. Based on the selective absorption in liquid water and thermodynamic non-equilibrium of hydrates in porous media, he argues that CO_2 would be depleted first from the CO_2/N_2 mixture, forming new hydrates.

He also discusses in detail the effects of adding N_2 to the injected CO_2 gas. He observed that the thermodynamic driving potential for formation of these new hydrates was, in fact, reduced by mixing N_2 into the injected CO_2 gas. But this also means that the higher the N_2/CO_2 ratio, the lesser the probability of new hydrate formation blocking the gas flow paths. Therefore, an optimum ratio would have to be injected to ensure continuous injection of guest gas molecules, and at the same time enough exothermic new hydrate formation to dissociate *in situ* CH_4 hydrates.

Bai et al. (2012, 2015) have been actively providing greater insights into this process through microsecond simulations. Through controlling the chemical potentials, and mass transfer limitations, they were able to establish the concepts of "memory effect" and the "self-preserving effect" in CH_4 hydrates. These studies help to suggest that the evolution of structures in bulk hydrate is not only heterogeneous but also step by step. They confirm that CH_4 molecules will first be released gradually, then agglomerate to form bubbles in the liquid regions (Figure 2.8). Their latest paper studies the effects of these bubbles and their dynamic properties of size and shape on the dissociation kinetics of hydrate melting and replacement.

Few of the key analytical tools employed in this thesis are based on techniques mentioned in their latest paper. To provide a quantitative understanding of the bubble dynamics they introduce the concept of cluster analysis of CH_4 molecules with different cutoff radii. They define a cluster as a set of C atoms from CH_4 that are within a fixed cutoff distance from one or more atoms of the same cluster. According to them, a bubble is defined as a cluster with the size of more than 10 atoms. They also use 2D mass density and binning concepts to visualize the shapes of bubbles more clearly. Finally, the technique of coordination analysis is used to track the number of methane molecules moving in and out of hydrate cages. These techniques will be explained in detail when they are utilized later in the thesis.

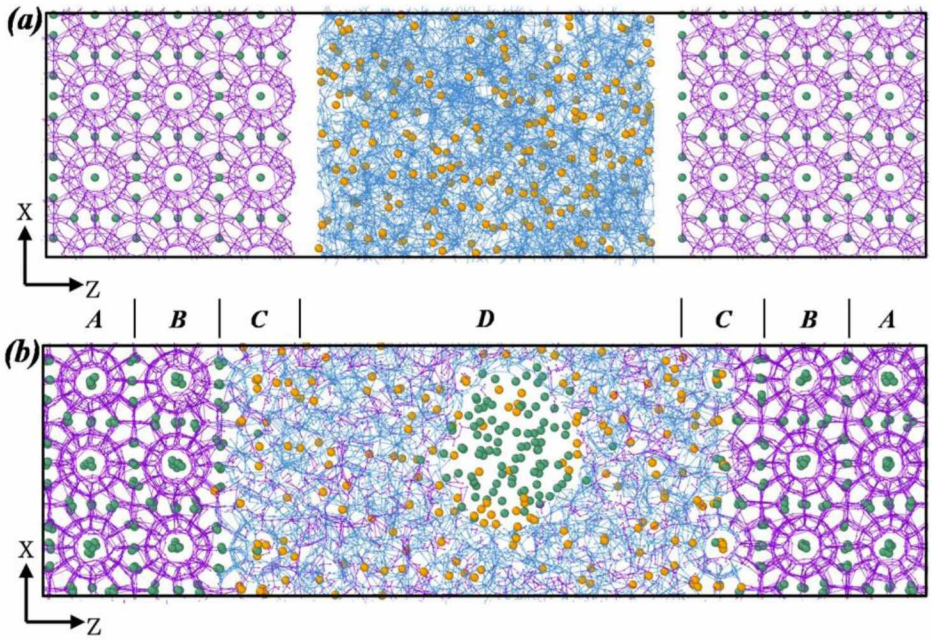

Figure 2.8: Initial and final configuration of replacement system at 180 ns from Lui et al., 2017. CO_2 molecules are shown in orange spheres, methane in green, and water in cyan (liquid phase) and magenta (hydrate phase).

CHAPTER 3 MOLECULAR DYNAMICS SIMULATIONS

Molecular Dynamic (MD) simulations are a statistical thermodynamic technique for computing the behavior of a classical many-body system. This method consists of explicitly defining atoms and/or molecules and studies the effects of external changes on the system based on the interactions between its components. MD simulations solve Newton's equations of motion for a system containing N interacting point particles, given by:

$$m_i \frac{\partial^2 r_i}{\partial t^2} = F_i \tag{1}$$

Where m_i and r_i are the mass and position vectors of a particle i, and F_i is the force acting on the particle i using interaction potential with other particles in the system. In essence, each particle interacts simultaneously with every other particle. Considering a pairwise interaction, the potential on each particle becomes:

$$\mathrm{F}_i = \sum_{j=1}^{N} -\frac{\partial U(r_{ij})}{\partial r_{ij}} \tag{2}$$

Therefore, if there are N particles, initial positions and velocities for all of them need to be specified (6N variables) to uniquely identify the dynamical system. And, one point in a 6N dimensional space represents our dynamical system.

3.1 Molecular Dynamics in Petroleum

Experimental measurements in the oil and gas industry can be very expensive and even detrimental to the physical environment of the system. The use of toxic and explosive chemicals, and the high temperatures and pressures achieved, lead to the design of elaborate experimental setups and often limits the scope of the research. MD simulations provide a safer and more accurate way to gather information about the thermophysical properties of hydrocarbons in a single theoretical framework

(Ungerer et al. 2006). All the system properties can be derived, and extrapolated, from the basic understanding of changes in potential energy of the system.

Another reason why many of the researchers are studying subsurface processes and hydrocarbon interactions at the molecular scale is that experiments cannot provide insight into the behavior at the microscopic level. Predicting thermodynamic properties of heavy hydrocarbons, optimizing the design of zeolite microporous adsorbents, or studying the solubility of gases in polymer materials at high pressures are some of the examples which can be accurately studied using molecular simulations. MD acts as a bridge between experiments in the laboratory and macroscopic thermodynamic models (Allen 2004). In fact, MD is most useful to simulate the dynamic behavior of systems, like diffusion and thermal coefficients, viscosity, and effects of changes in pressure and temperature on transport properties.

3.2 Molecular Potentials

In MD, both the intermolecular and intramolecular interactions are defined by a set of user-defined parameters called the potentials. These parameters vary based on the type of the atom/molecule and define their behavior and properties.

Non-bonding (intermolecular) potentials depend on the spatial configuration of each set of particles in a neighbor list, a list of non-bonded atoms within a user-defined radius. These interaction potentials most commonly contain a repulsion term, a dispersion term, and a coulombic term. In this work, the author uses two non-bonding potentials – the short-range Lennard-Jones potential and the long-range Coulombic potential.

The Lennard-Jones (LJ) potential is often expressed as the sum of pairwise interactions between atoms belonging to different molecules. For two particles separated by a distance r, the standard 12-6 LJ potential (Jones J. E. 1924) is given by

$$E = 4 \in [(\frac{\sigma}{r})^{12} - (\frac{\sigma}{r})^{6}] \qquad r < r_c \tag{3}$$

with two parameters: σ, the diameter, and $\in$, the well depth. r_c is the user defined cutoff radius. The first term represents Pauli repulsion, and the second term represents van der Waals attraction forces.

If the particles carry electrostatic charges, appropriate long-range Coulombic pairwise interactions are added

$$E = \frac{C q_i q_j}{\in V} \qquad r < r_c \tag{4}$$

Where C is an energy-conversion constant, q_i and q_j are the charges on the two atoms, and $\in$ is the relative dielectric constant.

For molecules, the bonded (intramolecular) potentials must also be considered. These comprise bond stretching (2-body), bend angle (3-body), dihedral angle (4-body), and a special type of improper dihedral angle interactions.

A simple 2-body harmonic bond potential is given by

$$U_{harmonic} = k(r - r_o)^2 \tag{5}$$

where r_0 is the equilibrium distance between the particles and k is a constant of proportionality.

3.3 Periodic Boundary Conditions

In principle, MD simulations can be performed in infinite space, but they are limited by the computational resources. To give the appearance of an infinite simulation box, unless the surface effects are of particular interest, Periodic Boundary Conditions (PBC) are employed. In PBC, a particle that leaves one face of the simulation box enters the box on the opposite face with the same velocity. The minimum image convention used ensures that each atom interacts with the nearest atom in the periodic array, i.e., each pair of particles is counted only once

irrespective of the number of times the particle crosses the periodic boundary. PBC is important since it allows for estimating bulk phase properties without expending enormous computational power. However, it is important to be aware of this imposed periodicity when considering properties affected by well-known finite-size effects.

3.4Temperature Coupling

In this thesis, both Berendsen (Berendsen et al. 1984) and Nose-Hoover (Evans & Holian 1985) thermostat coupling schemes are used to control the temperature at the desired values. Fundamentally in MD, the equipartition theorem (Tolman R. C. 1918) is employed to calculate the instantaneous temperature:

$$\langle E_k \rangle = \frac{f}{2} k_B T \tag{6}$$

where f is the number of kinetic degrees of freedom, and T is the thermodynamic temperature.

3.4.1 Berendsen Temperature Coupling

The Berendsen algorithm weakly couples the system to an external heat bath with temperature T_o using first-order kinetics. It is used to relax a system to the desired temperature. The deviation of the system from the bath temperature is corrected by introducing a timescale for velocity rescaling given by:

$$\frac{dT}{dt} = \frac{T_o - T}{\tau} \tag{7}$$

where τ is a characteristic time constant which controls the exponential decay of temperature deviation.

3.4.2 Nose-Hoover Temperature Coupling

Once the system is equilibrated, Nose-Hoover thermostat simulates proper canonical ensemble, by introducing an extra dynamic friction term and a thermal

reservoir to the system Hamiltonian in the equations of motion. The equations of motion are replaced by:

$$\frac{d^2 r_i}{dt^2} = \frac{F_i}{m_i} - \varepsilon \frac{dr_i}{dt} \tag{8}$$

In principle, Berendsen thermostat should only be used when achieving equilibrium for a non-equilibrated spatial distribution, followed by the Nose-Hoover thermostat for sampling.

3.5 Pressure Coupling

Similar to the temperature coupling, pressure coupling can be implemented by either the Berendsen (Berendsen et al. 1984) or Parrinello-Rahman (Parrinello & Rahman 1981) barostat coupling schemes. Fundamentally in MD, the virial equation for the pressure expresses the instantaneous pressure in a classical N-body system:

$$P = \frac{N k_B \tau}{V} + \frac{\langle W \rangle}{3V} \tag{9}$$

where $\langle W \rangle$ is an ensemble average of the virial function of potential energy of the system.

Both Berendsen and Parrinello-Rahman barostat coupling schemes employed in this thesis are similar to the Berendsen and Nose-Hoover thermostat coupling schemes respectively.

3.6 Statistical Ensembles

The concept of statistical ensembles is the cornerstone of molecular dynamic simulations. It characterizes a probability distribution of all possible states of a system compatible with a set of imposed constraints. Using each of these possible states, average system properties can be determined. This Table 3.1, adapted from Ungerer et al. (2006), illustrates the most commonly used statistical ensembles in MD simulations and few of their applications.

Table 3.1: Statistical Ensembles (Ungerer et al. 2006)

Statistical Ensemble	Imposed Variables	Applications
Canonical ensemble	N, V, T	Phase properties
Grand canonical ensemble	μ_i, V, T	Adsorption isotherms, selectivities
Isothermal-isobaric ensemble	N, P, T	Phase properties
Microcanonical ensemble	N, V, E	Transport properties
Gibbs ensemble	$N = N_1 + \ldots N_m$, P, T	Phase equilibrium of pure components and mixtures

In the current work, the author employ the use of canonical (NVT), isothermal-isobaric (NPT) and grand canonical (μ_iVT) ensembles at different stages of simulations.

3.7 Limitations of MD Simulations

Before diving into the details of simulating methane hydrate systems using MD, it is very important to know the limitations of simulating at the molecular scale.

- Timescales

  Usual timesteps in MD simulations are of the order of a few femtoseconds (10^{-15} seconds) for numerical stability. Given the expensive computations required to simulate millions of equations of motion for a system containing hundreds of thousands of particles at each time step, most MD simulations will only reach a few microseconds even after using enormous HPC clusters. Changes in the system, for example, exchange of CH_4 and CO_2 in a hydrate system, or structural changes in proteins, can take up to a few nanoseconds

to show up in average properties and hence, are limited by the availability of computational resources. Advances in computer power have enabled microsecond simulations, but simulation timescales still remain a challenge.

- Length Scales

  Similar to the issue with timescales, the dimensions of the simulation box are related to the number of particles in the system. This has a direct impact on the number of equations to be solved at each timestep and hence, the computational resources required. Periodic Boundary Conditions are a useful tool to overcome this limitation but are applicable only when surface effects are not of particular interest.

- Ignoring quantum effects

  In classical MD, one replaces the Schrodinger equation with the classical Newton equation. One indicator of the validity of the replacement is the de Broglie wavelength Λ. Quantum effects are expected to become significant when Λ is much larger than the interparticle distance. Therefore, all atoms, except for the lightest ones such as H, He, Ne are considered as 'point' particles at sufficiently high temperatures and classical mechanics can be used to describe their motions.

CHAPTER 4 MODEL DETAILS

Large-scale Atomic/Molecular Massively Parallel Simulator (LAMMPS) (Plimpton, 1995) by Sandia National Labs was used to model the system. The numerous studies of modeling hydrates at the molecular scale have used a range of potential models - varying water and guest interatomic potentials, fixed charge and polarizable, rigid and flexible, using different combination rules, etc. However, since the primary purpose of this thesis is to demonstrate the possibility of the proposed idea, the authors chose to use the most commonly used potential models for simplicity. The idea is to use models which have been proven to accurately predict the properties of the two processes – application of uniaxial strain (fracturing) and CH_4–CO_2–H_2O interactions.

4.1Water Models

SPC/E (Berendsen et al. 1987) and TIP4P/Ice (Abascal et al. 2005) are the two models extensively used for methane hydrate simulations. However, more recently, TIP4P/Ice has been proven to be more accurate in describing the density of water from the melting point up to the boiling point in the presence of dissolved hydrocarbons (Fernandez et al. 2006).

In this work, the TIP4P/Ice model for describing water molecules is used.

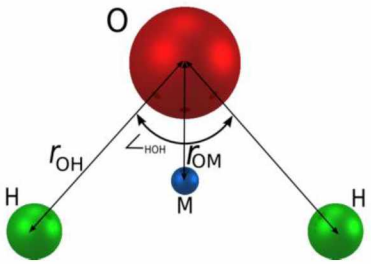

Figure 4.1: TIP4P/Ice Water Molecule

(http://www.sklogwiki.org/SklogWiki/index.php/TIP4P/Ice_model_of_water)

As seen in Figure 4.1, TIP4P/Ice is a 4-site rigid water model. The long-range electrostatic interactions are coulombic, and the oxygen-oxygen interactions are Lennard-Jones (LJ). The parameters are given in Table 4.1.

Table 4.1: TIP4P/Ice Model Parameters (Abascal et al. 2005)

Parameter	Value
O mass (u)	15.9994
H mass (u)	1.008
O charge (e)	-1.1794
H charge (e)	0.5897
r0 of OH bond (Å)	0.9572
θ of HOH (deg)	104.52
OM distance (Å)	0.1577
LJ ϵ of O-O (kcal/mol^{-1})	0.21084
LJ σ of O-O (Å)	3.1668
LJ ε, σ of OH, HH	0

4.2Methane Models

The fully atomistic Optimized Potentials for Liquid Simulations – All Atom (OPLS – AA) (Kaminski et al. 1994; Jorgensen et al. 1996) model was used to describe the methane interactions. The intermolecular interactions are described in the usual Coulomb plus Lennard-Jones format.

$$\Delta E = \sum_{i}^{a}\sum_{j}^{b}\left(\frac{q_i q_j e^2}{r_{ij}} + \frac{A_{ij}}{r_{ij}^{12}} - \frac{C_{ij}}{r_{ij}^{6}}\right) \qquad (10)$$

In the above equation, the interaction energy between molecules a and b is described by a summation over all pairwise interactions between sites i and j on the two molecules. Also, $A_{ij} = 4\epsilon_i\sigma_i^{12}$ and $C_{ij} = 4\epsilon_i\sigma_i^{6}$.

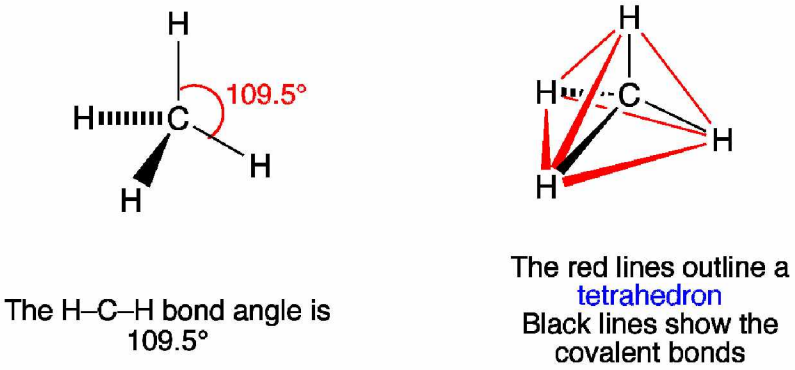

Figure 4.2: OPLS-AA Methane Molecule

(http://www.chemtube3d.com/VSEPRShapeCH4.html)

The charges for the OPLS force field have been developed by fitting to reproduce the properties of organic liquids and are, therefore, empirical in nature (Table 4.2).

Table 4.2: OPLS-AA Model Parameters (Kaminski et al. 1994; Jorgensen et al. 1996)

Parameter	Value
C mass (u)	12.0110
H mass (u)	1.008
C charge (e)	-0.2400
H charge (e)	0.0600
LJ ϵ of C-C (kcal/mol^{-1})	0.066
LJ σ of O-O (Å)	3.5
LJ ϵ, σ of HH	0

4.3 Carbon Dioxide Models

TraPPE (Potoff & Siepmann 2001) and EPM2 (Harris & Yung 1995) are the two potential models used for modeling CO_2 molecules. They have both been used inconclusively for simulating CO_2 hydrates. Optimization studies for CO_2 potential (Zhang & Duan 2005) concluded that neither of these can be regarded as the 'perfect' model for describing CO_2. Since both of them accurately predict the pure-component VLE data (Potoff & Siepmann 2001), but the TraPPE model is less accurate than EPM2 at higher pressures (Zhang and Duan 2005), the flexible 3-site EPM2 model was used. This model is a combination of the bond-bending potential, the short-range LJ potential, and the long-range Coulombic potential.

$$u_{bending}(\theta) = \frac{1}{2} k_\theta (\theta - \theta_o)^2 \qquad (11)$$

where k_θ = 1236 kJ/mol/rad^2 is the bond-bending force constant.

The equations describing pairwise LJ and Coulomb potentials are similar to the ones used for methane.

Table 4.3: EPM2 Carbon dioxide Model Parameters (Harris & Yung 1995)

Parameter	Value
C mass (u)	12.0107
O mass (u)	15.9994
C charge (e)	0.6512
O charge (e)	-0.3265
LJ ϵ of C-C (kcal/mol^{-1})	0.05589
LJ σ of C-C (Å)	2.757
LJ ϵ of O-O (kcal/mol^{-1})	0.1599
LJ σ of O-O (Å)	3.033

4.4 Lattice Structure Used

There are several known hydrate crystal structures, however, only three of these – structure I (sI), structure II (sII), and structure H (sH) – have been proven to be found in nature (Ripmeester et al. 1994). Extensive crystallographic studies were done by McMullan & Jeffrey (1965) on sI and sII structures. They confirmed that the unit cell of sI hydrate is cubic with space group Pm3n and a lattice constant of 12.03 Å at 248 K. As seen in Figure 4.3 and Table 4.4, for every 46 water molecules, 8 methane molecules occupied the 2 pentagonal dodecahedral (5^{12}) and the 6 tetrakaidecahedral ($5^{12}6^2$) cavities. These studies conclusively determined the position of oxygen atoms in water but did not determine the positions and orientations of protons in a systematic way.

The proton disorder of water molecules still remained an issue since multiple proton positions and orientations satisfied the ice rules and yet resulted in differences in molecular environments for the guest molecules. Sparks et al. (1999) developed an algorithm to randomly assign proton positions following the Bernal-Fowler Rules (Bernal & Fowler 1933) and with a net zero dipole moment. This is an example of a purely topology based method. Okano & Yasuoka (2006) performed a detailed energy-based analysis of proton positions in the sH structure by calculating the potential energy and net dipole moment for various orientations. The lowest energy orientation satisfying the ice rules was chosen as the most stable. Such energy-based methods employ a Monte Carlo algorithm and quantify adherence to the ice rules to determine the final configuration.

Takeuchi et al. (2013) performed similar energy-based analysis of proton positions for the sI and sII structures. They also compared the effects of these different configurations on the electrostatic forces experienced by the guest molecules. The detailed coordinates of oxygen and hydrogen positions in sI structure are provided in the paper by Takeuchi et al. (2013) for reference.

Table 4.4: Methane Hydrate Lattice Structures

Property	Structure I	Structure II	Structure H
Lattice	Cubic	FCC	Hexagonal
Space Group	*Pm3n (no. 223)*	*Fd3m (no. 227)*	*P6/mmm (no. 191)*
Lattice Constant	a = 12.03 Å	a = 17.31 Å	a = 12.3 Å c = 10.2 Å
H_2O / guest, min	46 / 8 = 5.75	136 / 24 = 5.67	34 / 6 = 5.67
Mean Cavity Radius, Å	3.95 (S), 4.33 (L)	3.91 (S), 4.73 (L)	3.94 (S), 4.04 (M), 5.79 (L)

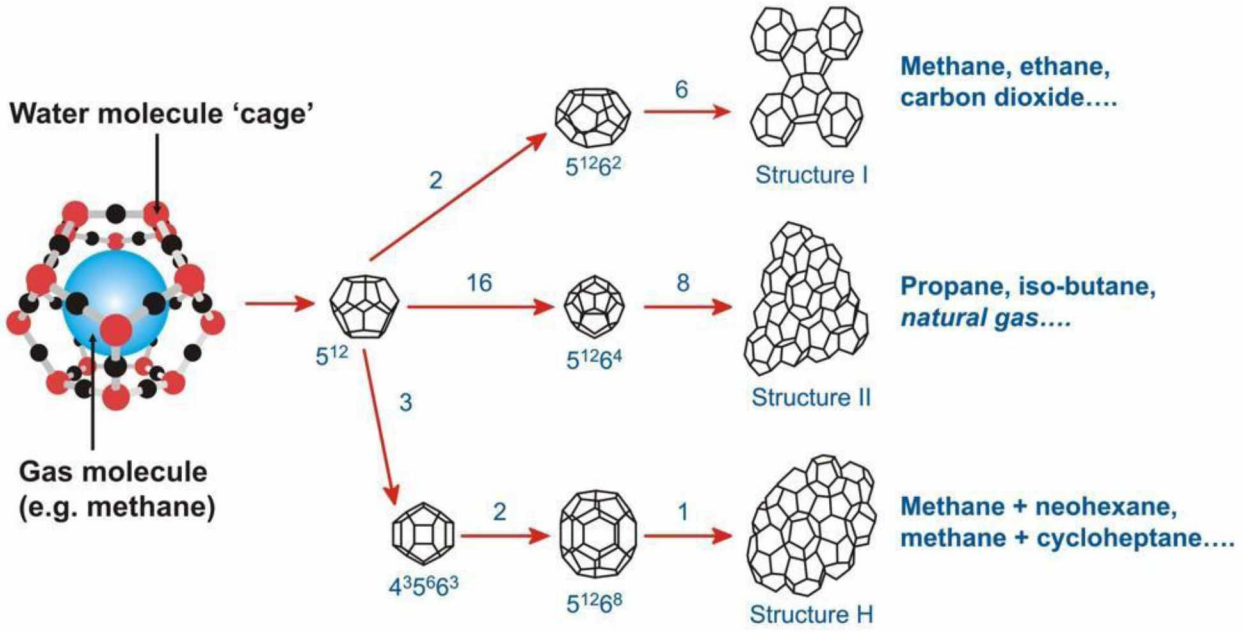

Figure 4.3: Methane Hydrate Structures. Figure is adopted from http://www.pet.hw.ac.uk/research/hydrate/images/hydrates/structures_large.jpg

4.5 Basic Simulation Box

Using the coordinates provided in Takeuchi et al. (2013), and expanding the unit cell using the miller indices provided in Sparks et al. (1999), a 4×3×2 simulation box was created. As shown in Figure 4.4, this contains total 24 unit cells of 46 H_2O and 8 CH_4 molecules each.

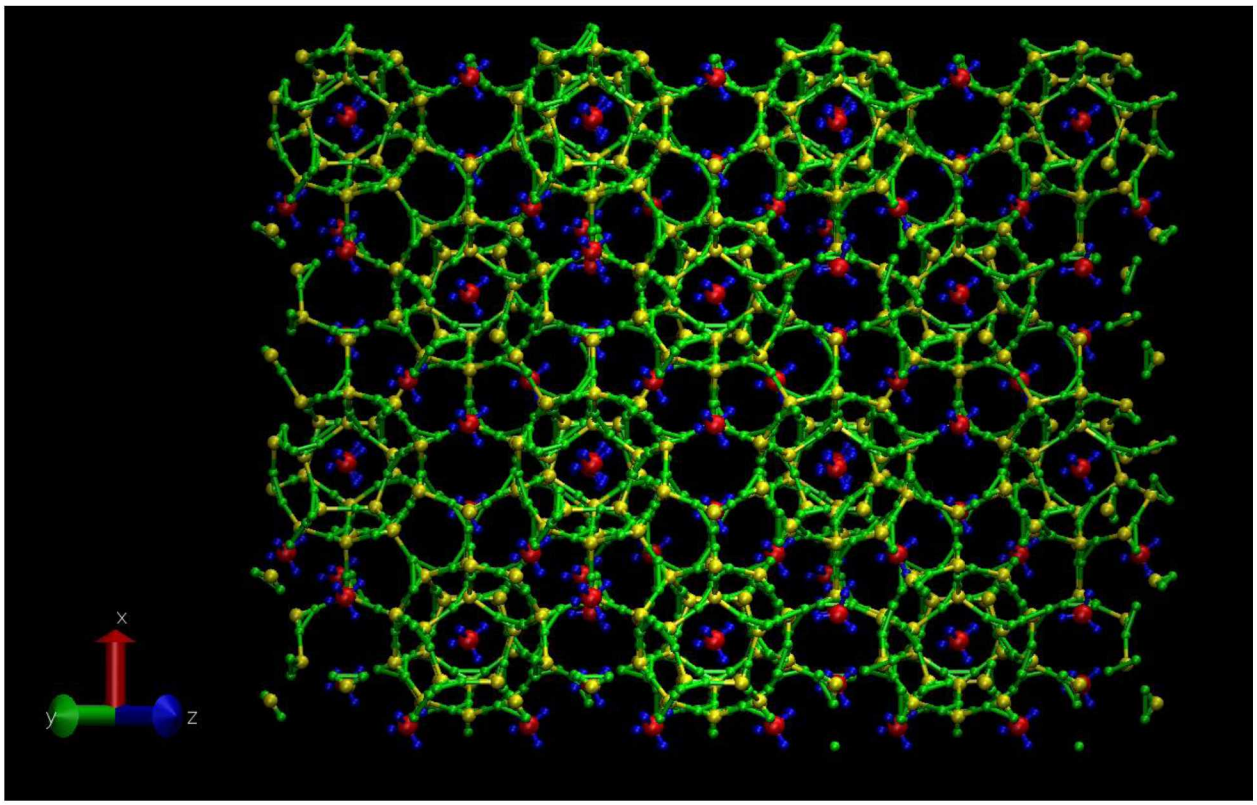

Figure 4.4: Basic simulation box of 4x3x2 unit cells. It contains 1104 water molecules and 192 methane molecules. Water is shown by yellow oxygen and green hydrogen spheres; methane is shown by red carbon and blue hydrogen spheres.

4.6 Energy Minimization

It is very important to have an equilibrated starting configuration for the molecular dynamic simulations to not encounter unreasonable forces. This was observed a lot in this work, initially when the simulation box was not energy minimized or

sufficiently equilibrated using the suitable statistical ensemble. This resulted in the loss of atoms at particular time steps. This was caused by either overlapping atoms or atoms coming too close and repelling each other.

I use the Polak-Ribiere (Polak 1971) version of the conjugate gradient (CG) algorithm available in LAMMPS. It iteratively adjusts the atom coordinates till one of the local potential energy minima is reached. The objective function being minimized is the total potential energy of the system which includes all pair, bond, angle, dihedral, improper and fix terms for the N atom coordinates. This method uses the gradient information of the previous step and therefore gets much closure to the nearest minimum.

I define the two parameters – energy tolerance (*etol* = $1e^{-10}$) and force tolerance (*ftol* = $1e^{-10}$) for defining the stopping criterion. Specified *etol* criterion is met when the energy change between successive iterations divided by the energy magnitude is less than or equal to the tolerance value. Specified *ftol* criterion is met when the final force on any component reaches the upper bound value defined by tolerance value.

4.7 Final Simulation Box

The final simulation box was created by replicating this 4x3x2 box using LAMMPS. The final simulation box (Figure 4.5) contained 18x12x3 unit cells. The dimensions were chosen to avoid the ripple effects of fracture propagation from walls, and yet reasonable as far as simulation time was concerned.

After energy minimization using the CG algorithm, the system was further equilibrated for 250 ps using the NPT ensemble. The conditions of P = 50 atm and T = 270 K was chosen such that the CH4 hydrates were stable.

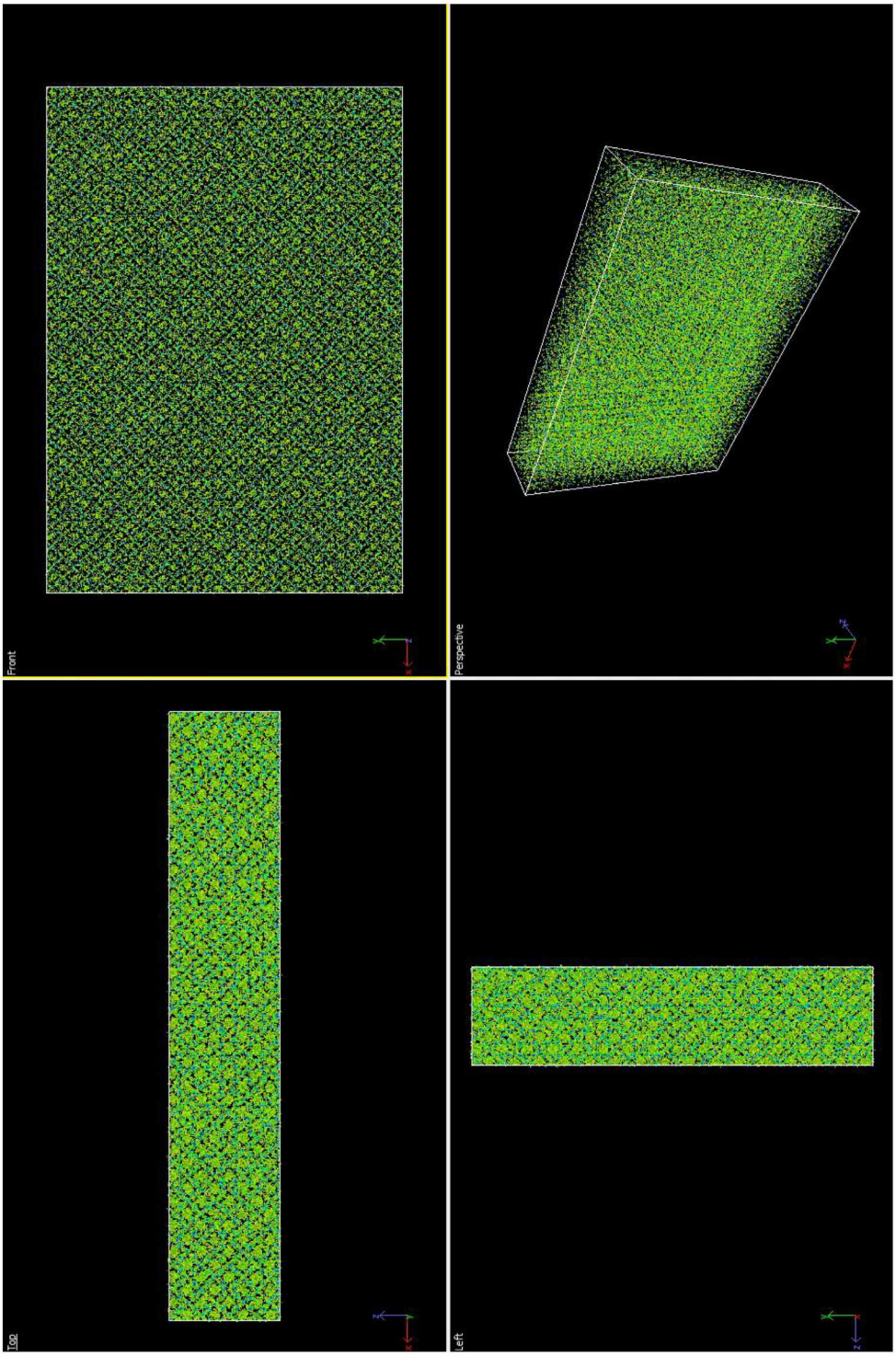

Figure 4.5: Final simulation box of 18x12x3 unit cells. It contains 26112 water molecules and 4608 methane molecules. Water is shown by yellow oxygen and green hydrogen spheres; methane is shown by dark blue carbon and light blue hydrogen spheres

CHAPTER 5 FRACTURE MODELING

An in-depth understanding of the mechanical properties of hydrates under different conditions is essential to predict the behavior of the naturally occurring hydrate-bearing sediments under different production scenarios. Depending on the geological formations hydrates occur in; their mechanical properties could be crucial to the drilling methodology employed, the changes in permeability of the reservoir, and propagation of fluids during the injection and/or production periods. The current chapter begins by verifying a few of the widely measured, both experimentally and using molecular dynamics simulations, characteristic elastic properties of methane hydrate structures. The idea of fracturing a hydrate system is then introduced and a protocol for measuring the fracture properties is developed. The hydrate simulation box, developed in the previous section, is subjected to a constant uniaxial strain and the evolution of the fracture surface area and the amount of CH_4 released is then estimated.

5.1 Measuring Elastic Properties

A simple approach to measuring the elastic properties of the system is to subject it to a constant uniaxial strain. LAMMPS has a *fix deform* function which allows us to apply a 'constant true shear strain rate' in only the y-direction. If the material is isotropic, tensile strain in all the three orthogonal directions would give exactly similar mechanical properties. The atom positions are rescaled periodically to avoid the introduction of elastic waves in the solid methane hydrate structure. The Young's modulus is estimated as the ratio of the normal stress to normal strain.

For the purposes of estimating the elastic properties of the structure, the final simulation box was 12x12x3 sI unit cells. The simulation box was subjected to a true strain rate of 2×10^{-7} fs^{-1} for 1 ns simulation run. This resulted in a maximum strain of 0.20. The system was allowed to deform and dimensions were allowed to change in all directions. The normal stress vs normal strain curve is shown

alongside in Figure 5.1. The system exhibited elastic behavior followed by failure, consistent with the results of previous experimental and molecular simulation works (Sloan & Koh 2008). The ultimate tensile stress occurs at a strain of ~14.8%. The gradual drop of the load indicates melting before complete rupture (Sveinsson 2015). As shown in Figure 5.2, the Young's modulus was calculated as the slope of the stress vs strain curve and estimated to be 8.2508 GPa from the initial elastic response. This value matches closely to the values estimated by experiments, as shown in Table 5.1.

Table 5.1: Comparison of elastic properties

Property	**Literature**		**Current Work**
	Experimental Value	**MD Simulation**	**MD Simulation**
Isothermal Young's Modulus	8.4 @ 268 K (Sloan & Koh 2008)	8.4456 @ 250 K (Jia 2016)	8.2508 @ 270 K

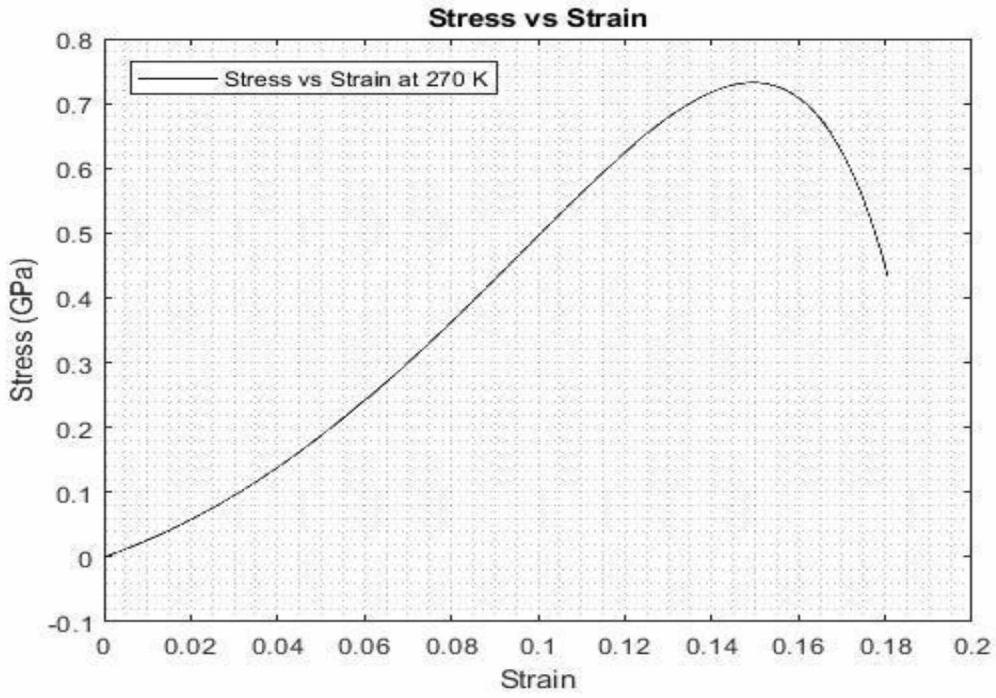

Figure 5.1: Stress vs Strain for a methane hydrate system at 270 K

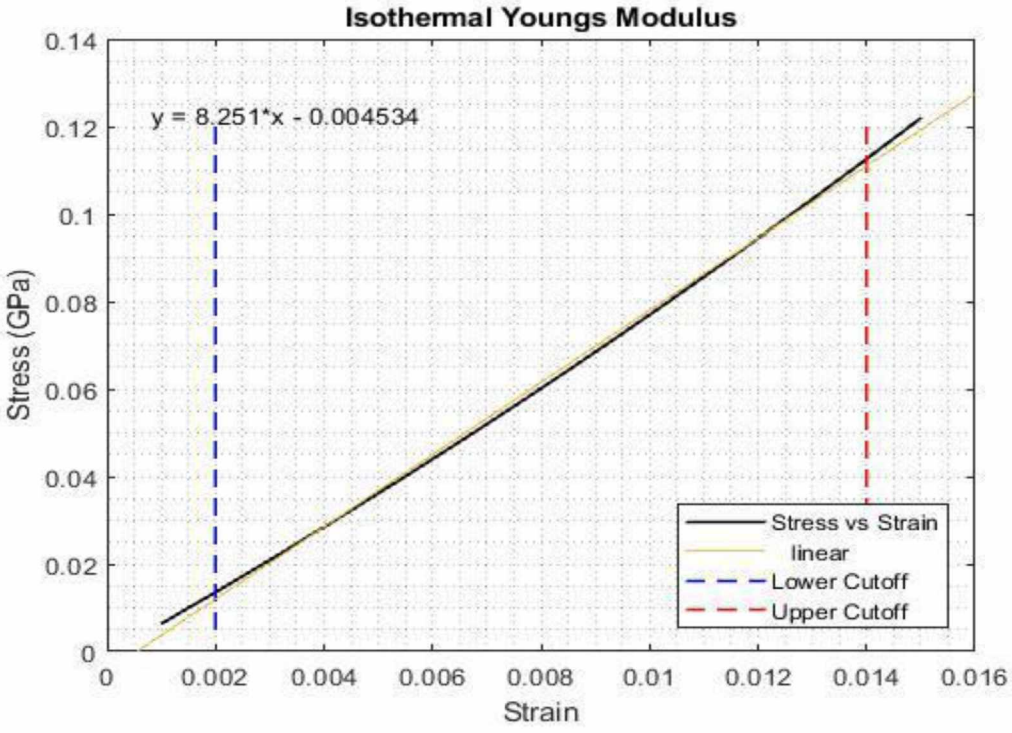

Figure 5.2: Estimation of Isothermal Young's Modulus at 270 K

5.2Simulation Protocol for Fracturing

As mentioned in the previous section, a 12x12x3 unit cell simulation box was used to study the evolution of fracture propagation in methane hydrates. Several different approaches have been applied to study the fracturing process using MD simulations in solids (Buehler 2006).

In the current work, the author first equilibrates the simulation box for 50 ps using the NPT ensemble at P = 50 atm and T = 270 K. In this equilibrated box, a small crack is carved out at one of the faces to initiate the fracture in that direction. This system is then again equilibrated using NPT at the same conditions for another 50 ps. The uniaxial loading was simulated using the deformation-control technique (Ning et al. 2012). The system was subjected to a uniaxial tensile loading for 250 fs at the same true strain rate as in the previous section, followed by a relaxation using the NVT ensemble at T = 270 K for another 250 ps. This cycle of alternate deformation and relaxation is continued for a total of 1 ns simulation time.

The steps are mentioned below in chronological order:

1. Equilibrate the 12x12x3 unit cell system using NPT ensemble at P = 50 atm and T = 270 K for 50 ps.
2. Carve out a cavity on one of the faces using the *delete_atoms* command in LAMMPS.
3. Equilibrate again using NPT ensemble at P = 50 atm and T = 270 K for 50 ps.
4. Perform deformation using *fix deform* at a constant true strain rate of $2x10^{-7}$ fs^{-1} for 250 fs.
5. Relax the system using NVT ensemble at T = 270 K for 250 fs.
6. Repeat steps 4 and 5 for a total simulation time of 1 ns.

The time duration of each individual step in the technique was based on several runs measuring the evolution surface area and amount of CH_4 molecules released. These are not optimized to maximize CH_4 production or stimulated surface area,

but just to demonstrate the procedure of fracture propagation in a methane hydrate system.

5.3Surface Area Measurements Using OVITO

Measuring the surface area of the fracture as it propagates with time is one of the crucial first steps to calculate any other property of fracture mechanics. However, it is far from trivial to get this dynamic measurement for a fractal-like surface created by the methane hydrate cages and the void spaces generated by dissociated cages. This work uses the Solvent Accessible Surface Area (SASA) (Shrake & Rupley 1973) concept to estimate the evolution of surface area with time. The Construct Surface Mesh (Stukowski 2014) feature of the OVITO tool (Stukowski 2010) used in the post-simulation analysis here is a modification of the SASA algorithm, and measures not only the surface area but also the solid volume. It uses the alpha-shape method of Edelsbrunner & Mucke (1994).

The SASA technique of surface area measurement, also known as the 'rolling ball' method, estimates the surface area accessible to a probe sphere of a user-defined size (Shrake & Rupley 1973). This small probe sphere represents a solvent molecule and it is rolled over the entire methane hydrate simulation box. The surface area traced by the center of this probe is the solvent accessible surface area of the system. Choosing the radius of this probe sphere carefully, the surface area of the fracture at regular time intervals in $Å^2$ can be estimated. The following Figure 5.4 shows the surface area of the fracture at different time steps estimated by a sphere of probe radius 5.0 Å. This radius was chosen to be big enough to cover only the generated surface of the fracture and be small enough to glide over the fractal-like surfaces created by dissociated hydrate cages.

Figure 5.3 shows a sample output display of the OVITO Construct Surface Mesh tool. As can be seen, the radius of the probe sphere was set at 5.0 Å and there was no polygon smoothing done to give more accurate results.

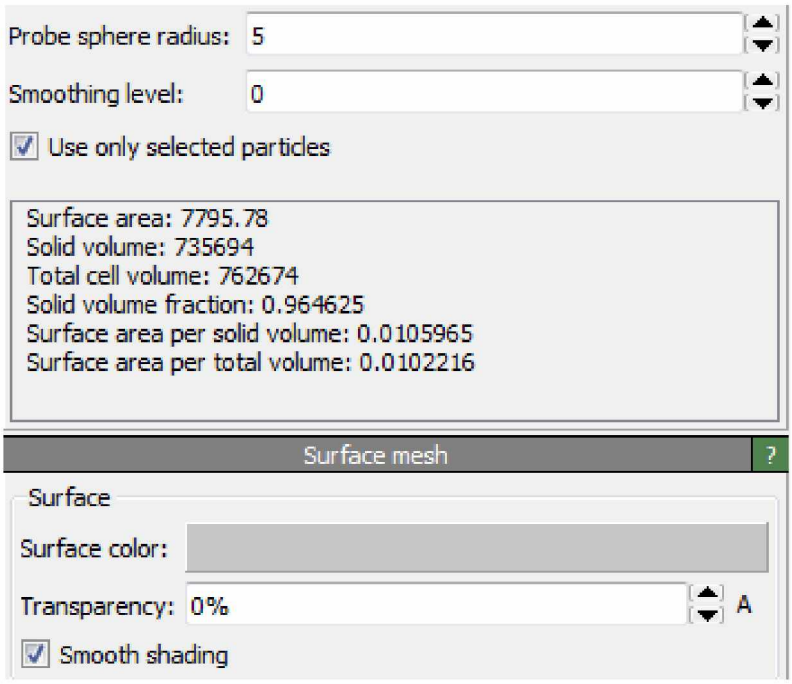

Figure 5.3: Example output displaying Construct Surface Mesh feature of OVITO at 400 ps.

Figure 5.4 shows snapshots of the system taken every 200 ps. The evolution of the fracture is evident from the increasing gray-color surface covered by the rolling particle. The methane molecules being released into the cavity can also be seen to increase as the fracture tip propagates across the box. The simulation box size was limited by the computational resources available, and ultimately a system spanning crack is created. It would be interesting to observe the effect of the dimensions of the box, especially in the direction of the fracture propagation, on the surface area increase and number of methane molecules released.

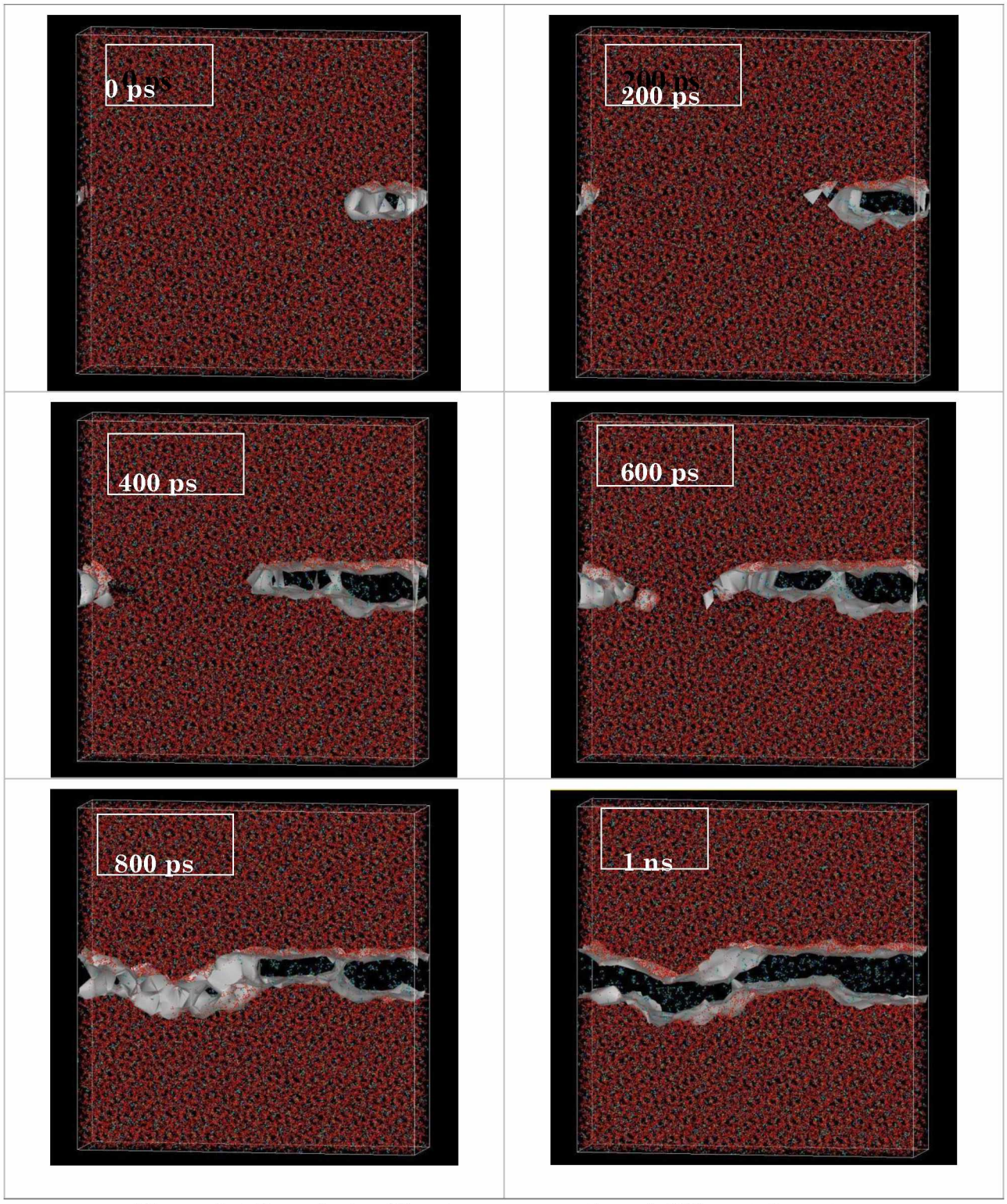

Figure 5.4: Snapshots of fracture propagation at different time steps

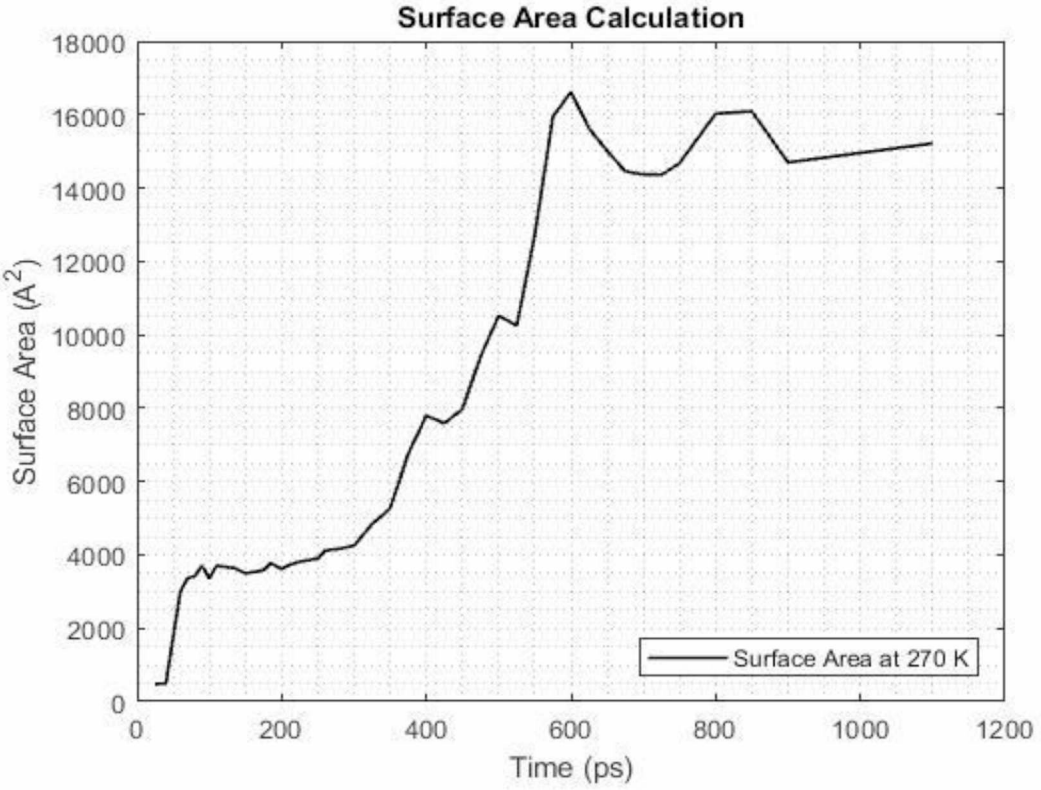

Figure 5.5: Surface Area evolution with time

The tool was applied selectively on only the water molecules. Figure 5.5 shows the increase in surface area with time. It can be seen that surface area does not vary much after 800 ps. This agrees with the snapshots as a system spanning crack after around 800 ps is observed.

Since the CH_4–CO_2 *in situ* replacement process is limited by diffusive transport; the number of methane hydrate cages stimulated is proportional to the surface area available for interaction (Jung & Santamarina 2010). Since there have been no studies quantitatively relating the available surface area and the replacement, it is difficult to estimate the required fracture dimensions to conclusively stimulate a given volume of methane hydrate reservoir, with or without CO_2 injection. However, this works shows that fracturing will provide the necessary mass transfer surface area to maximize the CH_4–CO_2 replacement.

5.4Amount of Methane Released

The main objective of fracturing a methane hydrate system is to dissociate the hydrate cages and release methane molecules into the cavity. It is important to estimate the number of methane molecules released as a function of time. To estimate this number, a rule introduced by Yagasaki (2014) and later modified by Liu (2017) is adopted. The author assumes that a CH_4 molecule is in the hydrate cage if the number of water molecules surrounding it in the first hydrate shell (within 5.5 Å from the methane molecule) is greater than methane's hydration number of 23. Using OVITO selectively on C atoms of CH_4 molecules, the coordination number of all atoms which have more than 23 water molecules surrounding them is computed. This gives us the number of CH_4 molecules dissociated and free from the hydrate cages. Although, this gives us a good estimate it does not account for the methane molecules which are outside the cages but not yet far enough from the water molecules or are dissolved in the liquid water.

Figure 5.6 shows the number of methane molecules released as a function of time at 270 K. As seen, the number tends to increase as the fracture propagates but achieves an almost constant value once the system spanning crack is created. This is expected as once the fracture crosses the length of the simulation box, no new hydrate cages are being broken. The system is then just equilibrating with the existing stress regime and this result in slights changes as methane molecules move in and out of the water layer created at the fracture surface.

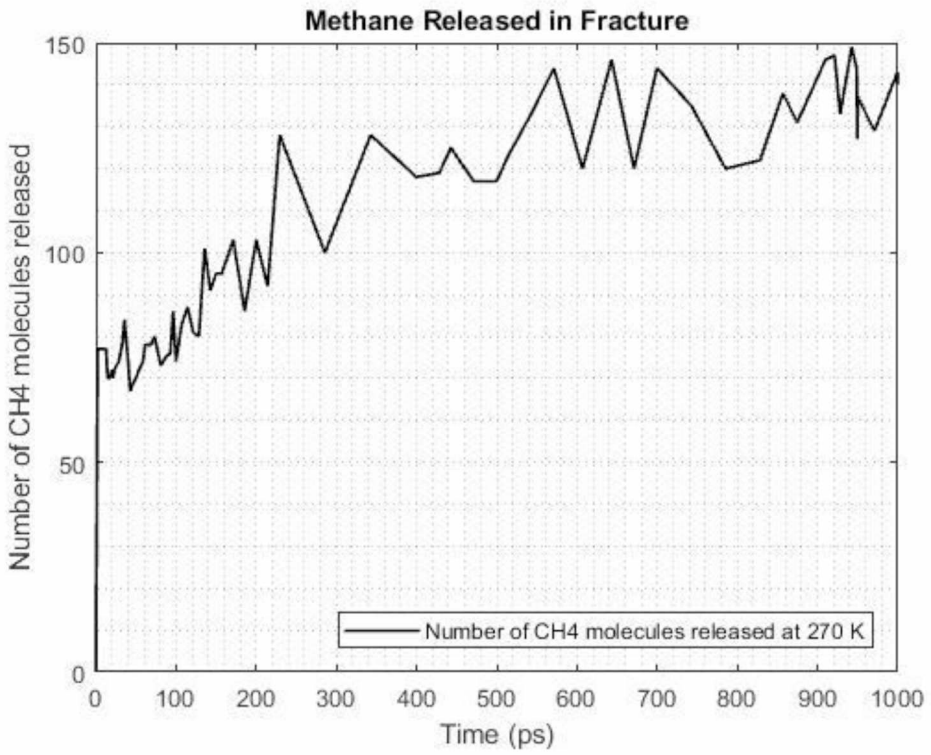

Figure 5.6: Amount of methane released as fracture propagates

There is not much prior research published studying the fracturing of methane hydrates at the molecular scale and the focus of this thesis was to see the potential of combining the techniques of fracturing and CH_4–CO_2 *in situ* replacement. Therefore, the study of fracture development in the system and details like the behavior of the crack tip, variation in fracture conductivity with stresses applied, optimizing the amount of methane released, etc., were left out of the scope of this current work. The elastic properties of the 100% saturated methane hydrate systems were verified and found to be in close agreements with literature. The fracture dimensions and the increase in surface area available for the *in situ* mass transfer were estimated as a function of time. Finally, the amount of methane released due to the propagation of the fracture was estimated using coordination analysis. These results lay the groundwork for further study of using fracturing as a primary recovery technique in methane hydrate systems, with or without CO_2 injection.

CHAPTER 6 CO_2 INJECTION IN ARTIFICIAL FRACTURE

The objective of this chapter is to combine the two techniques of fracture propagation and CO_2–CH_4 replacement in a CH_4 hydrate system. Ideally, this method would first create a hydraulic fracture in the hydrate-bearing sediments, then insert gaseous CO_2 into the created cavity to allow for the *in situ* mass transfer on the exposed surface area of the fracture. The author has not found any previous work using fracturing as a primary stimulation technique, and then coupling it with a secondary recovery technique. Therefore, the concepts studied here are more exploratory than conclusive. There is a lot of uncertainty in understanding the sequence of processes and raises questions like

- How would the gaseous CO_2 diffuse in the hydraulically fractured sediments? Will it dissolve in the water and form secondary hydrates?
- Will proppants be needed to keep the fracture open? How will they interact with the incoming CO_2?
- Would gaseous CO_2 be the optimum phase to maximize the replacement? Would liquid, supercritical, or even CO_2 emulsions give better CH_4 productivity?
- What are the relative timescales of the two processes, fracture propagation and mass transfer, to model them at the molecular scale? How much equilibration time would be needed to optimize the *in situ* mass transfer at the reservoir scale modeling?

These questions, and several other such fundamental issues, need to be conclusively answered; at both the simulation and the experimental scale before a combined recovery idea like this can be implemented in the field. The scope of this current work is to provide a little more insight into some of these unanswered questions. However, due to limitations of time and computational resources, it would be

difficult to conclusively make any claims regarding the field scale applicability of these recovery techniques.

The following chapter explains the methodology adopted to insert gaseous CO_2 molecules into a fractured hydrate simulation box, and analyzes the evolution of phase changes, coordination numbers, and nanobubble formation with time. Wherever possible, it compares the results with other CH_4–CO_2 exchange studies without the fractured environment. To understand the effect of temperature on this replacement process, all simulations are performed at three temperatures - 260 K, 270 K, and 280 K. Finally, to understand the effect of CO_2 concentration and the available surface area for mass transfer, the number of methane released is tracked in different cases.

6.1 Problems with Using an Actual Fracture

In the previous chapter, the author simulated fracture propagation in the hydrate box by applying uniaxial tensile loading in the y-direction and saw the fracture propagate in x-direction, parallel to the direction of maximum horizontal stress.

However, it was proving difficult to define the boundaries of the region formed by the changing surface area of the propagating fracture as a function of time (Figure 6.1 (top)). Moreover, there were no universally accepted methods available in literature.

Therefore, for the sake of this thesis and to prove the effect of the increased surface area due to a fracture on the CH_4-CO_2 replacement, a rectangular cavity in an unfractured simulation box by deleting molecules in a specific region is created. This resulted in a cavity as shown in Figure 6.1 (bottom) with a surface area close to the surface area of the final fracture in the previous section.

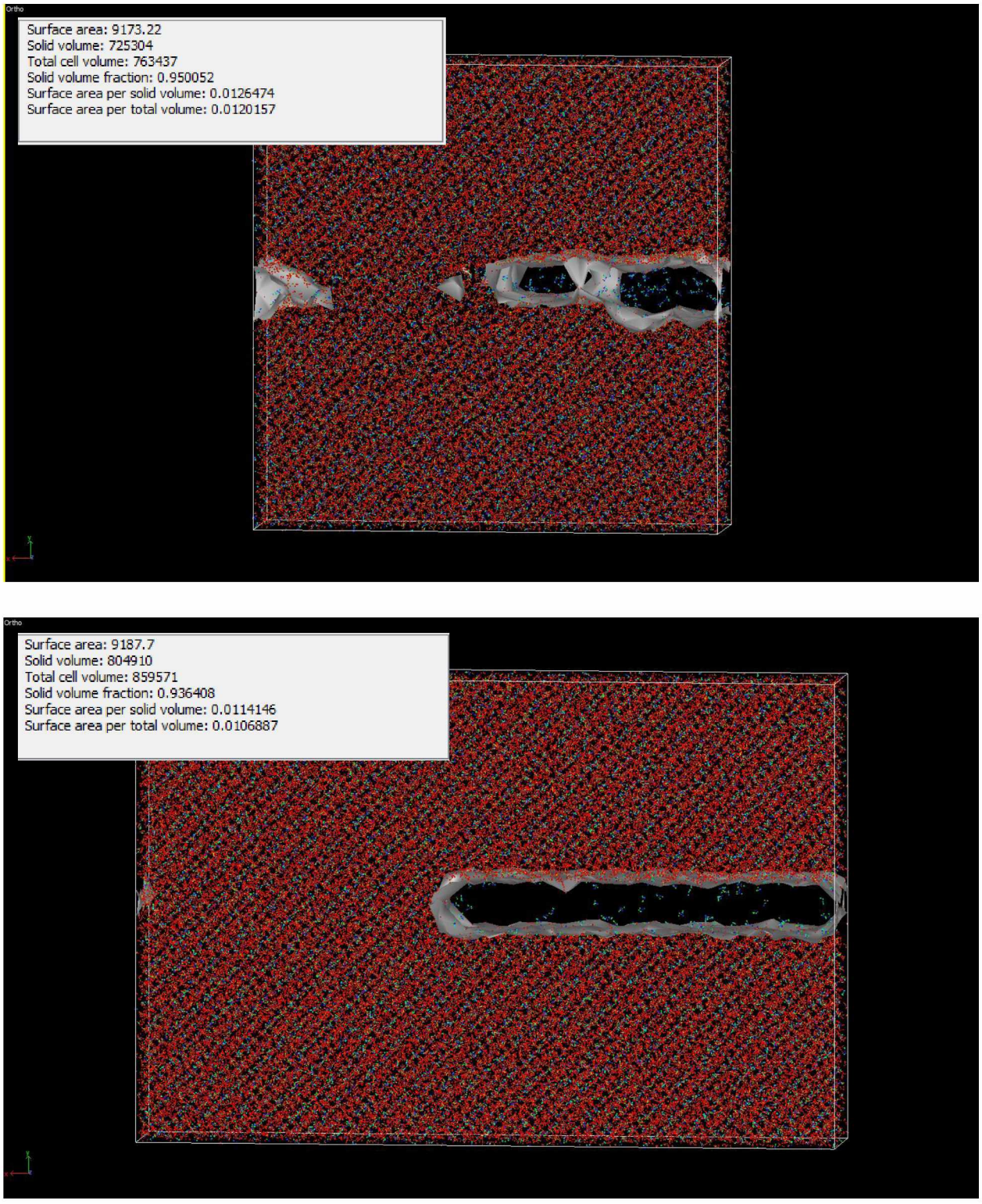

Figure 6.1: Comparison of actual fracture (top) and artificial fracture (bottom) with similar surface area

6.2GCMC vs *Fix Deposit*

After the cavity was created and the system equilibrated, CO_2 molecules had to be inserted into it. The idea was to inject a fixed number of CO_2 molecules into this created fracture by either using Grand Canonical Monte Carlo methods (GCMC) every few steps or depositing them all at once (*fix deposit*).

It was observed that, as the hydrate box relaxed, CH_4 molecules were released from the cages in the vicinity of the created fracture cavity. These gaseous molecules were randomly distributed in the cavity. They were important in quantifying the effectiveness of the process and therefore could not be deleted before inserting the CO_2 molecules in that region. GCMC involved inserting CO_2 molecules randomly based only on the potential (fugacity) in the region. This resulted in the CO_2 molecules being injected either on top of or very close to, the CH_4 molecules. They both came closer than the minimum interatomic distance and repelled each other with a large force. This caused the atoms to be thrown away outside the simulation box resulting in an error. Therefore, to avoid this error, *fix deposit* was used to inject all the CO_2 molecules almost all at once and then let them equilibrate.

This seems to contradict the understanding from the operational schedule of Ignik Sikumi in the sense that in their case the injection period lasted for a total of 14 days, whereas the soak-in period was just 2.5 days before production began. Therefore, the relative timescales of the two processes involved - CO_2 insertion into the cavity, and its diffusion into and replacement with the hydrates in the vicinity – is an important consideration. Although, it is known that the replacement reactions are extremely slow (Ohkagi et al. 1996), very little conclusive information is available about the process when performed in conjunction with fracture propagation, which is relatively a much faster process. Therefore, for the purpose of understanding the effectiveness of the two methods, without detailing their interface, it was assumed that all the CO_2 was deposited into the fracture in a very short duration and was then let to soak-in, or equilibrate, for a longer duration to give sufficient time for the replacement reaction. This also made sense because the

entire point of fracturing was to maximize the stimulated surface area in the least amount of time.

6.3 Final Simulation Protocol

The simulation box used in this study was a 18x12x3 unit cell box with a cavity of dimensions 120x15x35 Å originating at one side of the simulation box (see Figure 6.1 (B)). The system was then equilibrated for 40 ps in the NPT ensemble at P = 50 atm and T = 270 K. With the simulation box set up with a cavity for injection, 300 CO_2 molecules were deposited in the cavity using the *fix deposit* command in LAMMPS. The deposit was done maintaining a minimum distance of 2.5 Å, close to its bond length of 2.75 Å, to avoid overlap of non-bonded atoms.

As mentioned earlier, since the exact chronology and thermodynamic conditions of these processes in nature are unclear, simulations were run at conditions which provided insight into the phase changes as the CO_2 gas molecules diffused into the CH_4 hydrates. The following steps were followed:

1. CO_2 stabilization

   Since the CO_2 molecules were just deposited, and not inserted according to any potential or temperature constraints, it was necessary to bring them to the required conditions of system pressure and temperature. They were equilibrated for 100 ps using the NPT ensemble maintaining 50 atm and 270 K. It was observed that the CO_2 molecules achieved the P & T conditions pretty quickly.

2. System equilibration

   Once the entire system was at 50 atm and 270 K, CO_2 molecules were allowed to interact with the CH_4 hydrates using the NPT ensemble for 1 ns. The system pressure was gradually brought down from 50 atm to 20 atm in 200 ps and then the entire system continued to equilibrate at 20 atm and 270 K for the remaining 800 ps.

3. The system was analyzed at regular intervals measuring properties like Mean Squared Displacements (MSDs) of oxygen in water and carbon in CH_4; Radial Distribution Functions (RDFs) at the start and end to measure the structural changes; Coordination Analyses to determine the number of CH_4 released from cages; and cluster analysis to understand the evolution of the nanobubble.

To determine the effect of changing the temperature on the dissolution of CH_4 hydrates and evolution of CO_2 hydrates in the system, the simulations were run at 3 different temperatures: 260 K, 270 K, 280 K. These temperatures were chosen to represent three different phase existences at a pressure of 20 atm according to the system phase diagram in Figure 6.3. These conditions favor the replacement reaction according to similar MD studies by Bai et al. (2012) using similar force fields. They represent different stability regions for CH_4 hydrates, CO_2 hydrates, and mixed CH_4–CO_2 hydrates.

To see the effect of initial CO_2 concentration on the methane released, simulations were repeated with 450 and 600 molecules at 270 K. Finally, to study the effect of initial surface area on the efficiency of the replacement process, cases with different surface areas, but equal surface density of CO_2 molecules, were performed.

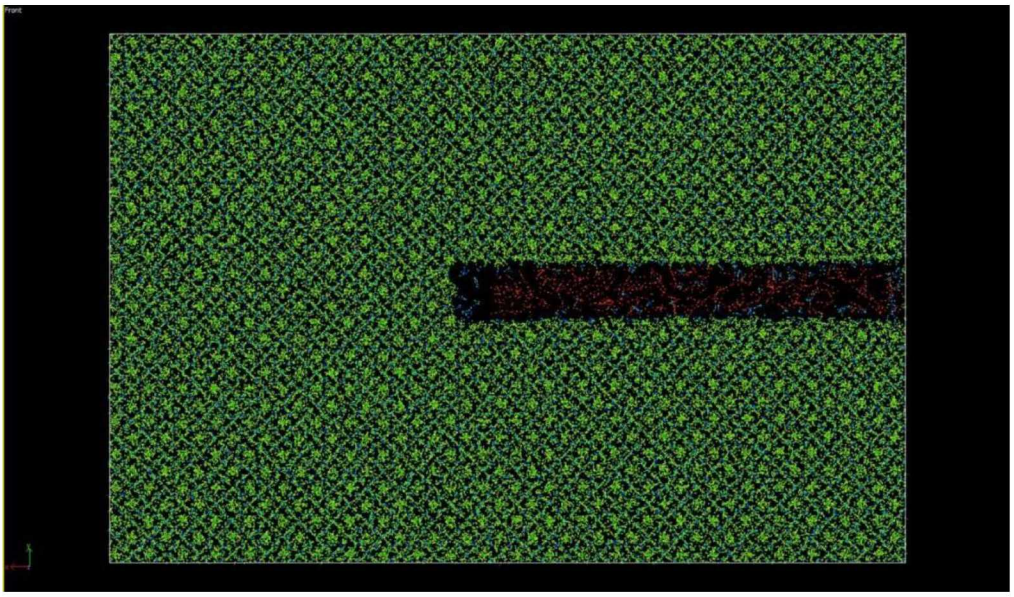

Figure 6.2: Final configuration with 300 CO_2 molecules in an artificial fracture at 270 K. Water is shown by yellow oxygen and green hydrogen spheres; methane is shown by dark blue carbon and light blue hydrogen spheres; CO_2 is shown in red.

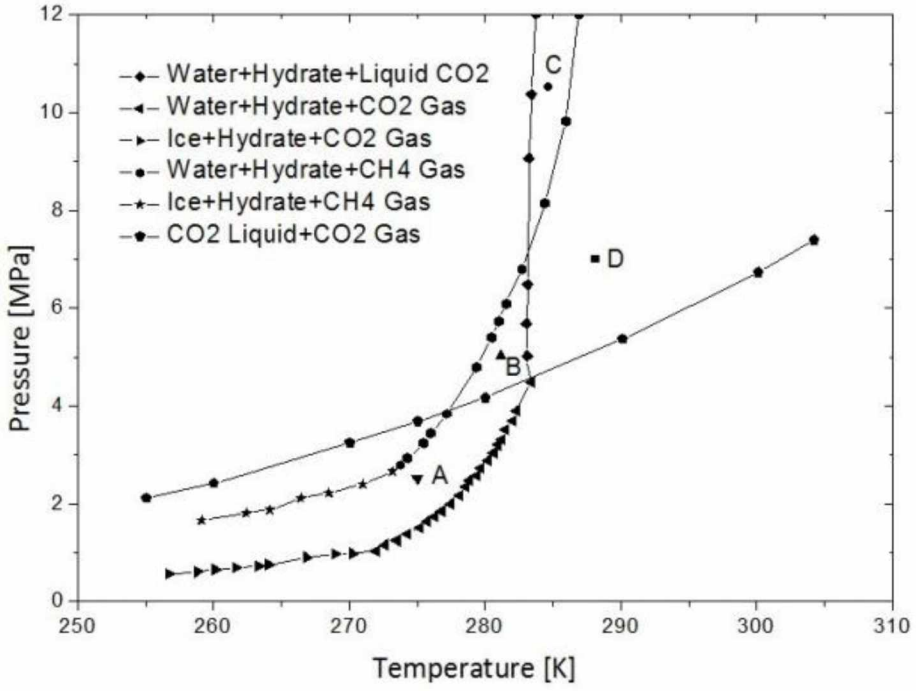

Figure 6.3: Diagram of CH_4, CO_2, and H_2O phase equilibrium. Figure adopted from Zhao et al. 2012

6.4 Mean Squared Displacement (MSD) Evolution at 270 K

Changes in the Mean Squared Displacement (MSD) of the oxygen atoms from water and carbon atoms from methane are a good measure of the phase changes and diffusion with time. MSD values can be used to obtain the self-diffusion coefficient. The self-diffusion coefficient describes the random motion of a particle in the absence of any gradients that would cause a mass flux.

There are two common ways to calculate the self-diffusion coefficient - from particle positions and from particle velocities. Theoretically, both yield the same results. Calculating self-diffusivity from velocities involves integrating the velocity auto-correlation function using the Green-Kubo relation. However, it has been found that simulations need longer to obtain a reliable self-diffusivity coefficient from velocities (Haile 1992). Therefore, the position data to estimate the self-diffusion coefficient (D) is used.

Einstein correlation is used to correlate MSD and self-diffusion coefficient values as a function of time.

$$D_x = \frac{1}{2d} \lim_{t\to\infty} \frac{\langle [r_x(t_o+t) - r_x(t_o)]^2 \rangle}{t} \qquad (12)$$

where D is the self-diffusion coefficient, and d is the dimensionality of the system. The numerator is the change in x-position between time $(t_o - t)$ and (t_o). Since a CH_4 hydrate system is isotropic (Jendi et al. 2016), the average diffusivity by using the average of the x, y, and z components or the mean squared displacement (MSD) between those time intervals is obtained.

The graph shown in Figure 6.4 displays the changes in MSD values of carbon in CH_4 molecules and the oxygen in water molecules as a function of time in femtoseconds at three different temperatures: 260 K, 270 K, and 280 K. The plateau of MSD values of water after approximately 100 ps could be arising from the cage effect. Such a cage effect, also observed in MD simulations of water in confined nanofilms (Han et al. 2010), indicates that the water is confined by the lattice

structure and the forces acting on it. All dissociation of the cages in hydrates around the cavity happens in the initial 100 ps. The average water molecule displacement after that remains constant indicating that the ratio of molecules as hydrates and liquid also remains constant after that time period. However, such a global average does not give insights into which hydrate cages break in particular.

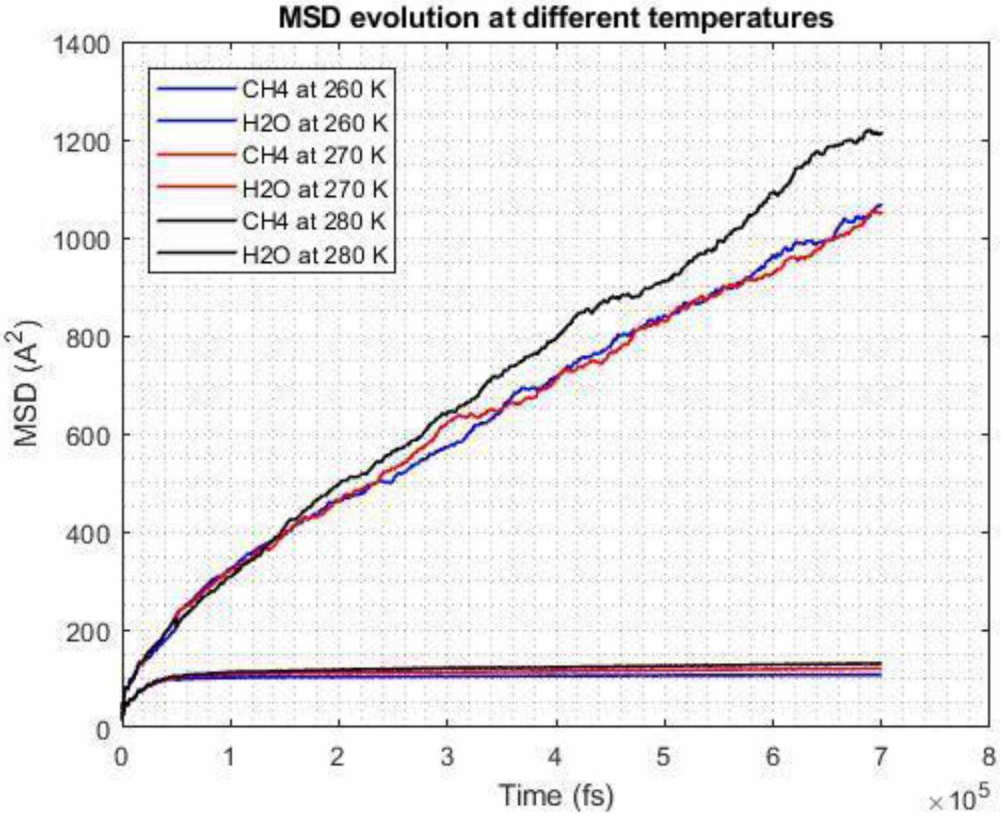

Figure 6.4: MSD evolution at different temperatures for CH_4 and H_2O molecules

The steady increase in the MSD values of carbon in CH_4, on the other hand, indicates the gradual transition of average methane positions from inherently solid hydrate cages to a more random fluid motion. The CH_4 molecules definitely have greater mobility as compared to their initial solid hydrate phase, as can also be seen in the snapshots of the simulation in Appendix A.

As seen, the diffusivity of CH_4 molecules tends to increase with temperature. The mobility of CH_4 at 270 K seems to be greater than that at 260 K up to 300 ps but then there seems to be no significant difference between the two.

Similarly, for water molecules, the diffusivity increases as the temperature increases. The slight vibrations at all the temperatures, even after the curves seem to plateau, are due to atomic vibrations around lattice sites without displaying diffusive behavior.

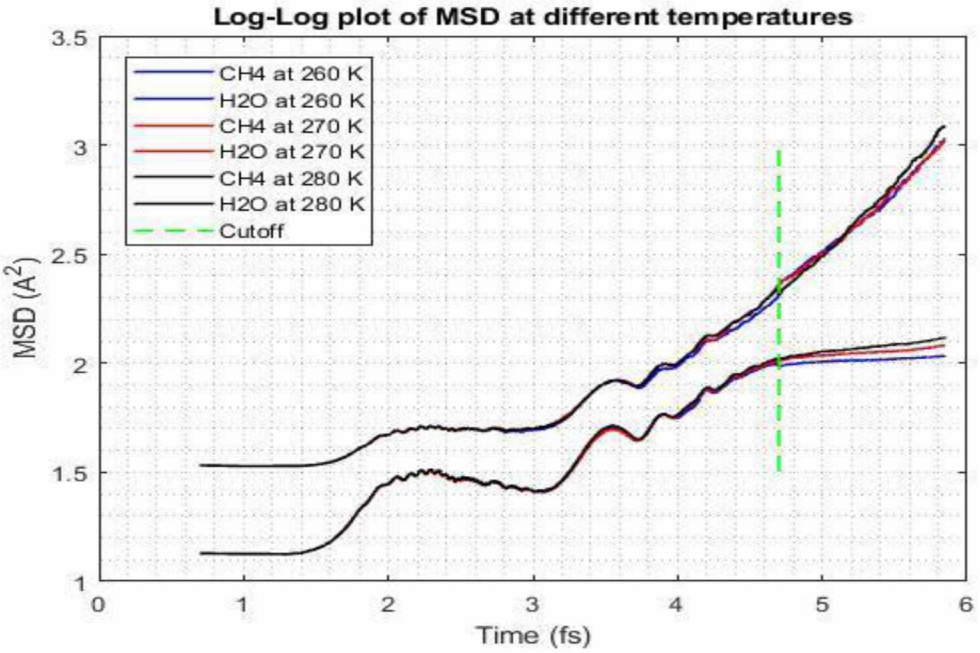

Figure 6.5: Log-Log plot of MSD at different temperatures for self-diffusivity calculations

To calculate the self-diffusivity coefficients for methane molecules, log-log plot in Figure 6.5, and the Einstein correlation are used. Using a simple linear least squares regression technique, the closest linear fit to the curves is obtained. Using the slopes, the following table lists the final results of the self-diffusivity coefficient calculations.

Table 6.1: Self Diffusivity Coefficients for CH_4 molecules

Temperature (K)	Slope	D, x10e-6 m^2/sec
260	0.5897	2.95
270	0.6152	3.08
280	0.6409	3.21

Table 6.2: Self Diffusivity Coefficient for H_2O using TIP4P/Ice

Temperature (K)	Slope	D, x10e-10 m^2/sec	D, x10e-10 m^2/sec (Picaud 2006)
260	2e-5	1	1.8
270	3e-5	1.5	2.5
280	5e-5	2.5	4.5

The calculations predict that the CH_4 molecules become more diffusive in the system at 280 K. This fact will also be validated by the RDF results in the next section. These values are almost 7-8 orders bigger than those reported in literature for cage-to-cage hopping mechanism (Kuhs et al. 2006, Peters et al 2008). This rapidity could be attributed to the spontaneous formation of nanobubbles. However, it is worth noting here that the diffusion coefficient of CH_4 through such a heterogeneous, non-equilibrium system consisting of CH_4 in several environments – hydrated, dissolved, in bubbles - will differ from the diffusion coefficient of CH_4 dissolved in water.

The diffusion coefficients for methane at this pressure and these temperature conditions were not available to compare. However, Keffer (2001) reported the self-diffusion coefficient for pure liquid methane as 2.5×10^{-8} m^2/sec and for pure

methane vapor at 2.1×10^{-5} m^2/sec using MD simulations. Shvab et al. (2014) prove that nonpolar solute particles, in this case, methane, diffuse much more slowly in water. Also, they tend to decrease the average diffusion coefficient of surrounding water molecules. However, diffusion properties inside bubbles are considerably different than those of bulk fluid and suggest enhanced diffusion.

For water molecules, the values are found in the same order of magnitude as that reported by Picaud (2006) using the TIP4P/Ice model for water, as seen in Table 6.2. However, a direct comparison is impossible because of the non-matching simulation pressures. The trend also seems to qualitatively agree with the results of temperature dependence of self-diffusion coefficients (Krynicki 1978).

6.5 Radial Distribution Function (RDF) at 270 K

The Radial Distribution Function (RDF), or Pair Distribution Function (PDF), is the probability density of finding an atom at a certain radial distance from another atom, divided by the probability density for the same event in a non-interacting system (Deserno 2004). It is a useful tool for describing the structural stability of a system. Figure 6.6 shows an illustration of RDF.

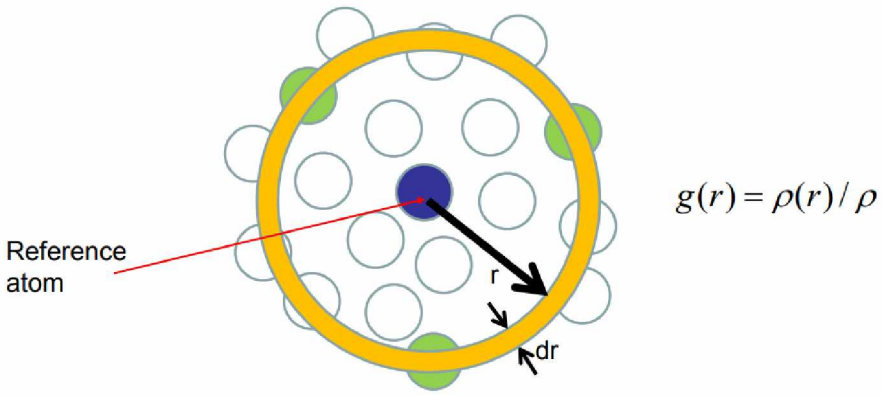

Figure 6.6: Illustration of Radial Distribution Function (RDF). Figure adopted from Buehler (2011).

The RDFs of (CH_4) carbon-carbon (CH_4), $g_{C-C}(r)$; (CH_4) carbon-oxygen (H_2O), $g_{C-O}(r)$; (H_2O) oxygen-oxygen (H_2O), $g_{O-O}(r)$; and (H_2O) oxygen-carbon (CO_2), $g_{O-C}(r)$; were evaluated at the end of NPT simulations of the system at 270 K. Ideally, these plots provide information on the local structure in a globally homogeneous lattice system. But in our case, these are calculated averages over the whole simulation box with inhomogeneous distribution of different phases: solid hydrate in some parts and fluid methane and water in others.

I use the Coordination Number modifier in OVITO to get the RDFs of the system. However, OVITO only calculates the global RDF ignoring the specific particle types. To overcome this limitation, the atoms not being evaluated were selected and deleted from the system. The Coordination Number modifier was applied only to the remaining atoms whose RDF was being evaluated.

Figure 6.7 (A-D) shows RDF plots for the 4 pairs of atoms mentioned earlier at the end of 2 ns of NPT simulations at P = 20 atm and T = 270 K.

The first peak in the methane – water RDF (B) at r = 2.75 Å corresponds to the coordination number of methane hydrates i.e. 23. This is consistent with the results of earlier simulations (English & Macelroy 2003). The later peaks average to a very small value for higher distances as their only interaction is at the boundary of the large gas bubble. Also, because of low methane solubility in water, there is limited representation of methane – water interaction in the aqueous phase.

The CH_4-CH_4 RDF (A) peaks at a very high value of r = 6.3 Å and flattens out to a value of 1 at higher cutoff values of ~35 Å (not shown here). This reflects the presence of one large gas bubble and remaining solid methane hydrate structure. These results again are in excellent agreement with the neutron diffraction results for gas hydrates (Koh et al. 2000) and other molecular dynamics simulations (Jiang et al. 2007, English & Macelroy 2003). The asymmetry of the profile is because of the occupation of both small and large cages, as confirmed in simulations by Tse et al. (1983).

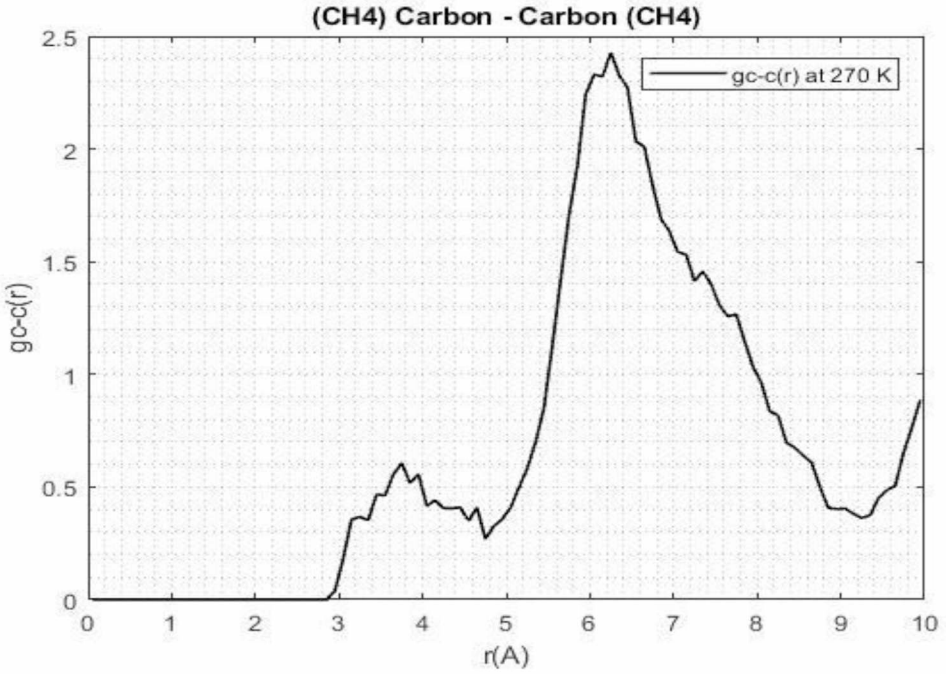
(CH4) Carbon - Carbon (CH4)
gc-c(r) at 270 K
gc-c(r)
r(A)
0
0.5
1
1.5
2
2.5
0
1
2
3
4
5
6
7
8
9
10

(A)

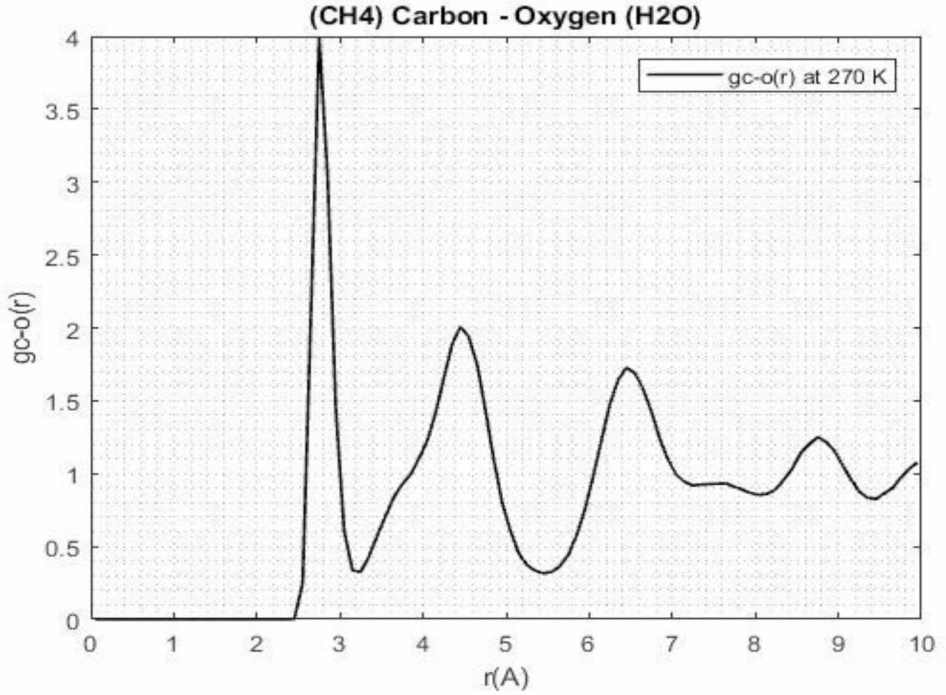
(CH4) Carbon - Oxygen (H2O)
gc-o(r) at 270 K
gc-o(r)
r(A)
0
0.5
1
1.5
2
2.5
3
3.5
4
0
1
2
3
4
5
6
7
8
9
10

(B)

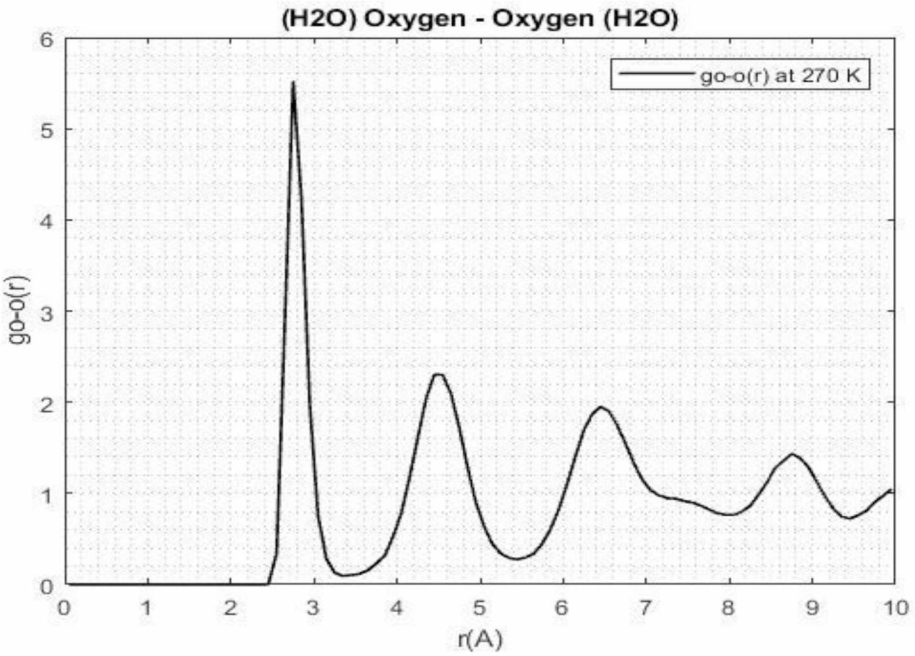

(C)

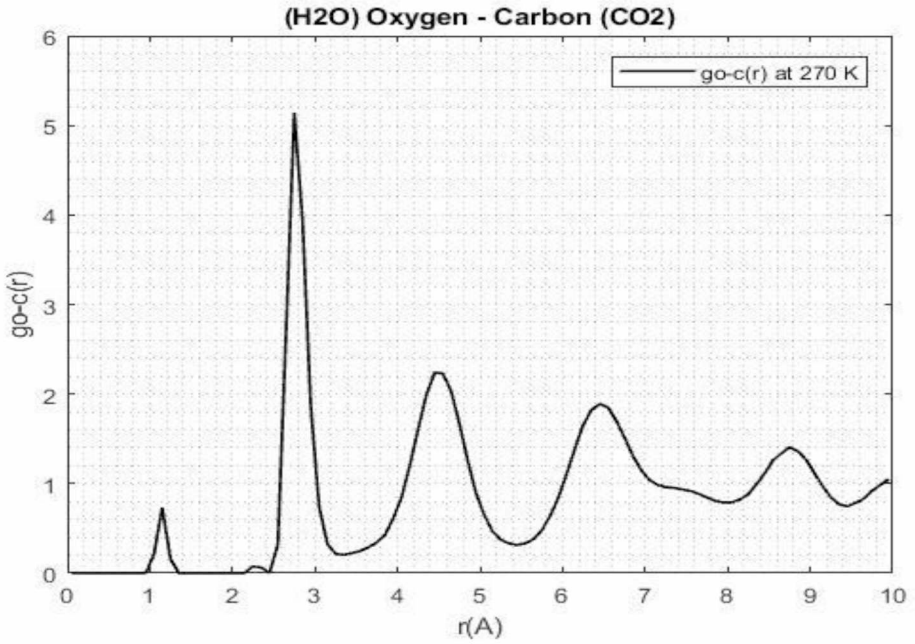

(D)

Figure 6.7: Variation in RDFs for pairs at end of 1 ns of NPT simulations at 270 K. (A) RDF of CH_4-CH_4, $g_{C-C}(r)$; (B) CH_4-H_2O, $g_{C-O}(r)$; (C) H_2O-H_2O, $g_{O-O}(r)$; and (D) H_2O-CO_2, $g_{O-C}(r)$.

As for the H_2O-H_2O RDF in (C), this gives the arrangement of the water molecules. The first two peaks, occurring at r = 2.75 Å and r = 4.45 Å, are the same as that of water (Chialvo et al. 2000) and also agree with other molecular dynamics simulations (Chialvo et al. 2002). This basically confirms the tetrahedral hydrogen bonding of the water molecules in gas hydrates. Also, the highest peak at r = 2.75 Å corresponds to the nearest distance between H_2O molecules separated from each other at approximately r = 2.78 Å (Geng et al. 2009) in hydrate structures.

Finally, for the H_2O–CO_2 RDF in (D), the uncharacteristic peak occurring at a very low cutoff distance and the remaining RDF similar to that of H_2O-H_2O indicate that all CO_2 molecules are dissolved in the water molecules. Lack of any significant CO_2 peaks also suggests that there is no CO_2 hydrate formation yet at the end of 2 ns and given temperature-pressure conditions.

The RDFs of all the pairs were compared at 3 different temperatures - 260 K, 270 K, and 280 K – at the end of a NPT simulation for 700 ps and P = 20 atm. The results are shown in Figure 6.10 (A-D).

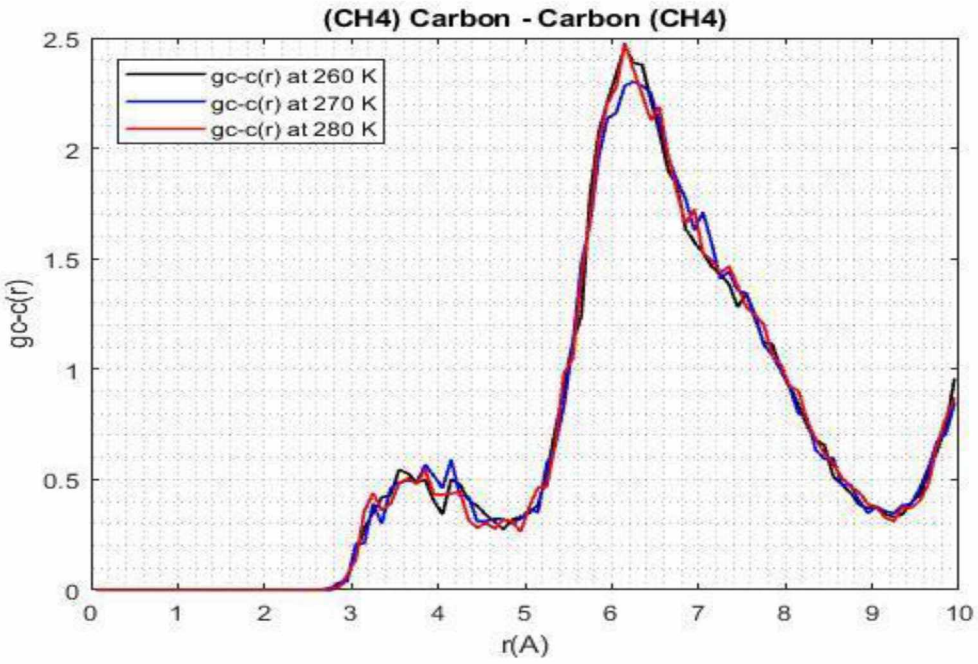
(CH4) Carbon - Carbon (CH4)
gc-c(r) at 260 K
gc-c(r) at 270 K
gc-c(r) at 280 K
gc-c(r)
r(A)

(A)

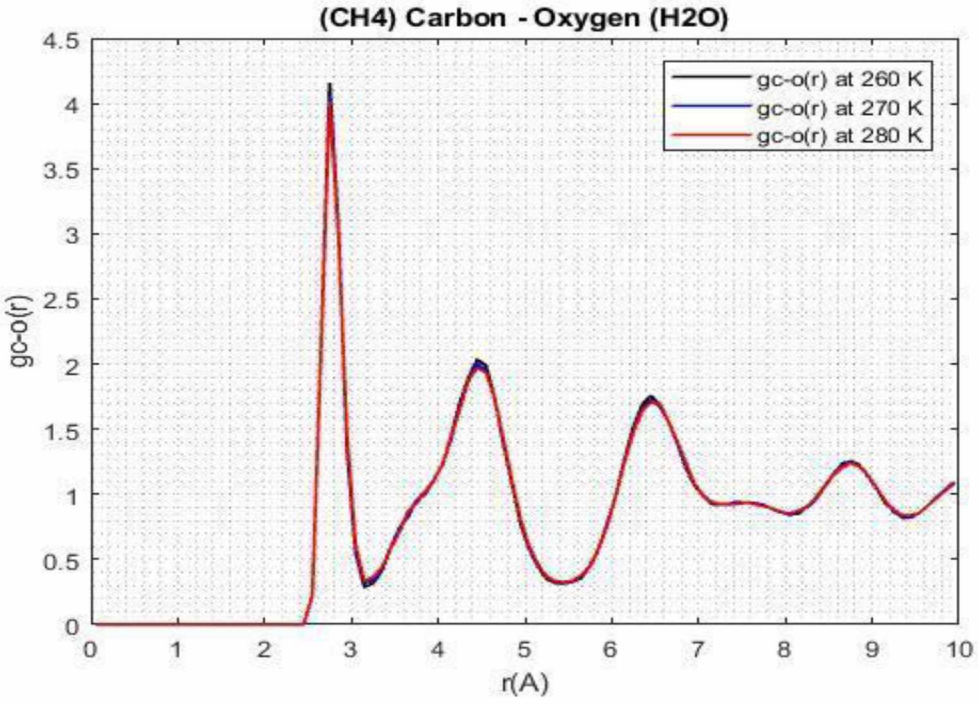
(CH4) Carbon - Oxygen (H2O)
gc-o(r) at 260 K
gc-o(r) at 270 K
gc-o(r) at 280 K
gc-o(r)
r(A)

(B)

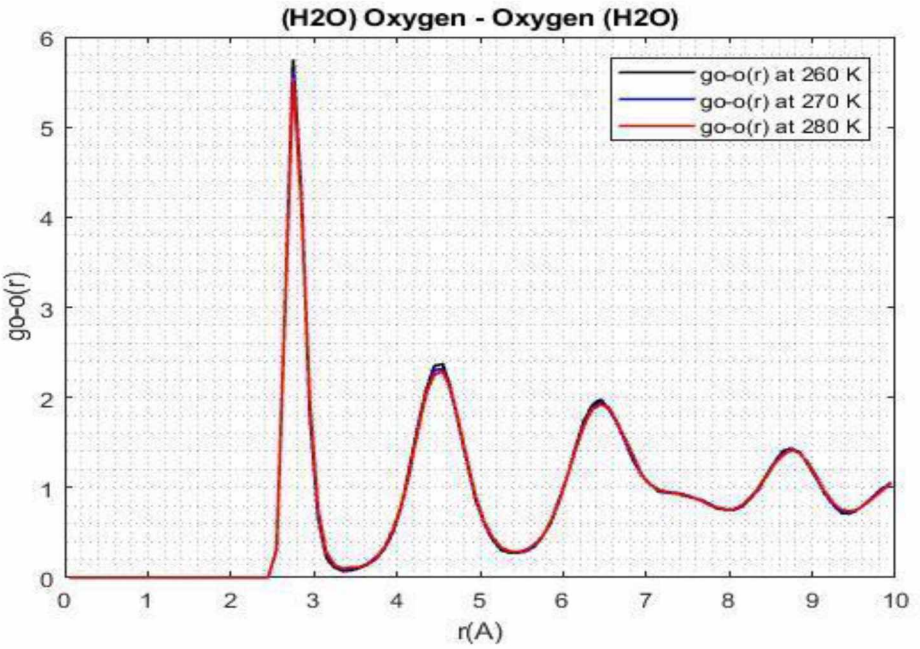

(C)

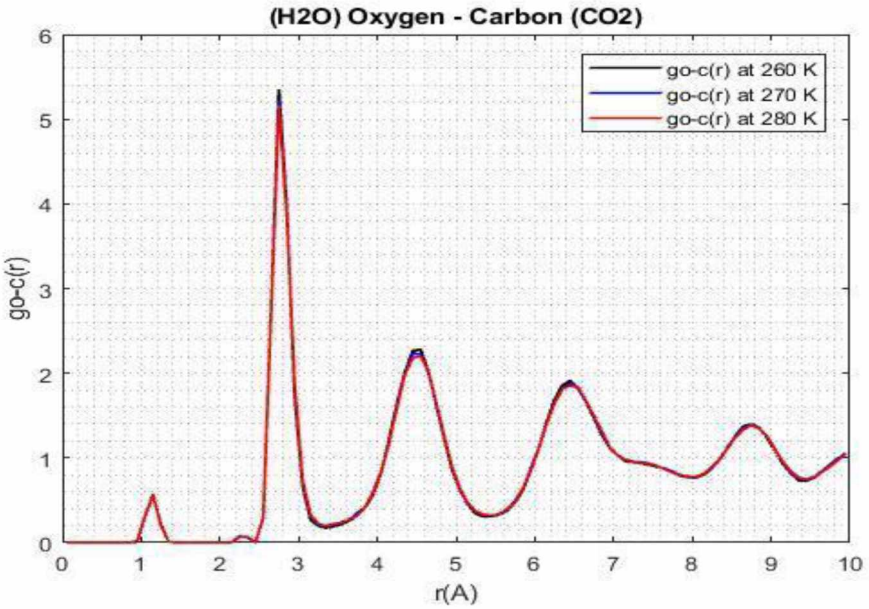

(D)

Figure 6.8: Comparison of RDFs for pairs at end of 1 ns of NPT simulations at different temperatures. (A) RDF of CH_4-CH_4, $g_{C-C}(r)$; (B) CH_4-H_2O, $g_{C-O}(r)$; (C) H_2O-H_2O, $g_{O-O}(r)$; and (D) H_2O-CO_2, $g_{O-C}(r)$.

As can be seen from Figure 6.8 (B), (C), and (D), the peaks get lower and broader as the temperature increases. This is expected (Jiang et al. 2007) because, at higher temperatures, the overall energy of the molecules is higher. Earlier works have compared the molecular dynamics simulations' RDF results to those generated by empirical potential structure refinement (EPSR) fits of neutron diffraction data (Thompson et al. 2006) and have attributed part of the discrepancy to the neglect of quantum effects in the simulations. It has been shown that in simulations of both liquid water and ice Ih, the peaks on H_2O-H_2O RDF are lowered and broadened by the inclusion of quantum effects.

The lowered and broadened peaks of CH_4–CH_4 at 270 K as compared to that at 260 K indicates that greater dissociation of the hydrates with aggregation of gas molecules occurred at the higher temperature. The peak at 280 K shows an unexpected behavior as compared to those at 260 K and 270 K. One would assume it to be lower than the others since a greater number of CH_4 molecules would dissociate out of the cages and form a part of the bubble at that temperature. However, as seen in the previous section, the molecules in smaller clusters are more diffusive at higher temperatures and hence, tend to agglomerate faster. They may be outside the cages but are close to enough number of H_2O molecules to be considered hydrates according to the cutoffs. This could also be due to the greater accumulation of water molecules near the mouth of the fracture at higher temperatures, beginning to form secondary methane hydrates. It is, however, difficult to qualify these secondary hydrate formations in the scope of this work as explained later.

The effect of temperature on the hydrogen bonding of the hydrates can also be understood better from the RDF curves to some extent. The hydrogen bond length has been shown to have a quadratic dependence upon temperature (Dougherty 1998). And since, the bond strength is linearly related to the bond length in second order it should also quadratically depend on temperature. The first two peaks in Figure 6.11 depict the covalent and hydrogen bonding interactions, respectively. As

the temperature increases, the hydrogen bond strength decreases, as reflected by the lower and broader second peak, to comply with the thermal expansion whereas the first peak is higher and sharper, depicting how the covalent bond strength increases to counteract the same thermal expansion. This opposite behavior has been previously identified for hydrogen bonding networks (Goryainov 2012).

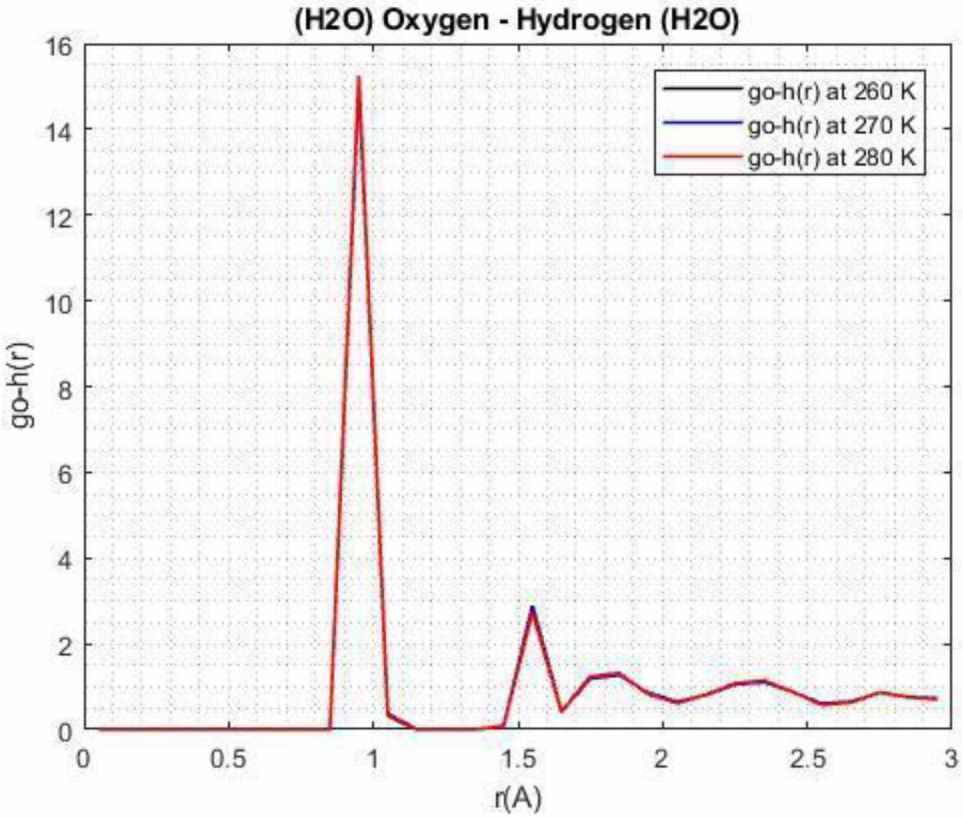

Figure 6.9: Comparison of RDFs for H_2O-H_2O, $g_{O-H}(r)$ pair at end of 1 ns of NPT simulations at different temperatures

6.6 Nanobubble Formation – Qualitative Analysis

It has been widely reported (Alavi & Ripmeester 2010; Bagherzadeh et al. 2012, 2015) that the hydrate phase decomposition occurs in a concerted fashion, with cages in the first row at the hydrate/fluid interface dissociating together. This was also observed in simulations here, although the relative timescales were significantly different due to different initial energies of the molecules and different degrees of superheating. It was observed that the decomposition front first stimulates the cages at the interface and then very quickly moves inward into the hydrate phase. It only progresses to a certain limit after which no significant decomposition occurs. This limit might be defined by the initial number of CO_2 molecules and the initial available surface area for the interaction.

It was observed that the CH_4 molecules are released from the cages around the stimulated area and then agglomerate to form CH_4-rich nanobubbles in the liquid region. While some of the CH_4 molecules are still dissolved in the liquid phase, after reaching the saturation limit in water, they begin to agglomerate in the vicinity of the hydrate/liquid interface. Unlike other previous works (Bagherzadeh et al. 2015; Lui et al. 2017), which had smaller clusters coalescing into multiple bigger nanobubbles with time, only one nanobubble was observed in this case. This is attributed to the fact that the simulation boxes in the earlier cases had different initial configurations with at least 2 hydrate/gas interfaces. The current work, however, only had 1 hydrate/gas interface created by the artificial fracture. Also, this could be due to the limited size of the simulation box such that the bubble absorbs all the released methane molecules from the surrounding liquid and prevents the formation of the second bubble. These factors may result in absence of multiple nanobubble embryos but very accurately predict progress of the system behavior.

It is observed that as the CH_4 hydrates decompose and molecules enter the fracture cavity, the CO_2 molecules begin to diffuse into the liquid region. The injected CO_2

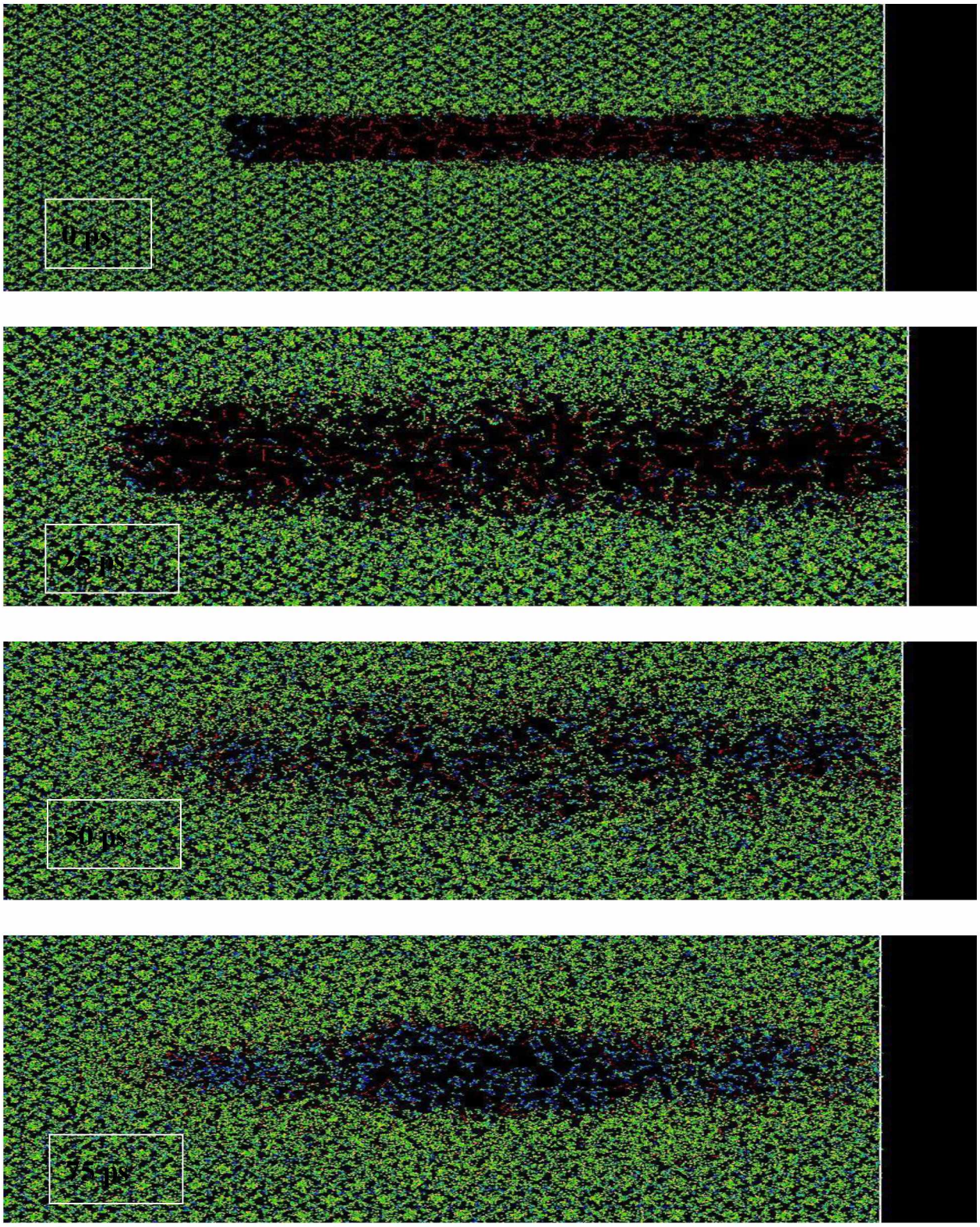

Figure 6.10: Snapshots of first 75 ps of NPT simulation with 300 CO_2 molecules at 270 K and 20 atmospheres.

and released CH_4 molecules seem to diffuse into the newly formed liquid region. As the simulation progresses, clusters of CH_4 molecules appear to accumulate and grow in size. At the same time, CO_2 molecules appear to diffuse further away from the interface into the liquid region. After about 100 ps, a primarily CH_4 cluster taking shape is distinctly seen, with almost all the CO_2 molecules dissolved in the liquid around it. Due to the application of periodic boundary conditions, the bubble takes up a cylindrical shape in order to minimize the interfacial tension (Lui et al. 2017). The author thinks that the bubbles may not even coalesce into cylindrical shapes if the simulation box used was big enough.

The possibility of coalescing is also dependent on the presence of a gas reservoir. Since here, unlike earlier simulations, there was no free CH_4 gas reservoir adjacent to the hydrate phase, the methane clusters remain in the liquid phase and form one single nanobubble.

Figure 6.13 (A) illustrates the snapshot of CH_4 and H_2O molecules at the end of 2 ns. The CH_4 molecules are depicted by red spheres whereas the green spheres represent the water molecules. As can be seen, the CH_4 molecules exist in all three environments: in undissociated hydrate cages, dissolved in the liquid phase, and in bubbles. The bubble has elliptical (*xy* plane) and rectangular (*yz* plane) cross sections.

Correspondingly, Figure 6.13 (B) illustrates the snapshot of CO_2 and H_2O molecules at the end of 2 ns. The CO_2 molecules are represented by red spheres and the water by green. It is seen that almost all the CO_2 molecules are dissolved in the liquid phase. This is expected as the solubility of CO_2 in water is high and very few CO_2 molecules were injected in the first place. However, this also qualitatively proves the point that CO_2 hydrate formation is a much slower process compared to CH_4 hydrate dissociation.

The accumulation of CH_4 in water is controlled by two opposing driving factors: (1) the rate of CH_4 entering the liquid, i.e., hydrate dissociation, and (2) the rate of CH_4

diffusing out of the liquid phase and into the gas phase. It is the balance of these two rates that determines the accumulation of CH_4 in bubbles. The rate of hydrate dissociation in this case at 270 K is faster compared to the rate of CH_4 diffusion into the gas phase. This results in insufficient time for them to diffuse out and therefore, leads to their accumulation in the aqueous phase in the form of embedded CH_4-rich bubbles.

Another point worth noting is that in the case of Bagherzadeh (2015), the bubbles form at the hydrate/liquid interface. On the other hand, in another work by Yagasaki (2014), the locations of bubble nucleation are distant from the hydrate cluster. Yagasaki et al. (2014) attribute this fact to the differences in the degrees of superheating. Bagherzadeh (2015) performed simulations at 340 K whereas Yagasaki (2014) performed at 292 K. The expected results in our work should have been closer to Yagasaki (2014). However, based on extensive thermodynamic calculations, Buffett & Zatsepina (1999) have proposed several degrees of superheating in the system in the absence of a gas phase initially. This would account for the growth of bubbles at the hydrate/liquid interface even at lower temperatures in this work.

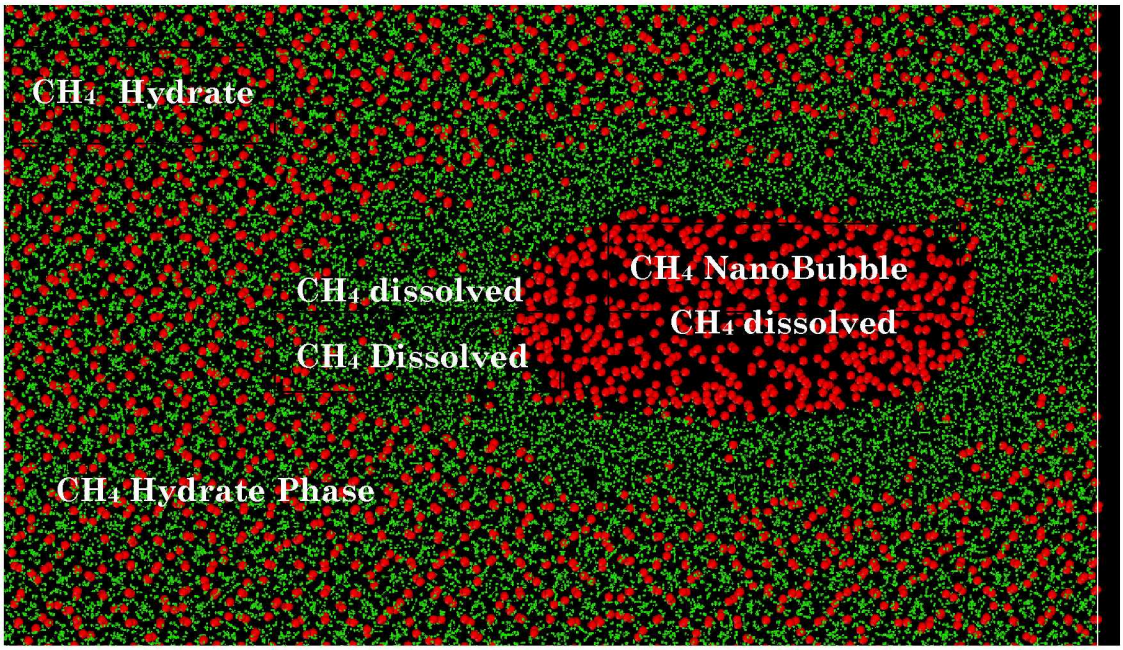

(A)

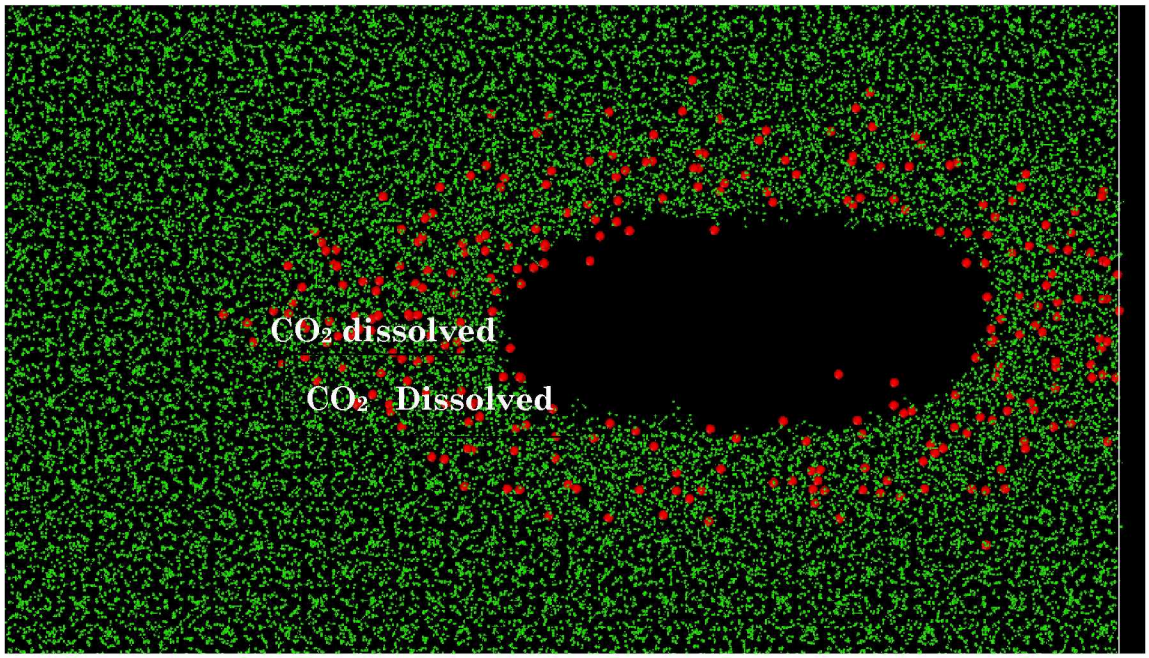

(B)

Figure 6.11: Snapshot of the system at end of 2 ns of NPT simulations showing different phases of CH_4 and CO_2 (A) Red spheres represent methane and green represent water. (B) Red spheres represent CO_2 and green represent water.

6.7 Nanobubble Formation: Quantitative Analysis

6.7.1 Cluster Analysis

In order to quantify the number of molecules in the bubbles, cluster analysis was performed with varying cutoff values of 4.5 Å, 5 Å, 5.5 Å, 6 Å, and 6.5 Å, respectively. This methodology is adopted from the recent work by Liu et al. (2017) analyzing similar systems. They define a cluster as a set of C atoms from CH_4 such that each C atom is within the specific cut-off distance from one or more atoms of the same cluster. The same convention of defining a bubble like them, "a cluster with the size more than 10 is classified as a bubble candidate" is used. The size is estimated based on the number of C atoms within the cluster. For example, in our case the smallest cluster could be of size 1, with no neighboring atoms within the cutoff, or 4275, with all C atoms within the same cluster.

The graph in Figure 6.14 presents the amount of CH_4 molecules in each of the candidate clusters for each of the cut-off for up to 2 ns of simulations at 270 K. The analysis was done using the Cluster Analysis Tool in the OVITO package on C atoms from CH_4 selectively. The detailed result of the number of clusters and their respective sizes is provided in Appendix B. The analysis was done at cut-off values close to the ones used by Liu et al. (2017). Cutoff values above 6.5 Å were not considered as all the CH_4 molecules seemed to appear in one single cluster above that.

Figure 6.15 presents only the clusters within reasonable cutoffs that estimate the amount of CH_4 in the main bubble. The reasonable cut-offs are selected such that the total amount of released CH_4 is approximately equal to that reported by the coordination analysis in Figure 6.16 at that particular moment at 270 K. As can be seen, the cut-off values seem to increase with time which indicates the merger of smaller clusters into the single larger bubble.

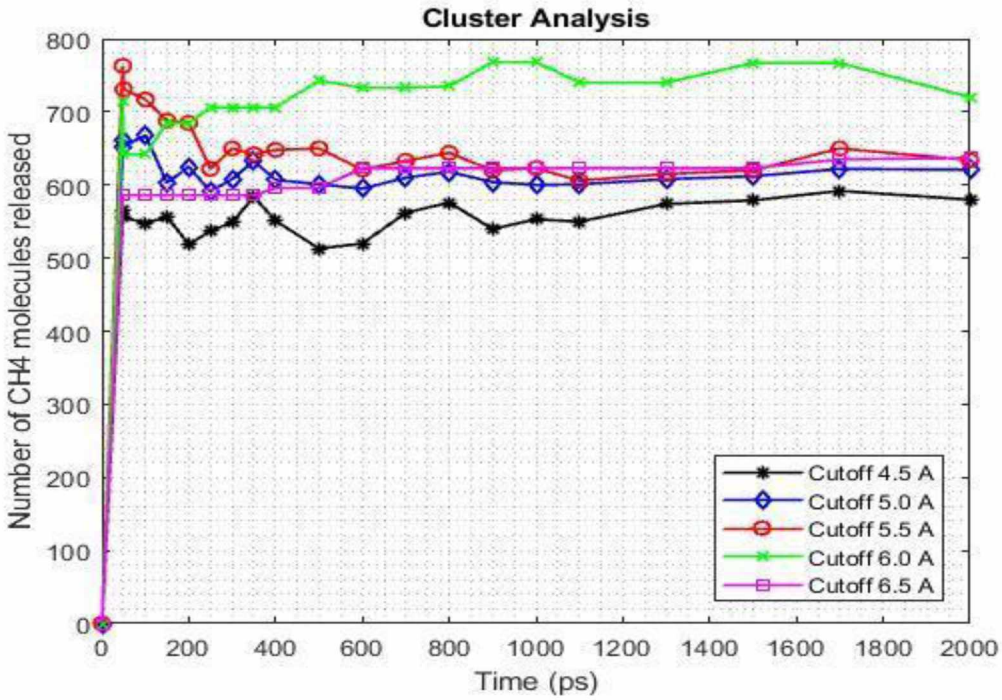

Figure 6.12: Total amount of CH_4 molecules in all the bubbles at 270 K with different cutoff sizes.

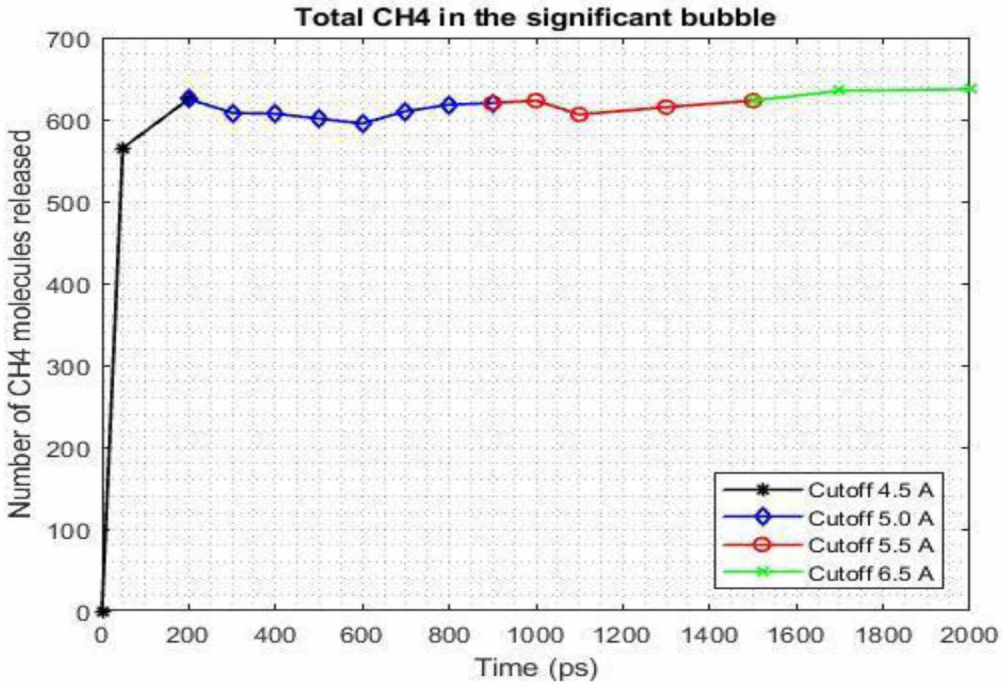

Figure 6.13: Amount of CH_4 molecules in the significant bubble and the corresponding cutoff size.

6.7.2 Coordination Analysis

The objective of stimulating the hydrate phase is to produce CH_4 molecules from it. Therefore, it is of utmost importance to investigate the number of CH_4 molecules released from the dissociated hydrate cages. To estimate this number, a rule similar to the one introduced by Yagasaki et al. (2014) and later modified by Liu et al. (2017) is adopted. It is assumed that a CH_4 molecule is in the hydrate cage if the number of water molecules surrounding it in the first hydrate shell (within 5.5 Å from the methane molecule) is greater than methane's hydration number of 23. Using OVITO selectively on C atoms of CH_4 molecules, the coordination number of all atoms that have more than 23 water molecules surrounding them is computed. This gives us the number of CH_4 molecules dissociated and free from the hydrate cages.

Figure 6.16 shows the evolution of the number of CH_4 molecules released with time for all three temperatures, 260 K, 270 K, and 280 K, for a total of 1 ns NPT simulations. As expected, the number of CH_4 molecules released is greater at higher temperatures. It is observed that as simulations progress, the number becomes almost constant at higher time steps. This seems to occur because of the way CH_4 molecules are counted in OVITO. At higher time steps, the molecules in smaller clusters are more diffusive at higher temperatures and tend to agglomerate faster. They may be outside the cages but close to enough H_2O molecules to not be counted in the coordination analysis. This could also be due to the greater accumulation of water molecules near the mouth of the fracture at higher temperatures, beginning to form secondary methane hydrates. It is difficult to qualify these secondary hydrate formations in the scope of this work as explained in the next section.

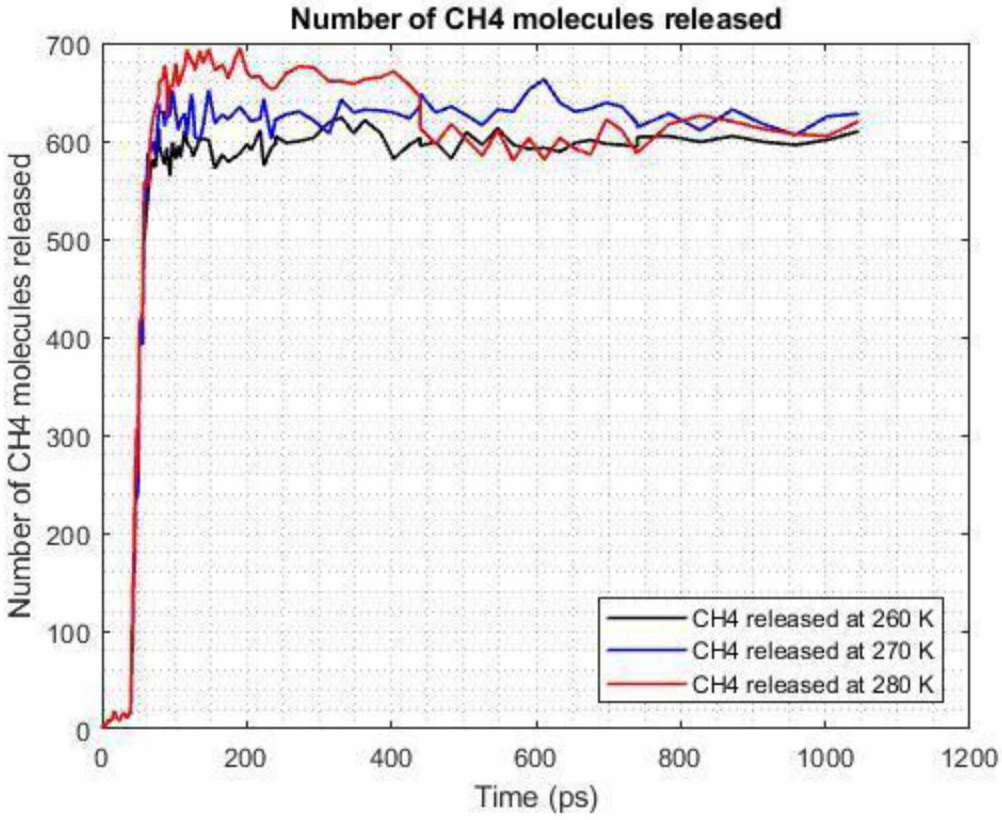

Figure 6.14: Total number of CH_4 molecules released at different temperatures

6.8 Formation of Secondary Hydrates Near Mouth of Fracture

One of the main concerns when proposing the idea of fracturing in a methane hydrate reservoir is the formation of secondary hydrates near the mouth of the fracture. This would block the path for the released gas and water molecules to leave the fracture and move towards the bottom hole of the well. Such a process would be best studied through simulations at the reservoir scale measuring the evolution of permeability near the mouth of the fracture. It is difficult to accurately quantify this phenomenon at the molecular scale.

The position of the formed gas bubble, and its movement with time could be an indication of the advancement of the gas and water molecules. As seen in the snapshots in Appendix A, the gas bubble tends to accumulate towards the center of

the fracture, at the hydrate/liquid interface, rather than move towards the mouth. The water molecules tend to accumulate near the mouth of the fracture blocking any connectivity of the gas molecules with the left face of the simulation box. It has been shown earlier that the gas bubbles eventually act as sites of nucleation for the formation of secondary hydrates (Bagherzadeh et al. 2015). The locally high concentration of CH_4 molecules could reduce the induction time for formation of hydrates as compared to that from 'fresh' solution. This is popularly known as the "memory effect" in hydrate systems. These facts indicate that there would, most probably, be the formation of secondary CH_4 hydrates near the mouth of the fracture at higher timescales. It is worth noting that all simulations here were performed at isobaric conditions with P = 20 atm at all faces, in the absence of any external pressure gradient. It would, however, be interesting to repeat these simulations with one of the faces of the box at a lower pressure to see if the released molecules have a tendency to migrate towards that face at longer timescales. To simulate this at the molecular scale is, however, not so trivial.

We primarily use the Berendsen et al. (1984) pressure control method in this work. This method is difficult to be applied in NEMD simulations with pressure gradients (Takaba et al. 2007). To resolve this issue, Alexiadis & Kassinos (2008) proposed the gravity-fed method. This method also would not satisfy the requirements here since it does not capture the fluid properties varying in the flow direction (Hanasaki & Nakatani 2006). Finally, the dual control volume grand canonical molecular dynamics (DCV-GCMD) method was considered (Heffelfinger & van Swol 1994). DCV-GCMD has been successfully applied to study flow in carbon nanochannels and to understand adsorption and diffusion phenomena in shale plays, but proved difficult to use in the case of an evolving fracture boundary. Therefore, the pressure-gradient driven scenario was left out of the scope of this current work.

6.9 Effect of CO_2 Concentration on Number of CH_4 Released

Figure 6.17 shows the number of CH_4 molecules released with a different number of CO_2 molecules injected into the cavity initially. It can be seen that the diffusion-driven mass transfer is directly proportional to the initial CO_2 concentration. The simulations were conducted at 270 K and 20 atmospheres for three cases of increasing numbers of CO_2 molecules – 300, 450 and 600, respectively. The CH_4 released with 450 CO_2 molecules is more than twice the CH_4 released with 300 CO_2 molecules. CH_4 released with 600 CO_2 molecules is greater than both cases. However, the increase of CH_4 molecules released with 600 CO_2 molecules as compared to 450 CO_2 molecules is less than the increase when an injection of 450 and 300 CO_2 molecules is compared in 1 ns.

This behavior was observed in previous experiments by Birkedal et al. (2015) and in molecular simulations by Sujith & Ramachandran (2016). However, since the experiments studied the exchange under continuous CO_2 flow, it is difficult to establish a direct correlation. The increased dissociation of CH_4 hydrate cages, in this case, can be attributed to greater heat liberation during the exchange. It was also observed that the higher number of CO_2 molecules stimulated greater hydrate volumes and penetrated deeper into the simulation box as shown in snapshots in Appendix A.

It was seen that the higher the number of CO_2 molecules, the steadier the growth of the gas nanobubbles. However, looking at the still increasing slope of line with 600 CO_2 in Figure 6.17 at the end of 1 ns, it took longer for the hydrate dissociation to reach equilibrium in this case. The increase in slope with 450 molecules is gradual whereas the slope with 300 molecules is almost flat after 700 ps. This indicates that the rate of methane hydrate dissociation increases with the initial CO_2 concentration. Therefore, an increase in initial CO_2 concentration results in more efficient dissociation of methane hydrates and will thereby improve the rate of displacement in longer simulations.

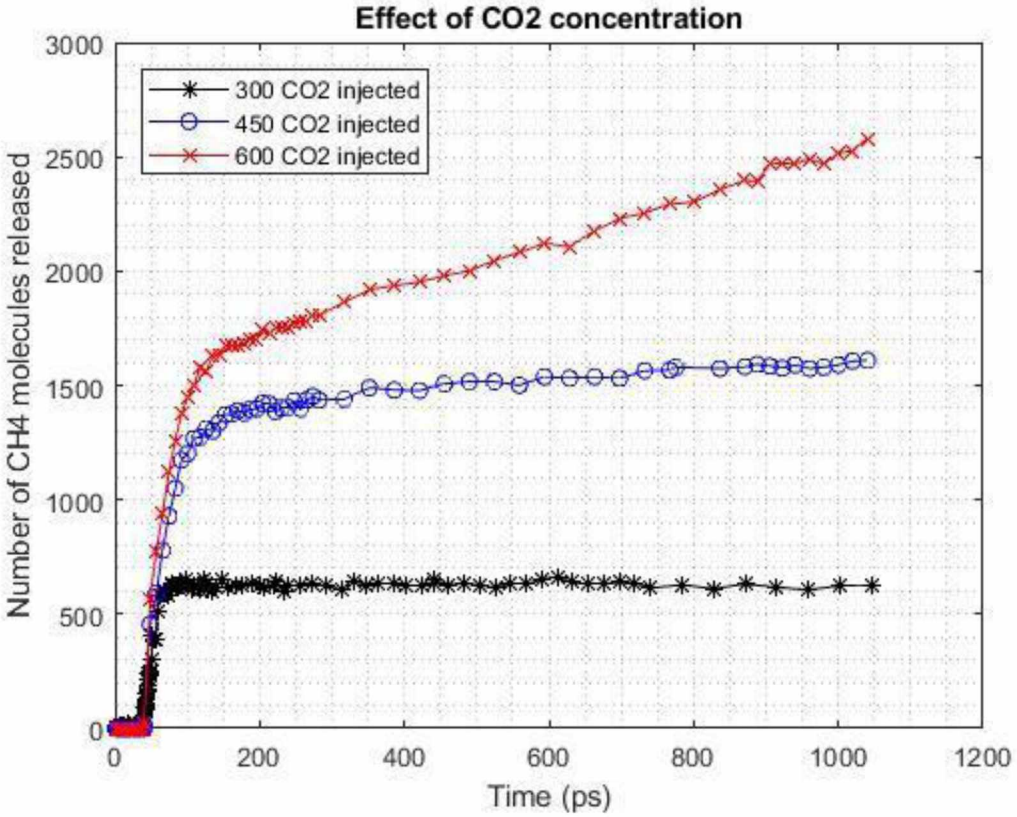

Figure 6.15: Comparison of number of CH_4 released with different initial CO_2 concentration

6.10 Effect of Surface Area on Number of CH_4 Released

Using Raman spectroscopy, Uchida et al. (2000) were the first to prove that replacement of CH_4 hydrates with CO_2 occurs at the contact surface area between the two. Ota et al. (2005) built simplistic kinetic models based on their experimental data for the *in situ* replacement and found that surface area plays a very important role in the initial stages of the process. Based on activation energy comparisons, they concluded that the CH_4 hydrate system underwent surface replacement during the initial contact with CO_2. This surface reaction later transformed into a diffusion limited process. Such a transition in the mechanism is evident in our work as well from the high initial rate of hydrate dissociation to the nanobubble stabilization and flattening slope of number of CH_4 released at longer times.

Therefore, if the replacement process is limited by diffusive transport, increasing the surface area available initially would result in faster and greater CH_4 hydrate dissociation and, possible, CO_2 hydrate formation (Jung et al. 2010). There is some supportive experimental evidence, but no molecular simulations were found exploring the effect of the surface area further.

To understand the effects of surface area on the mass transfer process, the current system of an artificial fracture with 300 CO_2 molecules was modified to increase the initial surface area. The number of CO_2 molecule per unit surface area was kept constant in all three cases to eliminate the effect of CO_2 concentration. Table 6.3 lists the details of the three cases.

Simulations were run in all cases at the same thermodynamic conditions of 270 K and 20 atm for 1 ns each. Figure 6.18 shows the number of CH_4 released as a function of time, estimated using the same coordination analysis methodology as in the previous sections.

Table 6.3: Details of cases with different initial surface area

Case ID	Fracture Surface Area (Å^2)	Number of CO_2 molecules injected	$\frac{\text{Number of } CO_2}{\text{Surface Area}}$
SA_1	9187.7 Å^2	300	0.0326
SA_2	11336.2 Å^2	370	0.0326
SA_3	13787.5 Å^2	450	0.0326

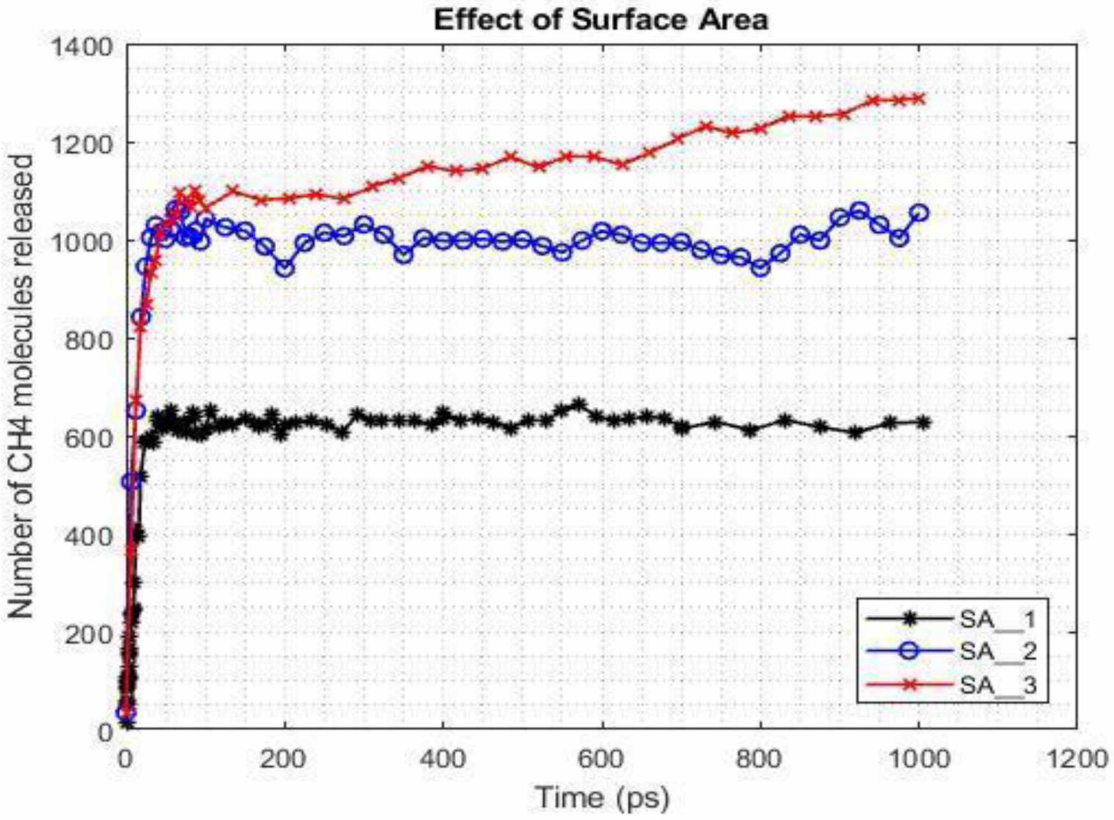

Figure 6.16: Comparison of number of CH_4 released with different initial surface area

As seen from the Figure 6.18, increase in the initial surface area available for mass transfer has a positive effect on the number of CH_4 hydrate cages dissociated. Although, the two are directly proportional, the increase between cases SA_1 and SA_2 is greater than the increase between SA_2 and SA_3. This could be because in case of SA_3 the injected CO_2 dissociates the hydrate cages across the length of the box, creating a system spanning region of fluid molecules. This limits the potential effect it could have as compared to a system with larger dimensions without the boundary effects coming into play.

Another interesting observation in these simulations is the formation of multiple nanobubbles at larger surface areas. These multiple nanobubbles do not coalesce in the 1 ns of simulations. Interestingly, there was 1 nanobubble in SA_1, exactly 2 nanobubbles in SA_2 and 3 nanobubbles in SA_3 at the end of 1 ns. The formation of these pseudo-stable nanobubbles and the relatively slower increase in released CH_4 after that, confirm the theory proposed by Ota et al. (2005). The initial stages of surface reaction driven dissociation led to the rapid formation of nanobubbles and the dissociation process slowed down in the diffusion driven regime afterward. It would, however, be interesting to see the effect of these nanobubble formations on the number of CH_4 released at longer timescales.

6.11 Comparing Effects of CO_2 Concentration and Surface Area

In the previous sections, it was shown that both the initial CO_2 concentration and the initial surface area have a significant positive effect on the dissociation of CH_4 hydrates. To understand the parameter which has a greater effect, two separate situations were compared. Another simulation was run with 600 CO_2 molecules in the corresponding surface area keeping the ratio constant. However, to accommodate the high surface area of 18369.7 $Å^2$ corresponding to 600 CO_2 molecules, two cavities of equal surface area were created as shown in Figure 6.19. It would be unrealistic to consider this a case of multiple fractures since the two cavities are practically within the same rock pore, just a few Å from each other. The

two situations compared had the same number of CO_2 molecules injected into cavities with different surface areas.

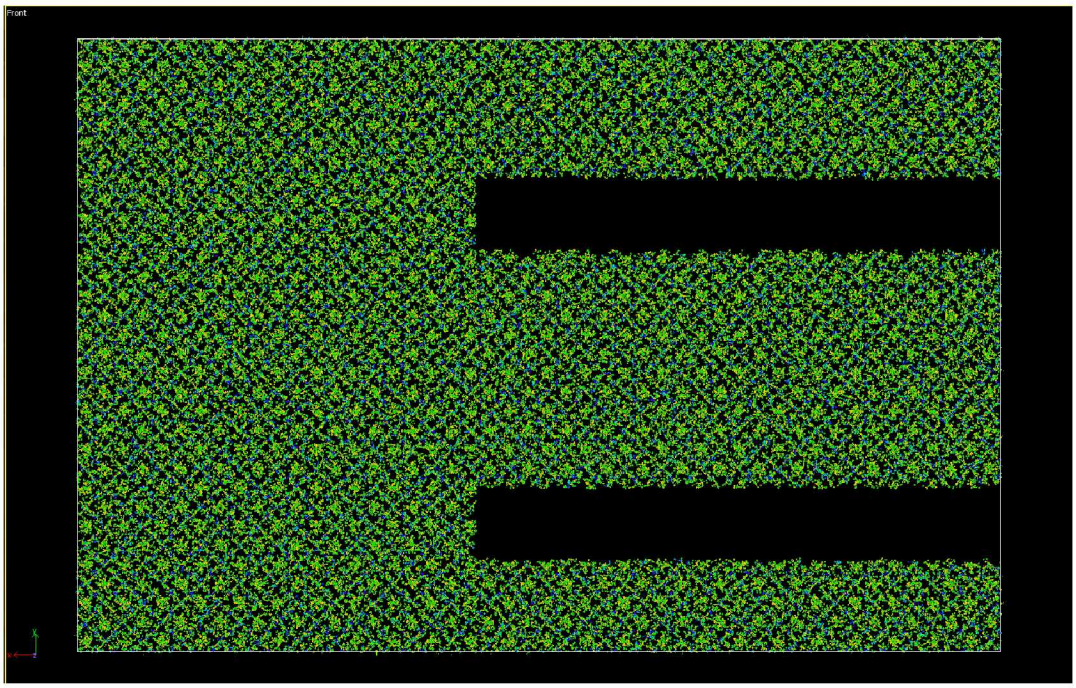

Figure 6.17: Snapshot of initial configuration with 2 cavities

The number of CH_4 released in each case is shown in Figure 6.20 for comparison. The CH_4 released in the case of higher CO_2 concentration is more in both situations. Also, the greater slope of lines with higher CO_2 concentration suggests that the rate of dissociation in the diffusion regime is also more positively impacted with higher initial CO_2 concentrations as compared to the higher surface area. Thus, the initial CO_2 concentration clearly has a greater positive effect on hydrate dissociation than the initial surface area. This set of simulations also lays the groundwork for further exploration to study the effect of having multiple interfaces on the replacement reaction from a theoretical point of view.

Table 6.4: Details of cases comparing variations in CO_2 concentration and surface area

Case ID	Number of CO_2 molecules injected	Fracture Surface Area (Å²)	$\frac{Numbe\ of\ CO_2}{Surface\ Area}$
450_SA_1	450	9187.7 Å²	0.0489
450_SA_3		13787.5 Å²	0.0326
600_SA_1	600	9187.7 Å²	0.0653
600_SA_4		18369.7 Å²	0.0326

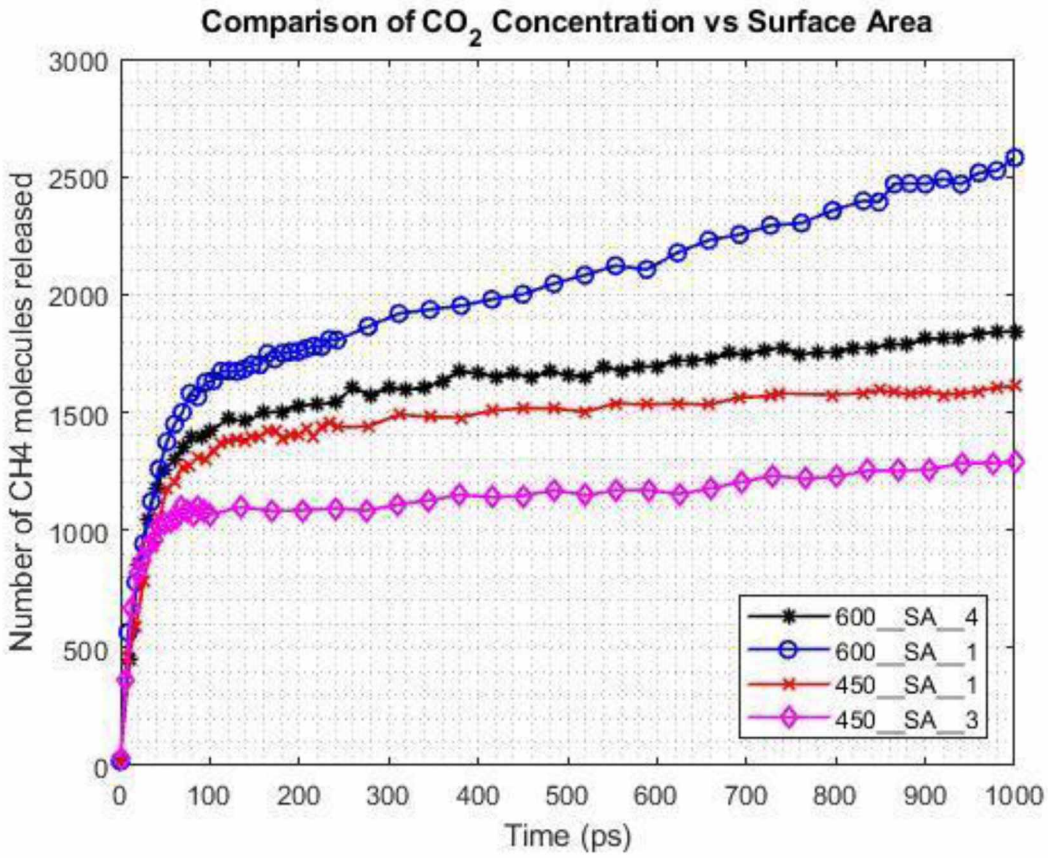

Figure 6.18: Comparison of effect of different initial CO_2 concentration and initial surface area on number of CH_4 released

CHAPTER 7 CONCLUSIONS

During this work, a sI hydrate simulation box was created and equilibrated to study the effects of fracturing on the efficiency of CH_4–CO_2 *in situ* replacement process. All simulations were performed at the molecular scale using LAMMPS. The stress-strain behavior of the solid hydrate was validated and the Isothermal Young's modulus was estimated by the application of a constant uniaxial strain. A maximum strain of 0.20 was applied and the ultimate tensile stress occurred at a strain of ~14.8%. The value of Isothermal Young's modulus was found in very close comparison to previous studies. This validated the simulation box models developed and the interatomic interaction potentials used.

The hydrate structure was then subjected to a constant tensile loading at 270 K using the deformation-control technique. Surface area was observed to increase as the fracture propagated. It ultimately formed a system spanning crack and no further increase in surface area was observed after that. It was observed that the number of CH_4 molecules released increased as the fracture conductivity increased but did not vary much after the formation of the system spanning crack. These preliminary results make fracturing a promising primary technique to increase the permeability of the reservoirs and provide the surface area for further depressurization, thermal injection, or guest molecule interaction.

CO_2 injection into the fracture created in the previous section proved to be difficult. Therefore, an artificial fracture cavity of the similar surface area was cut into the simulation box and CO_2 molecules were deposited into this cavity. Since the system was almost immediately subjected to a decreasing pressure after injection, there was practically no soaking period for the liquid CO_2 to diffuse into the hydrates. All the mass transfer occurred during the pressure reduction and as the system equilibrated for a total of 1 ns of simulation. Simulations were performed to study the variation of temperature, CO_2 concentration, and surface area.

It was observed that the released CH_4 molecules agglomerate to form CH_4-rich nanobubbles in the liquid region in all cases. These nanobubbles formed in the vicinity of the hydrate/liquid interface and not near the mouth of the cavity. The CO_2 molecules were observed to diffuse into the liquid region and were not a part of the nanobubble. The formation of the nanobubbles was followed by a continual increase in the number of CH_4 molecules released. This shows that after the rapid surface-driven stimulation, the CH_4 hydrates continue to be dissociated by diffusion-driven mechanisms.

Temperatures evaluated here did not have a drastic effect on the replacement process. Greater mobility of molecules was observed at higher temperatures. The self-diffusivity coefficient was estimated using the Einstein correlation, and the values were found to be very close to the literature. The slight variation in values observed was due to the presence of the heterogeneous, non-equilibrium system consisting of CH_4 in several environments: hydrated, dissolved, and in bubbles.

The peaks of all pairs of Radial Distribution Functions, except CH_4-CH_4, got lower and broader as the temperature increased since the overall energy of the molecules increased. The lowered and broadened peaks of CH_4–CH_4 at 270 K as compared to that at 280 K indicates that greater dissociation of the hydrates with aggregation of gas molecules occurred at the higher temperature.

Cluster analysis was done to quantify the size and shape of the nanobubbles. It was observed that the small clusters eventually agglomerate to form one large nanobubble and they continue to grow in size following the diffusion-driven dissociation regime. Coordination number analysis, similar to that done for fracture analysis, showed that the number of CH_4 molecules released is greater at higher temperatures. The number became almost constant for all temperatures as the simulation progressed.

One of the concerns around using fracturing for hydrate-bearing sediments is the formation of secondary hydrates near the mouth of the fracture. In the current

simulations, water molecules tend to accumulate near the mouth of the fracture and the nanobubble moves inward towards the center. This could lead to a favorable condition near the mouth for the formation of hydrates. However, since there was no pressure gradient applied in these simulations, it is difficult to conclude what a driving force towards the wellbore during production would do to the nanobubble position and released water. The pressure-driven scenario was left out of the current work.

To see the effect of initial CO_2 concentration on the methane released, simulations were repeated with 450 and 600 molecules at 270 K. Simulations indicate that as the initial concentration of CO_2 molecules in the cavity increases, both the net amount of CH_4 molecules released and the amount of CO_2 molecules diffused increases. Therefore, an increase in initial CO_2 concentration results in more efficient dissociation of methane hydrates and will thereby improve the rate of displacement in longer simulations.

To study the effect of initial surface area on the efficiency of the replacement process, cases with different surface areas, but equal surface density of CO_2 molecules, were performed. It was seen that increase in the initial surface area available for mass transfer also has a positive effect on the number of CH_4 hydrate cages dissociated.

Finally, effects of the above two parameters were compared. It was seen that the initial CO_2 concentration clearly has a greater positive effect on hydrate dissociation than the initial surface area.

In conclusion, fracturing has the potential to increase the efficiency of the CH_4–CO_2 exchange process significantly. It not only provides the increased surface area but also helps in formation of more nanobubbles to promote continued CH_4 hydrate dissociation. However, longer simulations will have to be done, with the application of a pressure gradient, to make conclusions about long-term CH_4 production and formation of secondary hydrates near the mouth of the fracture.

CHAPTER 8 APLICABILITY AND FUTURE RECOMMENDATIONS

The concepts studied here are at a very early stage of research and there are several possibilities that could be attempted to effectively combine the two processes of fracturing and CH_4–CO_2 replacement. These possibilities will need to be validated at all stages of development: molecular dynamics simulations to understand the mechanisms; continuum scale modeling and experiments to optimize the interaction of the processes, and finally, field scale trials to establish the long-term applicability of the concept.

Common to all studies in this thesis is that the temperature-pressure conditions are chosen either in the CO_2-hydrate, CO_2/CH_4 mixed hydrate, or CH_4-hydrate stability regions. Therefore, any conclusions about the field scale fracture propagation and CH_4 release rates based on these MD simulations would be extrapolation. These simulations provide an insight into the hydrate strength and CH_4-CO_2 exchange process in an artificial fracture but lack the effects of host sediment characteristics, rock mechanics, and hydrate saturations.

It is critical to consider hydrate morphology to determine what the actual mechanism of any type of stimulation process would be. It would be interesting to repeat similar MD studies with the hydrate structure between silica layers to understand, upon the application of the stresses, where the fracture is most likely to propagate – in the hydrate crystal, in the rock matrix, or at the interface of the two.

It is also critical to differentiate between CH_4 release and CH_4 production. The simulations here do not use any pressure gradient to replicate the production scenarios. The CH_4 molecules are released from their cages as the hydrate is destabilized. The simulations are not run long enough to conclude anything about CH_4 production. There have been experimental studies confirming the discrepancy. However, the reasons for discrepancies between CH_4 production and CH_4 release are not yet clear. This would make a very interesting problem for using the multi-scale modeling approaches.

It is worth mentioning here that as the CO_2 molecules transition from 50 atm to 20 atm at a constant temperature of 270 K in cases here, they are transitioning from a liquid state to a gaseous state. The author injects liquid CO_2 at 50 atm and gradually starts reducing the system pressure to 20 atm where CO_2 is present in the gaseous phase in its pure form. This liquid to gas phase change (vaporization) results in expansion of the CO_2 bulk volume at the constant temperature. This can be seen in the initial few picoseconds of the simulation as the volume expands and later equilibrates, to a methane-rich nanobubble, with most of the CO_2 dissolved in the liquid water region. However, it would be interesting to ascertain the effect of this volume expansion on the methane hydrate dissociation.

Also, scaling up the concept and simulating at the reservoir scale would be required to confirm its applicability at the field scale. There are now several comprehensive hydrate modeling simulators available commercially. Studying the effects of scenarios like the presence of multiple fractures, changes in porosity and permeability, fracture spacing, interaction with natural fractures, etc. would be needed to conclude the effectiveness of fracturing technology with the *in situ* mass transfer process.

Looking from the field scale point of view, using fracturing as a primary kick-off technology could prove very useful in increasing permeability of the low-permeability hydrate formations, like those found in the South China Sea or off-shore India. However, combining this with CH_4-CO_2 replacement would pose more logistical challenges rather than technical ones. Getting access to liquid CO_2 (or supercritical, or in emulsion form) at the wellhead for injection would require appropriate infrastructure and long-term planning. It would ultimately come down to the cost analysis to check if the value of the produced methane and sequestered CO_2 is large enough to warrant the capital expenditure.

REFERENCES

Abascal, J. L. F. et al. 2005. A potential model for the study of ices and amorphous water: TIP4P/Ice. *Journal of Chemical Physics* **122**(234511). https://doi.org/10.1063/1.1931662

Alavi, S. & Ripmeester, J. A. 2010. Nonequilibrium adiabatic molecular dynamics simulations of methane clathrate hydrate decomposition. *Journal of Chemical Physics* **132**(14): 144703. http://dx.doi.org/10.1063/1.3382341.

Alexiadis, A. & Kassinos, S. 2008. Molecular simulation of water in carbon nanotubes. *Chemical Reviews* **108**(12): 5014-5034. http://dx.doi.org/10.1021/cr078140f

Allen, M. P. 2004. Introduction to Molecular Dynamics Simulation. In *Computational Soft Matter: From synthetic polymers to proteins*, NIC Series **23**: 1-28, John von Neumann Institute for Computing, Julich.

Bagherzadeh, S. A. et al. 2012. Molecular Modeling of the Dissociation of Methane Hydrate in Contact with a Silica Surface. *Journal of Physical Chemistry B* **116**: 3188-3197. http://dx.doi.org/10.1021/jp2086544

Bagherzadeh, S. A. et al. 2015. Formation of methane nano-bubbles during hydrate decomposition and their effect on hydrate growth. *Journal of Chemical Physics* **142**(21). http://dx.doi.org/10.1063/1.4920971

Bai, D. et al. 2012. Replacement mechanism of methane hydrate with carbon dioxide from microsecond molecular dynamics simulations. *Energy & Environmental Science* **5**: 7033. http://dx.doi.org/10.1039/c2ee21189k

Bai, D. et al. 2015. How properties of solid surfaces modulate the nucleation of gas hydrate. *Scientific Reports* **5**:12747. http://dx.doi.org/10.1038/srep12747

Beaudoin, Y. C., Dallimore, S. R., & Boswell, R. 2014. Frozen Heat: A UNEP Global Outlook on Methane Gas Hydrates. Volume 2. United Nations Environment Programme, GRID-Arendal.

Berendsen, H. J. C. et al. 1984. Molecular dynamics with coupling to an external bath. *Journal of Chemical Physics* **81**(8): 3684-3690. https://doi.org/10.1063/1.448118.

Berendsen, H. J. C. et al. 1987. The missing term in effective pair potentials. *Journal of Physical Chemistry* **91**: 6269-6271.

Bernal, J. D. & Fowler, R. H. 1933. A Theory of Water and Ionic Solution, with Particular Reference to Hydrogen and Hydroxyl Ions. *Journal of Chemical Physics* **1**(8): 515. http://dx.doi.org/10.1063/1.1749327.

Birkedal, K. A., Hauge, L. P., et al. 2015. Transport Mechanisms for CO_2-CH_4 Exchange and Safe CO_2 Storage in Hydrate-Bearing Sandstone. *Energies* **8**: 4073-4095. http://dx.doi.org/10.3390/en8054073.

Boswell, R. & Collett, T. S. 2011. Current perspectives on gas hydrate resources. *Energy Environ. Sci.* **4**, 1206-1215. http://dx/doi/org/10.1039/C1030EE00203H.

Boswell, R. et al. 2012. Subsurface gas hydrates in the northern Gulf of Mexico. *Journal of Marine Petroleum Geology* **34**: 4-30.

Boswell, R., Schoderbek, D., Collett, T. S. et al. 2016. The Iġnik Sikumi Field Experiment, Alaska North Slope: Design, Operations, and Implications for CO_2–CH_4 Exchange in Gas Hydrate Reservoirs. *Energy Fuels* **31**: 140−153 http://dx.doi.org/10.1021/acs.energyfuels.6b01909.

Buehler, M. J. & Gao, H. 2006. Dynamical fracture instabilities due to local hyperelasticity at crack tips. *Nature* **439**(7074): 307–310. http://dx.doi.org/10.1038/nature04408.

Buehler, M. J. 2011. *Continuum and particle methods: Property calculation I.* Lecture Notes, Massachusetts Institute of Technology, Cambridge, MA.

Buffett, B. A. & Zatsepina, O. Y. 1999. Metastability of gas hydrate. *Geophysical Research Letters* **26**(19): 2981-2984.

Chialvo, A. A. et al. 2000. The structure of water from 25°C to 457°C: comparison between neutron scattering and molecular simulation. *Chemical Physics* **258**: 109-120.

Chialvo, A. A. et al. 2002. Molecular Dynamics Study of the Structure and thermophysical Properties of Model sI Clathrate Hydrates. *Journal of Physical Chemistry B* **106**: 442-451. http://dx.doi.org/10.1021/jp012735b.

Chen, C., Yang, L., Jia, R. et al. 2017. Simulation Study on the Effect of Fracturing Technology on the Production Efficiency of Natural Gas Hydrate. *Energies* **10**(2)**:** 1241. http://dx.doi.org/10.3390/en10081241.

Collett, T. S. et al. 2009. Natural Gas Hydrates: A Review, in Natural gas hydrates—Energy resource potential and associated geologic hazards, *AAPG Memoir* **89**, 146– 219.

Dallimore, S. R., Collett, T. S. 1995. Intrapermafrost gas hydrates from a deep core hole in the Mackenzie Delta, Northwest Territories, Canada. *Geology* **23**(6): 527-530

Dallimore, S. R., Collett, T. S., Taylor, A. E. et al. 2005. Scientific Results from the Mallik 2002 Gas Hydrate Production Research Well Program, Mackenzie Delta, Northwest Territories, Canada. Geological Survey of Canada, Bulletin No. 585, Natural Resources Canada, Ottawa, Canada.

Dallimore, S.R. et al. 2008. Geologic and Porous Media Factors Affecting the 2007 Production Response Characteristics of the JOGMEC/NRCan/Aurora Mallik Gas Hydrate Production Research Well. *Procs.,* 6th International Conference on Gas Hydrates, Vancouver, Canada.

Deserno, M. 2004. *How to calculate a three-dimensional g(r) under periodic boundary conditions*. Lecture Notes, Max-Plank Institute for Polymer Research, Mainz, Germany.

Deusner, C. et al. 2012. Methane production from Gas Hydrate deposits through injection of supercritical CO_2. *Energies* **5**: 2112-2140. http://dx.doi.org/10.3390/en5072112

Dougherty, R. C. 1998. Temperature and pressure dependence of hydrogen bond strength: A perturbation molecular orbital approach. *Journal of Chemical Physics* **109**(17): 7372. http://dx.doi.org/10.1063/1.477343

Edelsbrunner, H. & Mucke, E. P. 1994. Three-dimensional alpha shapes. *ACM Transactions on Graphics* **13**(1): 43-72. http://dx.doi.org/10.1145/174462.156635

English, N. J. & Macelroy, J. M. D. 2003. Structural and dynamical properties of methane clathrate hydrates. *Journal of Computational Chemistry* **24**: 1569-1581.

Espinoza, D. N. & Santamarina, J. C. 2011. P-wave monitoring of hydrate-bearing sand during CH_4-CO_2 replacement. *International Journal of Greenhouse Gas Control* **5**: 1031-1038. http://dx.doi.org/10.1016/j.ijggc.2011.02.006

Evans, D. J. & Holian, B. L. 1985. The Nose-Hoover thermostat. *Journal of Chemical Physics* **83**(8): 4069. https://doi.org/10.1063/1.449071

Fernandez, R. G. et al. 2006. The melting point of ice Ih for common water models calculated from direct coexistence of the solid-liquid interface. *Journal of Chemical Physics* **124**(144506). http://dx.doi.org/10.1063/1.2183308

Geng, C. Y. et al. 2009. Molecular simulation of the potential of methane reoccupation during the replacement of methane hydrate by CO_2. *Journal of Physical Chemistry A* **113**: 5463-5469. http://dx.doi.org/10.1021/jp811474m

Goryainov, S. V. 2012. A model of phase transitions in double-well Morse potential: Application to hydrogen bond. *Physica B* **407**: 4233-4237. http://dx.doi.org/10.1016/j.physb.2012.06.045

Haile, J.M. 1992. *Molecular Dynamics Simulation*, New York, NY: John Wiley & Sons, Inc.

Han, S. et al. 2010. Phase transitions in confined water nanofilms. Nature Physics 6: 685-689. http://dx.doi.org/10.1038/NPHYS1708

Hanasaki, I. & Nakatani, A. 2006. Fluidized piston model for molecular dynamics simulations of hydrodynamic flow. *Modelling and Simulation in Materials Science and Engineering* 14: S9–S20. http://dx.doi.org/10.1088/0965-0393/14/5/S02

Hancock, S. H., Collett, T. S., Dallimore, S. R. et al. 2005. Overview of thermal stimulation production-test results for the JAPEX/JNOC/GSC et al. Mallik 5L-38 gas hydrate production research well. Geological Survey of Canada, Bulletin No. 585, Natural Resources Canada, Ottawa, Canada.

Hancock, S. H., Dallimore, S. R., Collett, T. S. et al. 2005. Overview of pressure-drawdown production-test results for the JAPEX/JNOC/GSC et al. Mallik 5L-38 gas hydrate production research well. Geological Survey of Canada, Bulletin No. 585, Natural Resources Canada, Ottawa, Canada.

Harris, J. G. & Yung, K. H. 1995. Carbon dioxide's liquid vapor coexistence curve and critical properties as predicted by a simple molecular model. *Journal of Physical Chemistry* **99**: 12021-12024.

Heffelfinger, G. S. & van Swol, F. 1994. Diffusion in Lennard–Jones fluids using dual control volume grand canonical molecular dynamics simulation (DCV–GCMD). *Journal of Chemical Physics* **100**: 7548. https://doi.org/10.1063/1.466849

Helgerud, M. B. et al. 2009. Elastic wave speeds and moduli in polycrystalline ice Ih, sI methane hydrate, and sII methane-ethane hydrate. *Journal of Geophysical Research* **114**: B02212.

Hirohama, S. et al. 1996. Conversion of CH_4-hydrate to CO_2-hydrate in liquid CO_2. *Journal of Chemical Engineering of Japan* **29**(6): 1014-1020.

Hyodo, M. et al. 2013. Mechanical behavior of gas-saturated methane hydrate-bearing sediments. *Journal of Geophysical Research: Solid Earth* **118**: 5185-5194. http://dx.doi.org/10.1002/2013JB010233

Jendi, Z. M. et al. 2016. Ab initio modelling of methane hydrate thermophysical properties. *Physical Chemistry Chemical Physics* **18**: 10320. http://dx.doi.org/10.1039/c5cp06530e

Jia, J. et al. 2016. Microscopic Origin of Strain Hardening in Methane Hydrate. *Scientific Reports* **6**: 23548. http://dx.doi.org/10.1038/srep23548

Jiang, H. et al. 2007. Molecular Dynamics Simulations of Methane Hydrate Using Polarizable Force Fields. *Journal of Physical Chemistry B* **111**: 6486-6492. http://dx.doi.org/10.1021/jp068505k

Jin, G.R., et al. 2015. Optimization of gas production from hydrate deposit using joint depressurization and thermal stimulation. *J. Central South Univ. (Sci. Technol.)* **46**: 1534–1543.

Jones, J. E., 1924. On the determination of molecular fields - II. From the equation of state of a gas. *Proceedings of the Royal Society A* **106**:738. http://dx.doi.org/10.1098/rspa.1924.0082

Jorgansen, W. L. et al 1996. Development and testing of the OPLS All-Atom force field on conformational energetics and properties of organic liquids. *Journal of the American Chemical Society* **118**: 11225-11236

Jung, J. W. et al. 2010. Properties and phenomenon relevant to CH_4-CO_2 replacement in hydrate-bearing sediments. *Journal of Geophysical Research: Solid Earth* **115**(B10102). http://dx.doi.org/10.1029/2009JB000812

Jung, J. W., Santamarina, J. C. et al. 2011. Gas production from hydrate-bearing sediments: The role of fine particles. *Energy & Fuels* **26**: 480-487. http://dx.doi.org/10.1021/ef101651b

Kaminski, G. et al. 1994. Free energies of hydration and pure liquid properties of hydrocarbons from the OPLS All-Atom model. *Journal of Physical Chemistry* **98**: 13077-13082.

Keffer, D. 2001. *The Working Man's Guide to Obtaining Self Diffusion Coefficients from Molecular Dynamics Simulations*. Lecture Notes, University of Tennessee, Knoxville.

Koh, C. A. et al. 2000. Water ordering around methane during hydrate formation. *Journal of Chemical Physics* **113**(15): 6390. http://dx.doi.org/10.1063/1.1288818

Konno, Y., Masuda, Y., Hariguchi, Y. et al. 2010. Key factors for depressurization induced gas production from oceanic methane hydrates. *Energy Fuels* **24**, 1736–1744. http://pubs.acs.org/doi/pdf/10.1021/ef901115h

Konno, Y. et al. 2016. Hydraulic fracturing in methane-hydrate-bearing sand. *RSC Advances* **6**: 73148. http://dx.doi.org/10.1039/c6ra15520k

Konno, Y., Fujii, T., Sato, A. et al. 2017. Key Findings of the World's First Offshore Methane Hydrate Production Test off the Coast of Japan: Toward Future Commercial Production. *Energy Fuels* **31**, 2607−2616. DOI: http://dx.doi.org/10.1021/acs.energyfuels.6b03143

Krynicki, K. et al. 1978. Pressure and temperature dependence of self-diffusion in water. *Faraday Discussions of the Chemical Society* **66:** 199-208. http://dx.doi.org/10.1039/DC9786600199

Kuhs, W. F. et al. 2006. Formation of methane hydrate from polydisperse ice powders. *Journal of Physical Chemistry B* **110**(26): 13283-13295. http://dx.doi.org/10.1021/jp061060f

Kurihara, M., Funatsu, K., Kusaka, K. et al. 2005. Well-test analysis for gas hydrate reservoirs: examination of parameters suggested by conventional analysis for the JAPEX/JNOC/GSC et al. Mallik 5L-38 gas hydrate production research well. Geological Survey of Canada, Bulletin No. 585, Natural Resources Canada, Ottawa, Canada.

Kvamme, B. and Kuznetsova, T. 2010. Investigation into stability and interfacial properties of CO_2 hydrate-aqueous fluid system. *Mathematical and Computer Modelling* **51**: 156-159. http://dx.doi.org/10.1016/j.mcm.2009.08.007

Kvamme, B. et al. 2014. Consequences of CO_2 solubility for hydrate formation from carbon dioxide containing water and other impurities. *Physical Chemistry Chemical Physics* **16**: 8623-8638. http://dx.doi.org/10.1039/c3cp53858c

Kvamme, B. 2016. Thermodynamic limitations of the CO_2/N_2 mixture injected into CH4 hydrate in the Ignik Sikumi field trial. *Journal of Chemical Engineering & Data* **61**: 1280-1295. http://dx.doi.org/10.1021/acs.jced.5b00930

Kvenvolden, K.A. 1993. Gas hydrates, geological perspective and global change. *Reviews of Geophysics*. **31**, 173–187. http://onlinelibrary.wiley.com/doi/10.1029/93RG00268/epdf

Kvenvolden, K. A. 1999. Potential effects of gas hydrate on human welfare. *PNAS* **96**: 73420-3426. http://dx.doi.org/10.1073/PNAS.96.7.3420

Li, Y. et al. 2015. Mechanical behaviors of permafrost-associated methane hydrate-bearing sediments under different mining methods. *Applied Energy* **162**: 1627-1632. http://dx.doi.org/10.1016/j.apenergy.2015.04.065

Lui, W. et al. 2016. Experimental study on the mechanical properties of sediments containing CH_4 and CO_2 hydrate mixtures. *Journal of Natural Gas Science and Engineering* **32**: 20-27. http://dx.doi.org/10.1016/j.jngse.2016.03.012

Lui, Y. et al. 2017. Evolution of bubbles in decomposition and replacement process of methane hydrate. *Molecular Simulation* **43**(13-16): 1061-1073. http://dx.doi.org/10.1080/08927022.2017.1359745

McGrail, B. P. et al. 2007. Using Carbon Dioxide to Enhance Recovery of Methane from Gas Hydrate Reservoirs: Final Summary Report, PNNL-17035, Pacific Northwest National Laboratory, Oak Ridge, TN.

McMullan, R. K. & Jeffrey, G. 1965. Polyhedral clathrate hydrates. IX. Structure of ethylene oxide hydrate. *Journal of Chemical Physics* **42:** 2725.

Moridis, G.J., Silpngarmlert, S., Reagan, M.T. et al. 2011. Gas production from a cold, stratigraphically-bounded gas hydrate deposit at the Mount Elbert gas hydrate stratigraphic test well, Alaska North Slope: Implications of uncertainties. *Marine and Petroleum Geology* **28:** 517–534. https://doi.org/10.1016/j.marpetgeo.2010.01.005

Moridis, G. J., Reagan, M. T., Boyle, K. L. et al. 2011. Evaluation of the Gas Production Potential of Some Particularly Challenging Types of Oceanic Hydrate deposits. *Transport in Porous Media* **90**:269–299. http://dx.doi.org/10.1007/s11242-011-9762-5

Ning, F. L. et al. 2012. Mechanical properties of clathrate hydrates: status and perspectives. *Energy & Environmental Science* **5:** 6779–6795. http://dx.doi.org/10.1039/C2EE03435B

Ning, F. L. et al. 2015. Compressibility, thermal expansion coefficient and heat capacity of CH_4 and CO_2 hydrate mixtures using molecular dynamics simulations. *Physical Chemistry Chemical Physics* **17**: 2869–2883. http://dx.doi.org/10.1039/c4cp04212c

Ohkagi, K. et al. 1996. Methane exploitation by carbon dioxide from gas hydrates – Phase equilibria for CO_2-CH_4 mixed hydrate system. *Journal of Chemical Engineering of Japan* **29**(3): 478-483.

Okano, Y. & Yasuoka, K. 2006. Free-energy calculation of structure-H hydrates. *Journal of Chemical Physics* **124**(2): 024510. http://dx.doi.org/10.1063/1.2150430

Ota, M. et al. 2005. Methane recovery from methane hydrate using pressurized CO_2. *Fluid Phase Equilibria* **228-229**: 553-559. http://dx.doi.org/10.1016/j.fluid.2004.10.002

Oyama, A. & Masutani, S. M. 2017. A Review of the Methane Hydrate Program in Japan. *Energies* **10**: 1447. http://dx.doi.org/10.3390/en10101447

Parrinello, M. & Rahman, A. 1981. Polymorphic transitions in single crystals: A new molecular dynamics method. *Journal of Applied Physics* 52: 7182. https://doi.org/10.1063/1.328693

Peters, B. et al. 2008. Path Sampling Calculation of Methane Diffusivity in Natural Gas Hydrates from a Water-Vacancy Assisted Mechanism. *Journal of American Chemical Society* **130**(51): 17342-17350. http://dx.doi.org/10.1021/ja802014m

Picaud, S. 2006. Dynamics of TIP5P and TIP4P/Ice potentials. *Journal of Chemical Physics* **125**(17). http://dx.doi.org/10.1063/1.2370882

Plimpton, S. 1995. Fast Parallel Algorithms for Short-Range Molecular Dynamics. *Journal of Computational Physics* **117:** 1-19.

Polak, E. 1971. *Computational methods in optimization: A unified approach*, Volume 77, New York, NY: Academic Press, Inc.

Potoff, J. J. & Siepmann, J. I. 2001. Vapor-Liquid equilibria of mixtures containing alkanes, carbon dioxide, and nitrogen. *AIChE Journal* **47**(7): 1676-1682.

Qorbani, K. & Kvamme, B. 2016. Non-equilibrium simulation of CH_4 production from gas hydrate reservoirs through the depressurization method. *Journal of Natural Gas Science and Engineering* **35:** 1544–1554.

Qorbani, K., Kvamme, B., Kuznetsova, T. 2017. Using a reactive transport simulator to simulate CH_4 production from bear island basin in the Barents Sea utilizing the depressurization method. *Energies* **10**(2): 187. http://dx/doi/org/10.3390/en10020187

Ripmeester, J. A. et al. 1994. Molecular perspectives on structure and dynamics in clathrate hydrates. *Annals of New York Academy of Sciences*, 161-176.

Ruan, X. et al. 2017. Numerical investigation of the production behavior of methane hydrate under depressurization conditions combined with well-wall heating. *Energies* **10**(2): 161.

Schoderbek, D., Farrell, H., Hester, K. et al. 2013. ConocoPhillips Gas Hydrate Production Test: Final Technical Report for Period October 1, 2008-June 30, 2013, DOE Award No.: DENT0006553.

Shrake, A. & Rupley, J. A. 1973. Environment and exposure to solvent of protein atoms, Lysozyme and insulin panel. *Journal of Molecular Biology* **79**(2): 351-364.

Shvab, I. & Sadus, R. J. 2014. Thermodynamic properties and diffusion of water + methane binary mixtures. *Journal of Chemical Physics* **140**(10): 104505. http://dx.doi.org/10.1063/1.4867282

Sloan, E.D. and Koh, C.A. 2008. *Clatharate Hydrates of Natural Gases*; third edition. Boca Raton, FL: CRC Press

Song, Y., Zhang, L., Lv, Q. et al. 2016. Assessment of gas production from natural gas hydrate using depressurization, thermal stimulation and combined method. *RSC Advances* **6:** 47357–47367.

Sparks, K. A. et al. 1999. Configurational Properties of Water Clathrates: Monte Carlo and Multidimensional Integration versus the Lennard-Jones and Devonshire Approximation. *Journal of Physical Chemistry B* **103**: 6300-6308. http://dx.doi.org/10.1021/jp9903108

Stern, L. A., Kirby, S. H., Durham, W. B. 1998. Polycrystalline methane hydrate: synthesis from superheated ice, and low-temperature mechanical properties. *Energy & Fuels* **12:** 201–211.

Stevens, J. C. et al. 2008. Experimental hydrate formation and gas production scenarios based on CO_2 sequestration. *Procs.*, 6th International Conference on Gas Hydrates, Vancouver, British Columbia, Canada, July 6-10.

Stukowski, A. 2010. Visualization and analysis of atomistic simulation data with OVITO - the Open Visualization Tool. *Modelling & Simulation in Materials Science and Engineering* **18**(1): 015012. http://dx.doi.org/10.1088/0965-0393/18/1/015012

Stukowski, A. 2014. Computational analysis methods in atomistic modeling of crystals. *Journal of the Minerals, metals, and materials society* **66**(3): 399-407. http://dx.doi.org/10.1007/s11837-013-0827-5

Sujith, K. S. & Ramachandran, C. N. 2016. Carbon dioxide induced bubble formation in a CH_4–CO_2–H_2O ternary system: a molecular dynamics simulation study. *Physical Chemistry Chemical Physics* **18**: 3746. http://dx.doi.org/10.1039/c5cp05623c

Sveinsson, H. A. 2015. *Molecular modeling of fracture in methane hydrates*. MS thesis, University of Oslo, Oslo. http://dx.doi.org/10.13140/RG.2.1.1037.7126

Takaba, H. et al. 2007. Molecular simulation of pressure-driven fluid flow in nanoporous membranes. *Journal of Chemical Physics* **127**(5). http://dx.doi.org/10.1063/1.2749236

Takeuchi, F. et al. 2013. Water proton configurations in structures I, II, and H clathrate hydrate unit cells. *Journal of Chemical Physics* **138**(12): 124504. http://dx.doi.org/10.1063/1.4795499

Thompson, H. et al. 2006. Methane hydrate formation and decomposition: Structural studies via neutron diffraction and empirical potential structure refinement. *Journal of Chemical Physics* **124**(16): 164508. http://dx.doi.org/10.1063/1.2191056

Tolman, R. C., 1918. A General Theory of Energy Partition with Applications to Quantum Theory. *American Physical Society* **11**(261). https://doi.org/10.1103/PhysRev.11.261

Tse, J. S. et al. 1983. Dynamical properties of the structure I clathrate hydrate of xenon. *Journal of Chemical Physics* **78**(2096). https://doi.org/10.1063/1.444921

Tse, J. S. et al. 1984. Computer simulation studies of the structure I clathrate hydrates of methane, tetrafluoromethane, cyclopropane, and ethylene oxide. *Journal of Chemical Physics* **81**(6146). https://doi.org/10.1063/1.447569

Uchida, T. et al. 2000. Replacing methane with CO_2 in clathrate hydrate: Observations using Raman Spectroscopy. *Procs.*, 5th International Conference on Greenhouse Gas Control Technologies, Cairns, Australia, September 13-16.

Uddin, M. & Coombe, D. 2014. Kinetics of CH_4 and CO_2 hydrate dissociation and gas bubble evolution via MD simulation. *Journal of Physical Chemistry A* **118**:1971-1988. http://dx.doi.org/10.1021/jp410789j

Ungerer, P. et al. 2006. Applications of molecular simulation in Oil and Gas production and processing. *Oil & Gas Science and Technology* **61**(3): 387-403.

Waite, W. F. et al. 2000. Laboratory measurements of compressional and shear wave speeds through methane hydrate. *Annals of New York Academy of Sciences*, 1003-1010.

White, A. N. 2003. *Mass transfer study of CO_2 penetration through methane hydrates using CO_2 vapor and a CO_2 nucleated micro-emulsion*. MS thesis, University of Alaska Fairbanks, Fairbanks, AK (December 2003).

Wu, J. et al. 2015. Mechanical instability of monocrystalline and polycrystalline methane hydrates. *Nature Communications* **6**(8743). http://dx.doi.org/10.1038/ncomms9743

Yagasaki, T. et al. 2014. Effect of bubble formation on the dissociation of methane hydrate in water: A molecular dynamics study. *Journal of Physical Chemistry B* **118**: 1900-1906. http://dx.doi.org/10.1021/jp412692d

Yamamoto, K., Dallimore, S. 2008. Mallik 2006–2008 gas hydrate research project progress. *Fire Ice, Methane Hydrate Newsletters* **8** (3): 1–5.

Yun, T. S., Santamarina, J. C., Ruppel, C. 2007. Mechanical properties of sand, silt, and clay containing tetrahydrofuran hydrate. *Journal of Geophysical Research* **112**. http://dx.doi.org/10.1029/2006JB004484

Zhang, Z. & Duan, Z. 2005. An optimized molecular potential for carbon dioxide. *Journal of Chemical Physics* **122**(214507). http://dx.doi.org/10.1063/1.1924700

Zhao, J. et al. 2012. A review on research on replacement of CH_4 in natural gas hydrates by use of CO_2. *Energies* 5: 399-419. http://dx.doi.org/10.3390/en5020399

APPENDICES

Appendix A: Snapshots of all simulation cases

This section includes snapshots of all cases at the start and the end of simulations. All simulations were run for a total of 1 ns.

- Oxygen of H_2O – Green spheres
- Carbon of CH_4 – Blue spheres
- Carbon of CO_2 – Red spheres

The cases covered in this thesis are:

Table A1: Summary of all simulation cases run

Case No.	No. of CO_2 injected	Temp (K)	Pressure (atm)	Surface Area	$\frac{\text{Number of } CO_2}{\text{Surface Area}}$ x10^{-2}
1	300	270	20	9187.7 Å	3.26
2	300	260	20	9187.7 Å	3.26
3	300	280	20	9187.7 Å	3.26
4	450	270	20	9187.7 Å	4.89
5	600	270	20	9187.7 Å	6.53
6	370	270	20	11336.2 Å	3.26
7	450	270	20	13787.5 Å	3.26
8	600	270	20	18369.7 Å	3.26

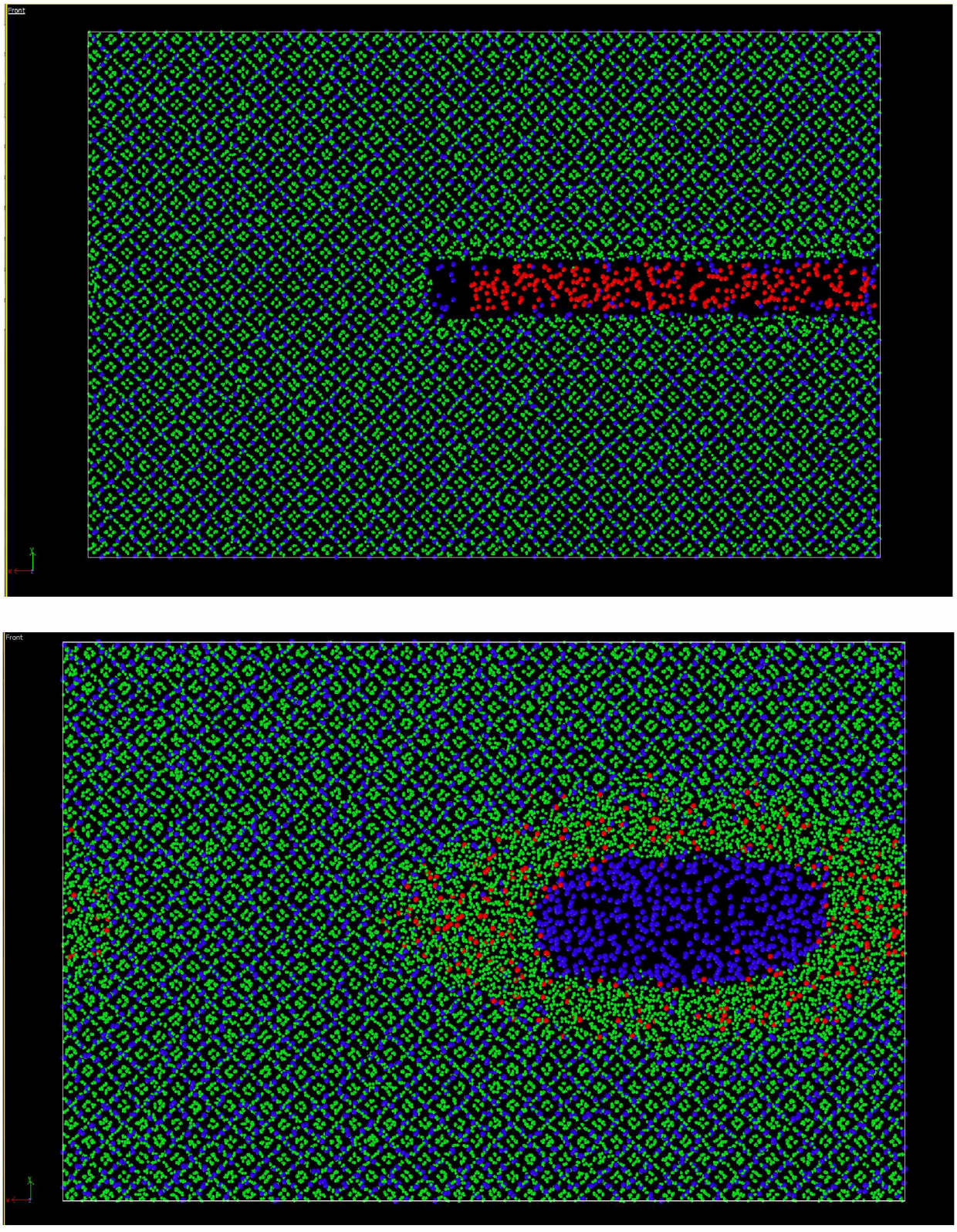

Figure A1: Snapshot of Case No. 1 (A) at 0 ps, (B) at 1 ns.

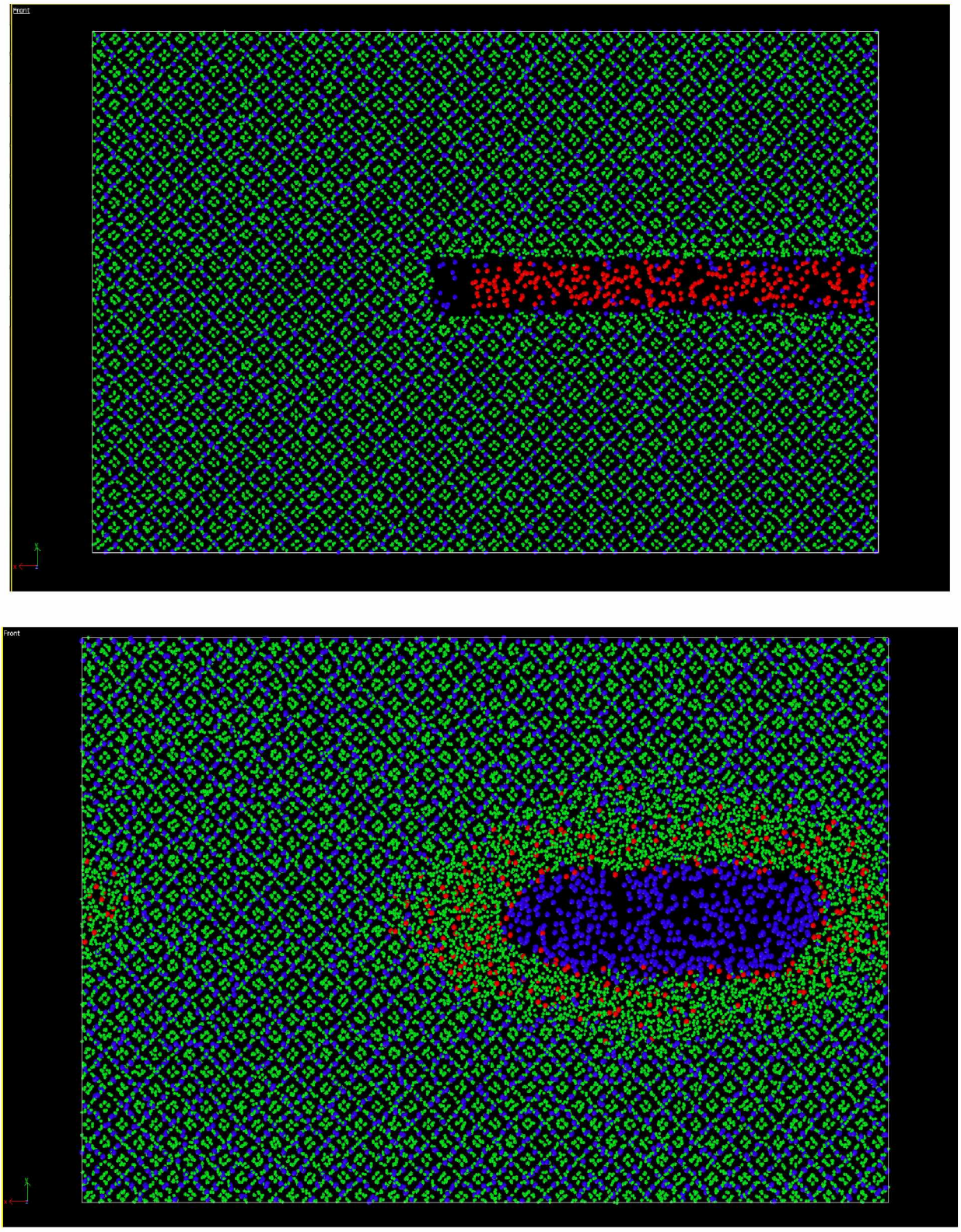

Figure A2: Snapshot of Case No. 2 (A) at 0 ps, (B) at 1 ns.

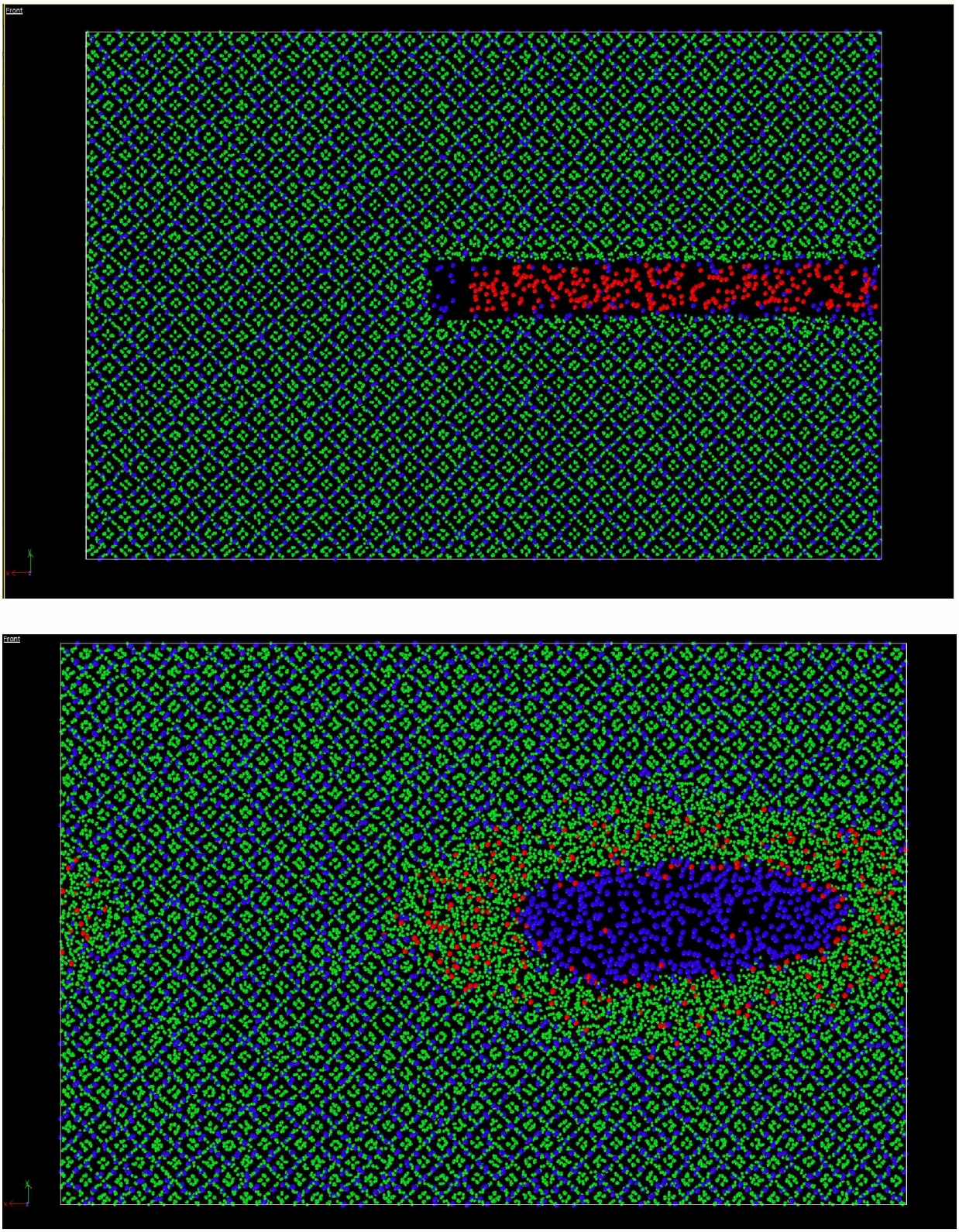

Figure A3: Snapshot of Case No. 3 (A) at 0 ps, (B) at 1 ns.

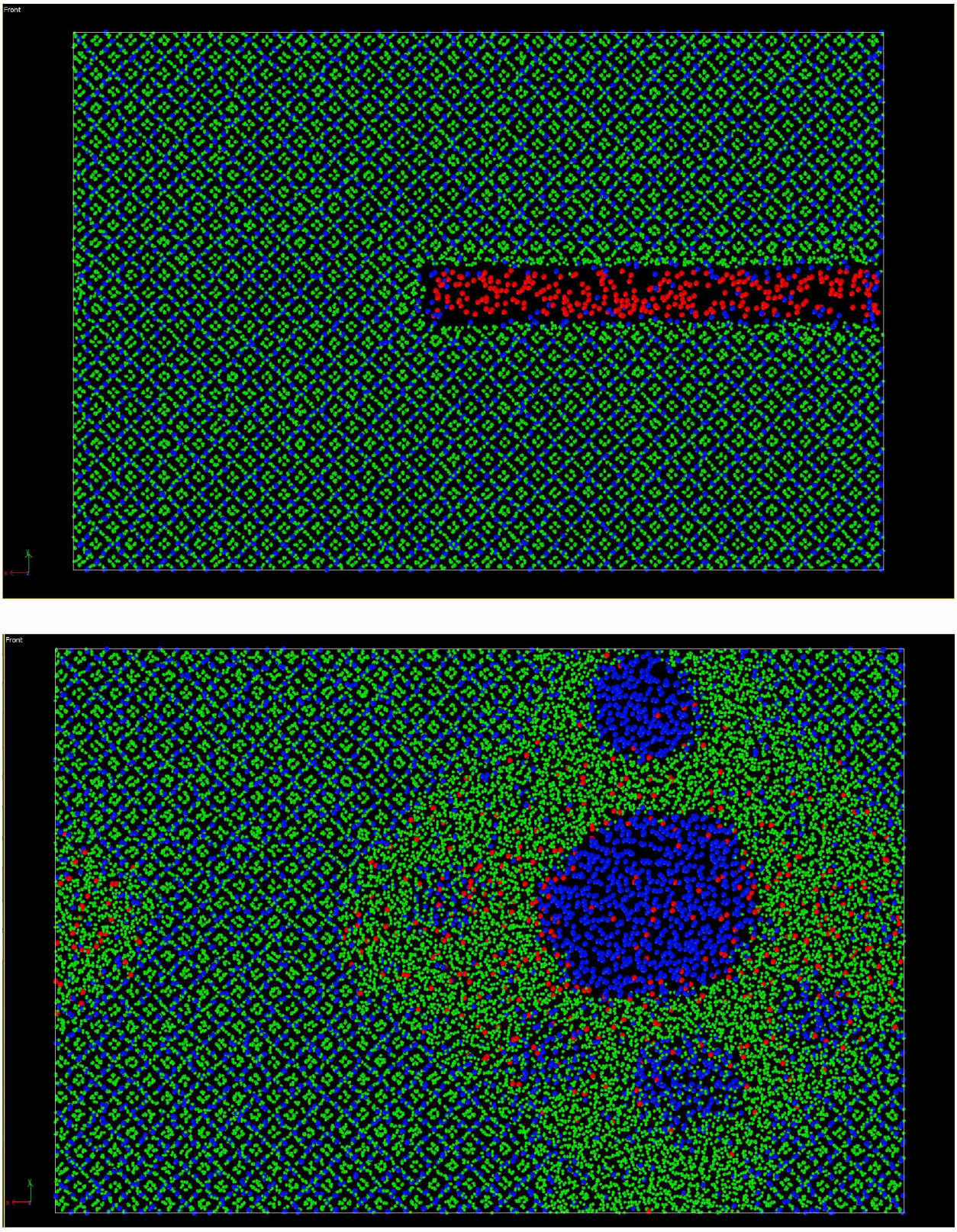

Figure A4: Snapshot of Case No. 4 (A) at 0 ps, (B) at 1 ns.

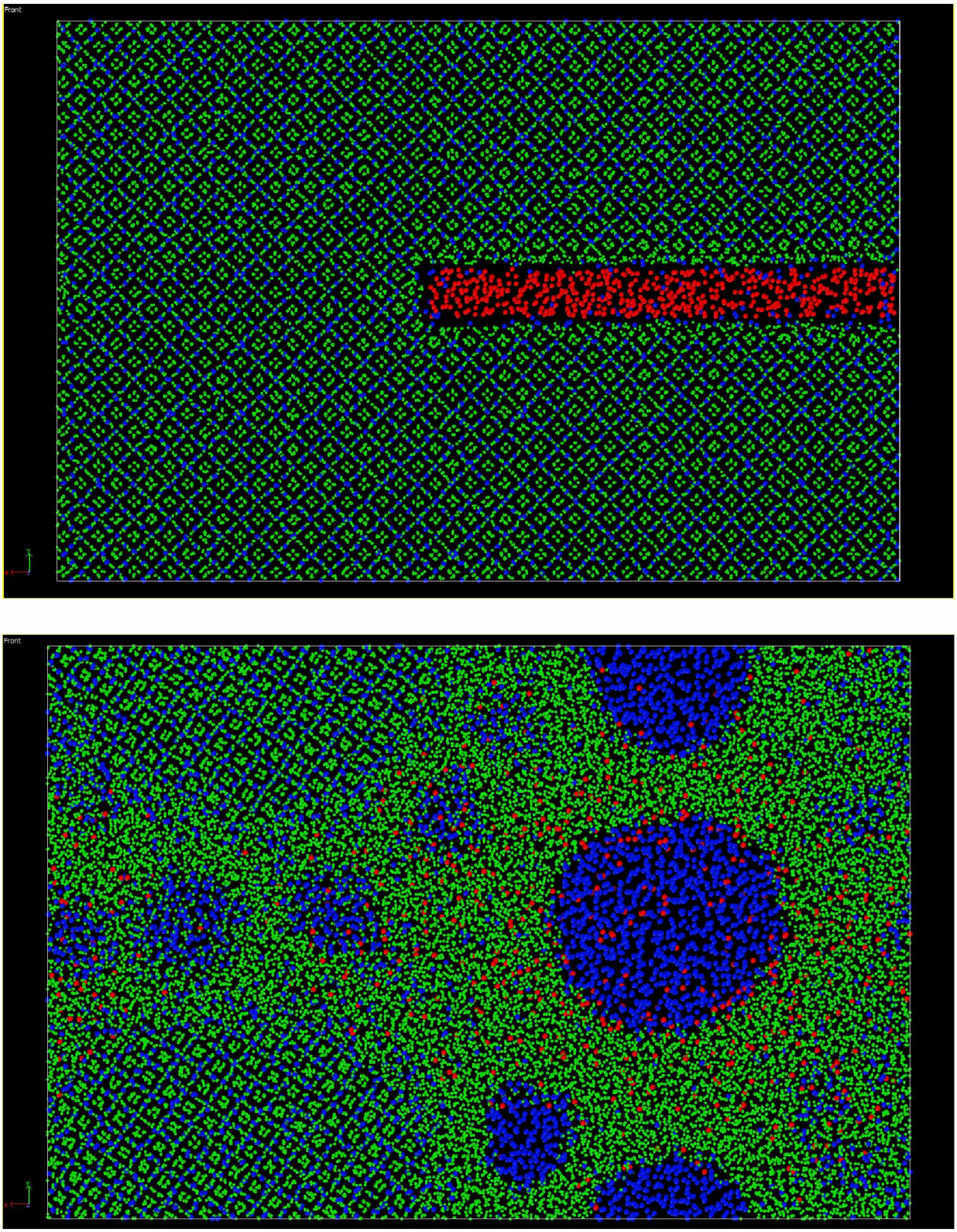

Figure A5: Snapshot of Case No. 5 (A) at 0 ps, (B) at 1 ns.

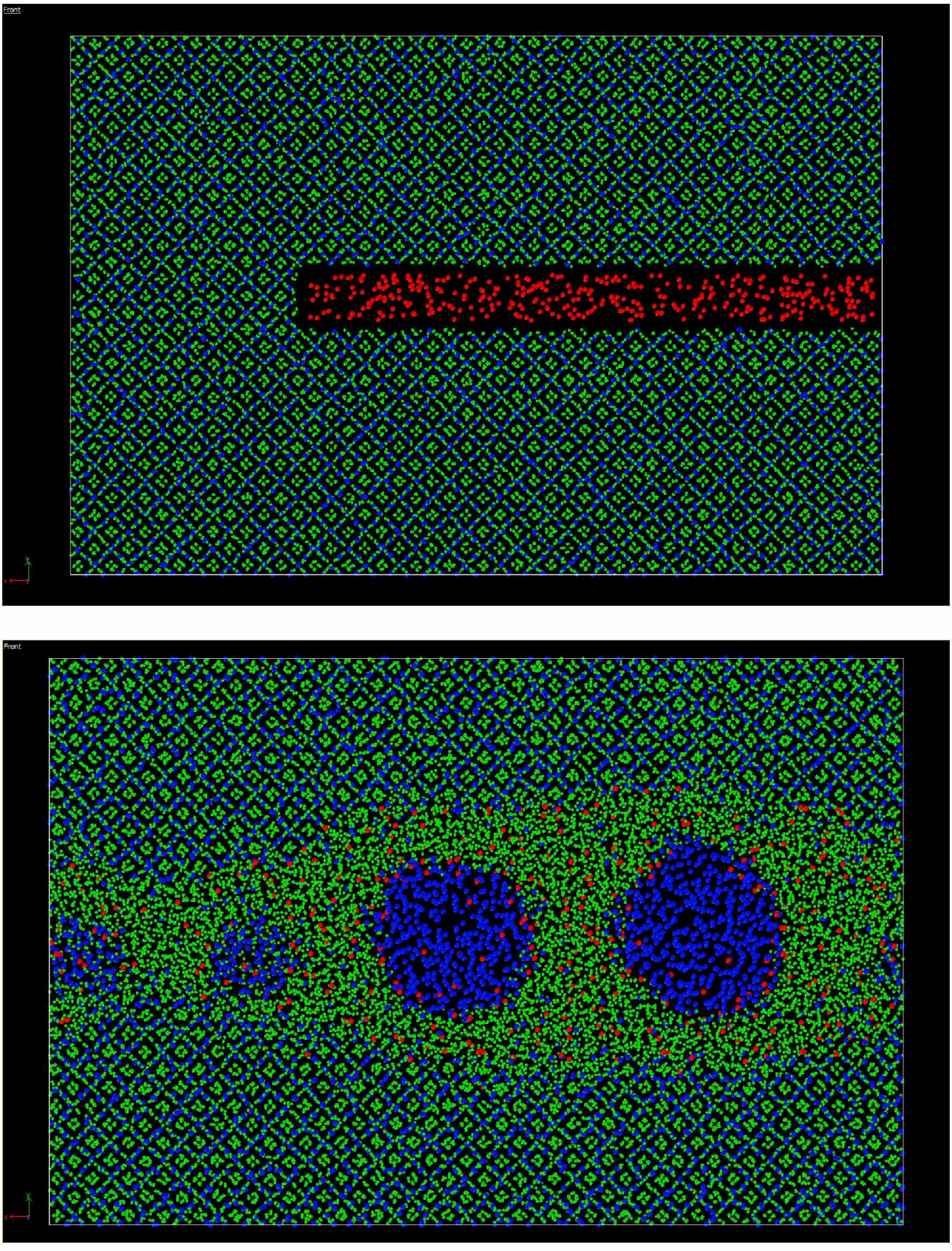

Figure A6: Snapshot of Case No. 6 (A) at 0 ps, (B) at 1 ns.

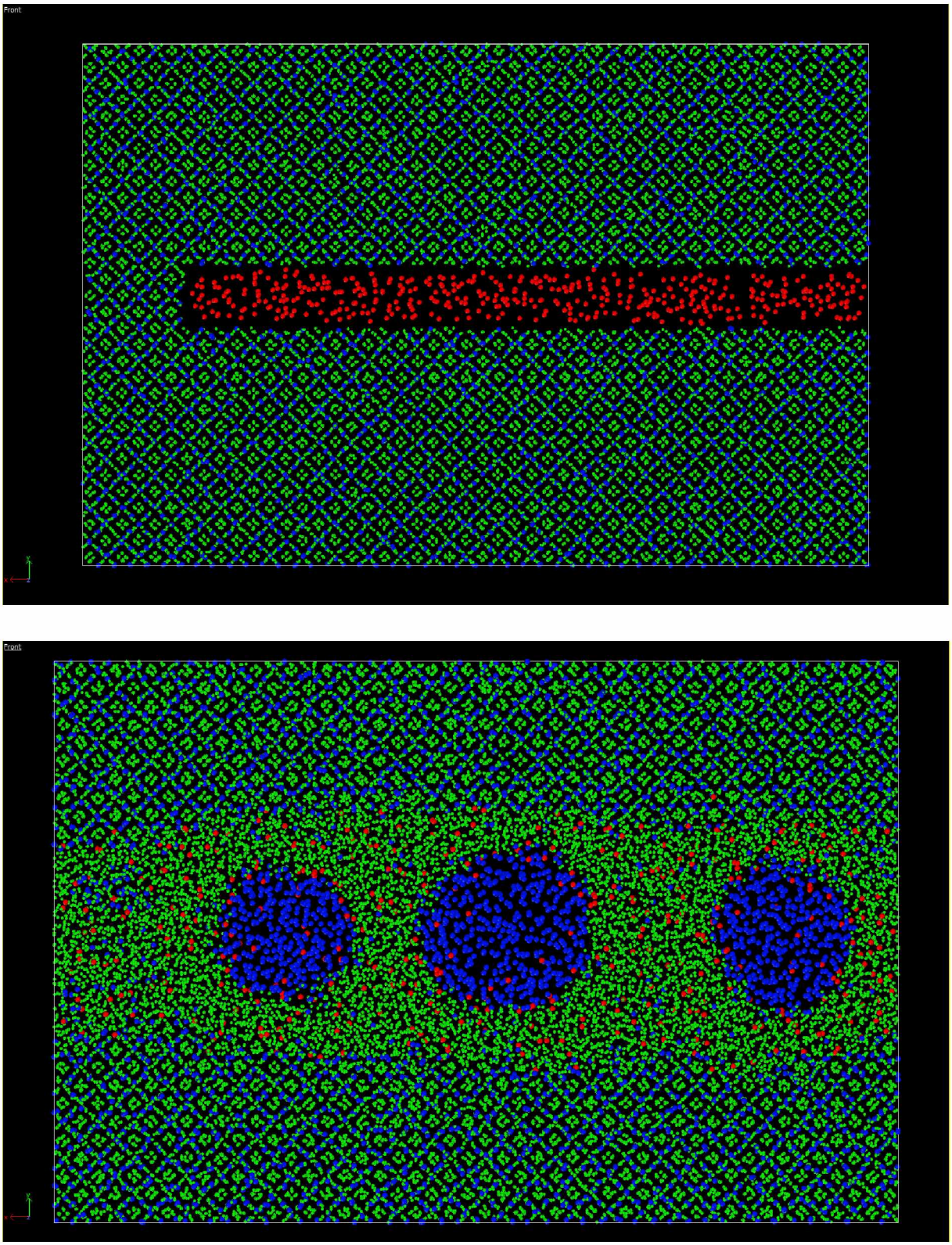

Figure A7: Snapshot of Case No. 7 (A) at 0 ps, (B) at 1 ns.

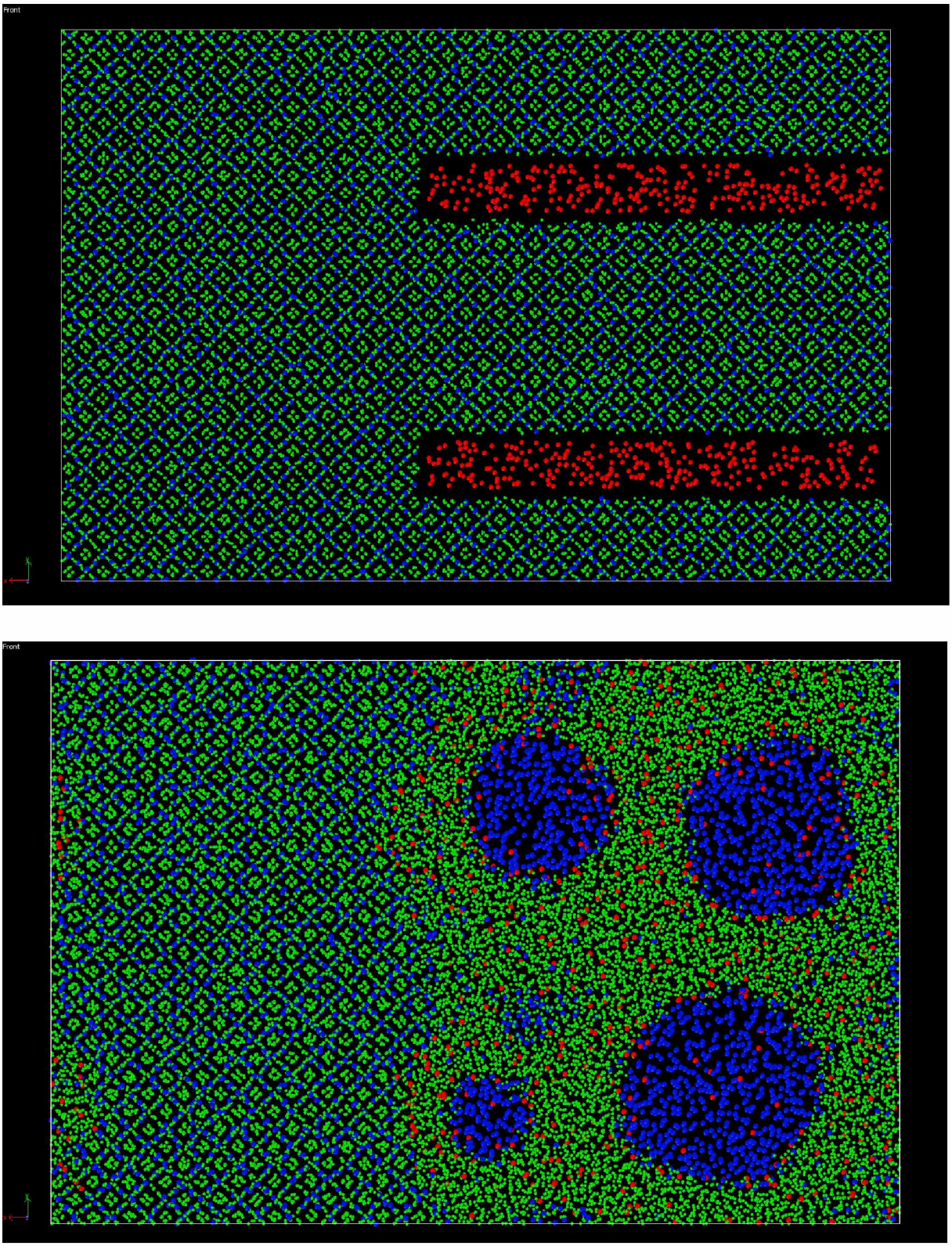

Figure A8: Snapshot of Case No. 8 (A) at 0 ps, (B) at 1 ns.

Appendix B: Cluster Analysis

The results of cluster analysis with different cutoff compared in Figure 6.14 are shown in table S1. The clusters of C atoms in CH_4 are listed in decreasing order of cluster size within each cutoff at a different time. Through this process the rough amount of CH_4 molecules in each nanobubble is obtained. To keep the table short, only cluster sizes greater than 15 are shown here. Although smaller cutoffs have fewer numbers of clusters above size 15, they have a large number of smaller clusters between the size of 15 and 10 not reported here. The accumulation of these smaller clusters into bigger ones can be seen from the larger size clusters at longer times and from more clusters above 15 at higher cutoffs. The results presented here are for simulation of 300 CO_2 molecules injection at 270 K and 20 atmospheres for 2 ns of simulation time.

Table A2: Details of Cluster Analysis with different cutoff radii

	4.5 Å	**5.0 Å**	**5.5 Å**	**6.0 Å**	**6.5 Å**
0.2 ns	309, 169, 24, 17	562, 26, 17	570, 30, 18	573, 35, 22	586
0.4 ns	535, 16	573, 20	581, 20, 16	582, 37, 20, 18, 17	596
0.6 ns	500, 20	575, 20	591, 20	601, 24, 21, 16	623
0.8 ns	516, 21, 19	578, 19	584, 19, 17	588, 21, 21, 17, 16	623
1 ns	543	600, 16	602	603, 39, 26, 17, 17, 16	623
1.2 ns	560	604	610	610, 151, 20, 19	623
1.4 ns	577	610	615	617, 41, 20	623
1.6 ns	586	618	625	621, 46, 42, 22, 21, 19	623
1.8 ns	588	622	630	634, 41, 20, 17, 17	635
2 ns	580	621	634	636, 57, 16	637